University of Nottingham

UK | CHINA | MALAYSIA

Development of microfluidic based graphene/micro-capsulated phase change materials for thermal management application

By

Yanhong Guo

Thesis submitted to the University of Nottingham for the degree of Doctor of Philosophy

July 2024

Abstract

Phase change materials (PCMs) are commonly used for heat storage, but they face challenges such as leakage, corrosion, and low thermal conductivity. In this project, microencapsulation packaging is employed to address these issues before using PCMs for energy storage and thermal management. Additionally, graphene-based materials are incorporated to enhance the heat transfer of the microencapsulated phase change materials (MEPCMs).The formation, breakup, and phase change mechanism of low melting point alloy (LMPA) PCM particles in a microfluidic channel are numerically studied. The effects of flow rate, interfacial tension, perturbation flow Weber number, and oscillating frequencies on droplet dynamics are being investigated. Furthermore, experimental synthesis is carried out in a needle-based microfluidic device to synthesize MEPCMs and graphene-decorated MEPCMs. The results demonstrate a smooth surface and spherical shape of the microcapsules with a relative size change in the MEPCM particles within 5%. These microcapsules exhibit good phase transition and thermal storage performance, with the shell material providing effective protection for the PCM material. The addition of graphene significantly improves heat conductivity as the mass ratio increases from 0.1 to 2 wt%. Finally, the thermal performance and pressure drop of various microchannel designs and coolants are compared. Structure C proves to have the best PEC performance, reaching 1.43 at Re=600. Geometric shapes of micro pin fins minimally affect thermal resistance, but triangular fins cause the highest pressure drop. Circular pins exhibit the highest PEC, surpassing hexagonal pins by over 8% in certain Re ranges. Micro pin fin spacing influences outlet temperature distribution and PEC optimization, with 0.3 mm spacing achieving a peak PEC of 1.57 at Re=600. GO/MEPCM slurry in microchannels shows higher pressure drop and thermal resistance compared to water. The

PEC peaks at 3.79 with 0.4wt% GO content at Re=100, outperforming Al2O3 nanofluid by 84% at Re=400.

Acknowledgment

Firstly, I would like to express my gratitude to my supervisor, Dr. Yong Ren, for his support and assistance in my research and daily life. He not only provided me with ample freedom, but also provided me with timely assistance when I encountered difficulties, which made me feel warm. His affirmation and encouragement of my work in every meeting discussion have made me more confident and interested in scientific research, and also strengthened my determination to pursue this path of scientific research. In addition, his sincere and easy-going attitude towards others, as well as his disciplined and efficient lifestyle habits, have deeply influenced me and are a role model for me to learn from. Secondly, I would like to thank my other supervisors, Dr. Siegfried Yeboah, Prof. Yuying Yan and my internal reviewer, Prof. Xiaogang Yang for their advice and guidance, which have benefited me greatly. Their unique personality charm and rigorous academic attitude have also subtly influenced me, making me understand how to improve myself more comprehensively. At the same time, I am very grateful to Prof. Houcheng Zhang for his help in my studies. I still remember that it was because of his tremendous help that I had the opportunity to apply for a doctoral program at the University of Nottingham Ningbo. His rigorous attitude towards scientific research has also profoundly influenced my research attitude during my doctoral studies. Thirdly, I want to give thanks to my friends, Zhiyu Zhang, Rui Jiang, Minrui Ni, Fei Long, Tuo Hou, Jiaying Lu and Yuqing Shen. Their care and support for my studies and life have made me feel warm during my doctoral studies, allowing me to experience many wonderful and

unforgettable happy days. Because communicating with them on various daily topics has enriched and deepened my life, I am very grateful for the time we have spent together.

Finally, I would like to express my special gratitude to my family. First of all, I would like to express my gratitude to my parents for their unconditional support of my siblings and me in our studies over the years. Even in the most difficult times, they have never complained about their hard work, especially my mother. Her gentle, kind, tolerant, and strong personality has deeply influenced me. Let me always remember to be kind to others and always be grateful. She is the greatest mother in my heart. Secondly, I would like to express my gratitude to my two younger sisters and younger brother, who have always been my pride. Their unconditional love for me has always made me feel that I am a very happy person. Because of my family, I am not afraid of any difficulties in life, because no matter what difficulties I encounter, the thought of having them fills my heart with strength, giving me the courage to try and change. I am very grateful for their contributions to me, because their support, tolerance, encouragement, and care have made me who I am now.

Contents

List of Publications

[1] **Y. Guo**, T. Hou, J. Wang, Y. Yan, W. Li, Y. Ren, S. Yan. Phase Change Materials Meet Microfluidic Encapsulation, Advanced Science, 2023: 2304580.

[2] **Y. Guo**, Y. Liu, T. Hou, X. Zhang, J. Gao, J. He, C. Wang, J. Wang, Q. Zhao, Y. Chan, Y. Ren. Oscillatory flow driven microdroplet breakup dynamics and microparticle formation in LMPA-water two phase flow system, Engineering Applications of Computational Fluid Mechanics, 2024, 18: 2315972.

[3] **Y. Guo**, Y. Ren, T. Hou, J. Wang, C. Wang. Numerical Study on the Formation and Solidification of LMPA Microdroplet in a Microfluidic Device, Frontiers in Energy Research, 2022, 10: 843118.

[4] **Y. Guo**, X. Zhang, J. Wang, Y. Yan, Y. Ren. Investigation of continuous pulse current source on the performance of phase change material-thermoelectric cooler system. e-Prime - Advances in Electrical Engineering, Electronics and Energy, 2023, 4: 100163.

[5] H. Wang, **Y. Guo**, Y. Ren, S. Yeboah, J. Wang, F. Long, Z. Zhang, R. Jiang. Investigation of the thermal management potential of phase change material for lithium-ion battery, Applied Thermal Engineering, 2024, 236: 121590. (Co-first authors)

[6] X. Xu, J. Lin, **Y. Guo**, X. Wu, Y. Xu, D. Zhang, X. Zhang, X. Yujiao, J. Wang, C. Yao, J. Yao, J. Xing, Y. Cao, Y. Li, W. Ren, T. Chen, Y. Ren, A. Wu, TiO2-based Surface-Enhanced Raman Scattering bio-probe for efficient circulating tumor cell detection on microfilter, Biosensors & Bioelectronics, 210 (2022) 114305.

[7] F. Long, **Y. Guo**, Z. Zhang, J. Wang, Y. Ren, Y. Cheng, G. Xu, Recent Progress of Droplet Microfluidic Emulsification Based Synthesis of Functional Microparticles, Global Challenges, 7(9) (2023) 2300063.

[8] Z. Zhang, F. Long, **Y. Guo**, Y. Liang, J. Wang, Y. Ren, Enhanced visible-light-driven photocatalytic application for water purification and hydrogen evolution by large-sized nanofilm-constructed hierarchical porous g-C3N4/SiO2, Nano Select, (2024) e202300098.

Conference paper

[1] **Y. Guo**, F. Long, Z. Zhang,Y. Ren, NEEDLE-BASED MICROFLUIDIC PRODUCTION OF MICROENCAPSULATED PHASE CHANGE MATERIAL FOR THERMAL ENERGY STORAGE, Proceeding of International Heat Transfer Conference 17, (2023).

Patents

[1] 任勇(Yong Ren), 阎玉英(Yuying Yan), **郭艳红(Yanhong Guo)**, 王静(Jing Wang). 一种热电发电机器件及该器件的性能检测方法(A thermoelectric generator device and its performance testing method). 申请号(Application number)：CN202211587280.1（发明专利）(Invention patent)

[2] 任勇(Yong Ren), 阎玉英(Yuying Yan), **郭艳红(Yanhong Guo)**,龙菲(Fei Long), 王静(Jing Wang). 一种针管微流控装置及用其制备相变微胶囊储能材料的方法(A needle based microfluidic device for preparing microencapsulated phase change energy storage materials). 申请号(Application number): CN202310062567.0 (发明专利) (Invention patent)

List of Figures

List of Tables

Chapter 1- Introduction

1.1. Background

As the economy grows rapidly, there is a rising global demand for energy. However, the continuous development of non-renewable energy has had an irreversible impact on the environment, and the problem of energy shortage has become increasingly serious. Therefore, in recent years, the issue of how to effectively improve the energy utilization rate has aroused widespread concern, among which new energy storage materials are the current research focus. Phase change materials (PCMs) exhibit exceptional heat storage capabilities, efficiently absorbing and releasing substantial energy during phase transitions [1]which have been widely used in many fields, including solar energy storage systems, industrial waste heat recovery, building temperature control, and thermal comfort textiles.

1.2. Classification of PCMs

PCMs can be categorized into three primary types based on their chemical composition: inorganic, organic, and eutectic PCMs [2], as illustrated in Figure 1.1.

Within the organic PCM category, a further subdivision can be made into two sub-categories: paraffin and non-paraffin compounds [2]. Paraffin PCMs are composed of linear alkanes, characterized by the molecular formula C_nH_{2n+2}. These materials offer several key advantages, including substantial heats of fusion, chemical stability, safety, compatibility with non-corrosive metal containers, and cost-effectiveness [3]. Their versatility allows for compatibility with a wide range of encapsulating materials, making them a popular choice [4]. Non-paraffin PCMs represent

the largest group and encompass fatty acids, fatty alcohols, and esters. Fatty acids are typically carboxylic acids consisting of long aliphatic chains, which can be saturated or unsaturated. Fatty alcohols, on the other hand, are primarily linear-chain primary alcohols with carbon atoms ranging from 4-6 to 22-26 [5]. Despite their distinct characteristics, non-paraffin PCMs share common features, including a high heat of fusion, the ability to undergo phase changes without supercooling, widespread availability, and cost-effectiveness [3]. These qualities render them suitable for numerous applications [6, 7]. Inorganic PCMs, in contrast to their organic counterparts consisting of carbon, hydrogen, and oxygen atoms, are composed of non-carbon-based substances such as salt hydrates, salts, metallic compounds, and metal alloys. While these materials offer higher energy storage density and thermal conductivity compared to organic PCMs, they do come with certain drawbacks, including issues with corrosion and a propensity for supercooling. Additionally, their operational temperature range is generally higher when compared to organic PCM options [7, 8]. Eutectic PCMs refer to mixtures comprising two or more compounds, typically a combination of organic-organic, organic-inorganic, or inorganic-inorganic materials. A notable advantage of eutectic PCMs lies in their ability to attain specific melting points by adjusting the proportions of each component within the mixture. In a eutectic PCM, the blending of two or more materials results in a substance with a lower melting point than any individual component. Upon heating, this material melts and absorbs heat, and upon cooling, it solidifies and releases heat. The eutectic composition provides a well-defined melting point, enhancing the PCM's efficiency in storing and releasing thermal energy [4]. A material's viability as a PCM in various applications hinges on its apt phase change temperature. However, thermal, physical, kinetic, chemical, and economic

attributes also significantly impact PCM performance, storage system traits, and application feasibility. Table 1.1 encompasses crucial properties and the applications for PCMs.

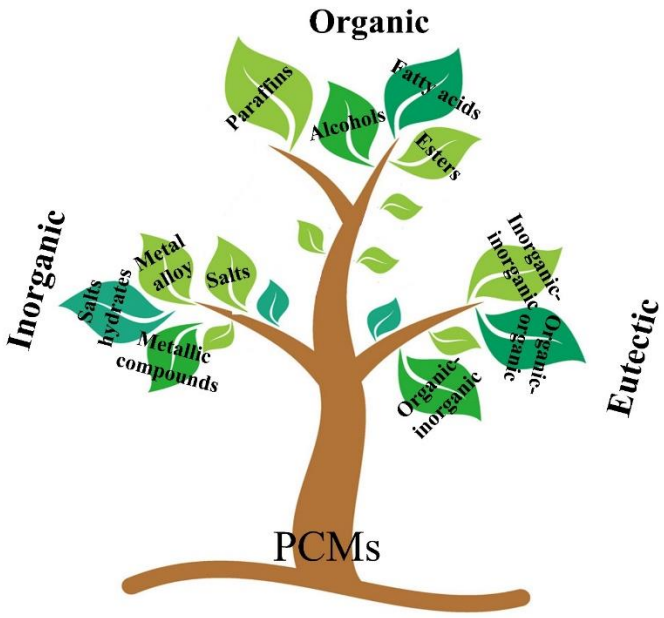

Figure 1-1 Classification of PCMs.

Table 1-1 Advantages, disadvantages, and applications of PCMs [4, 9, 10].

Types of materials	Advantages	Disadvantages	Applications
Organics PCMs	Large temperature range Compatible with other materials	Low thermal conductivity Flammable	Thermal energy storage Building and construction industry

	No supercooling	Relatives large volume changes	Electronics thermal managements
	No separation	Expensive except technical grade paraffin wax	Cold storage and transportation
	Chemically stable		Textile industry
	Safe		Electronics thermal managements
	Non-reactive		Automotive industry
	Easily recycled		Aerospace industry
			Energy-efficient refrigeration
			cosmetics
			Food industry
			Biomedical fields
Inorganic PCMs	High volumetric latent heat	High changed volume	Thermal energy storage
	Easily available	Supercooling	Building and construction industry

	Less expensive	Corrosiveness	Electronics thermal managements
	Higher thermal conductivity		Cold storage and transportation
	High thermal fusion		Textile industry
	lower volumetric variation		Electronics thermal managements
	Non-flammable		Automotive industry
			Aerospace industry
			Energy-efficient refrigeration
Eutectics	Sharp melting point	Limited thermophysical properties data	Thermal energy storage
	High volumetric storage density		Building and construction industry
			Cold storage and transportation
			Electronics thermal managements

1.3. Conventional method for fabricating MEPCM microcapsules

Although PCMs have been widely used as a heat storage medium, in practical applications, pure PCMs have defects as they are vulnerable to leakage, corrosion, phase separation, low thermal conductivity and volume change, etc. [11]. In contrast, if microencapsulation/microfiber packaging is carried out before PCMs are used for energy storage, due to the encapsulation of solid shells, microencapsulated phase change materials (MEPCM) microcapsules have greater advantages over unpackaged microcapsules in terms of storage, transportation, and application. Besides, as the graphene can improve the heat transfer by coroperate with shell material and a solid shell can prevent the interaction of nuclear PCMs with the outside environment, it can not only improve the stability, specific surface area, and heat transfer efficiency of the unpacked PCM, but also solve the problems of PCM leakage, phase separation, and corrosivity.

In fact, because of the above advantages of MEPCM microcapsules, they have currently been widely used in the fields of building energy conservation [12-15], thermal storage and temperature regulation textiles [16, 17], military [18], and functional thermal fluids [19-21]. Until now, many methods have been developed to fabricate MEPCM microcapsules. Table 1.2 shows the conventional microencapsulation methods of PCMs. On the one hand, the early physical methods caused violent flows, poor microcapsule uniformity, and limitations in core-shell material selection [22, 23], and chemical methods restrict material choices and require highly reactive monomers. On the other hand, the traditional MEPCM fiber preparation lacks precise control, resulting in incomplete core-shell structures, PCM leakage, and reduced phase-change latent heat [24-28].

Table 1-2 Conventional microencapsulation methods of PCMs

Physical synthesis methods	**Physical chemical synthesis methods**	**Chemical synthesis methods**
Electrostatic encapsulation [29]	Sol–gel encapsulation [22]	Suspension polymerization [30]
Spray-drying [31]	Coacervation [23]	In situ polymerization [32]
One-step method [33]	Supercritical CO_2-assisted [34]	Emulsion polymerization [35]
-	-	Dispersion polymerization [36]
-	-	Interfacial polymerization [37]

In recent years, microfluidic technology is considered to be a favorable tool for preparing functional material precursors by virtue of its ability to accurately control a small amount of fluids in microchannels with small cross-sectional dimensions [38-40]. It can be seen from previous studies [41-43] that microfluidic technology can accurately control the formation and stability of fluid interface. On the basis of obtaining multiple emulsion templates and laminar liquid lines, precise and controllable microcapsules and microfiber structures can be obtained by reacting or

curing at the phase interface, which can be helpful to confine corrosive or toxic materials, enclose powder materials, and control the release of different compounds. Due to these advantages, microencapsulation has been employed for the confinement of a wide range of compounds that include: bacteria, drugs and cells in the pharmaceutical and biomedicine and field; additives used in cosmetic and food industries [44-48]. Specially, with the unique advantages of microfluidic technology in the field of controllable preparation of microcapsules and microfiber functional materials, through precise control of the structure of MEPCM microcapsules, the encapsulation rate, and monodispersity of MEPCM microcapsules can be effectively improved. Generally, the heat transfer can be enhanced by improving the thermal conductivity of PCM. Highly conductive nanoparticles such as Al2O3 and graphene nanoparticles [32] are added to PCM to improve the thermal conductivity.

Recently, the effect of microencapsulated and suspended PCM in a conventional singlephase heat transfer fluid to form phase change slurry has been investigated. The slurry can serve not only as the thermal storage media but also as the heat transfer fluid.

Chapter 2-Literatue review

The Phase change heat transfer is very important to evaluate the performance of MEPCMs and design LHTES systems. It has been extensively studied and significant advancements have been achieved. The critical studies are reviewed in Section 2.1 and Section 2.2 respectively.

2.1. MEPCM fabrication based on microfluidic technology

There are some landmark nodes in the development history of microfluidics-based microcapsules, as illustrated in Figure 2.1.

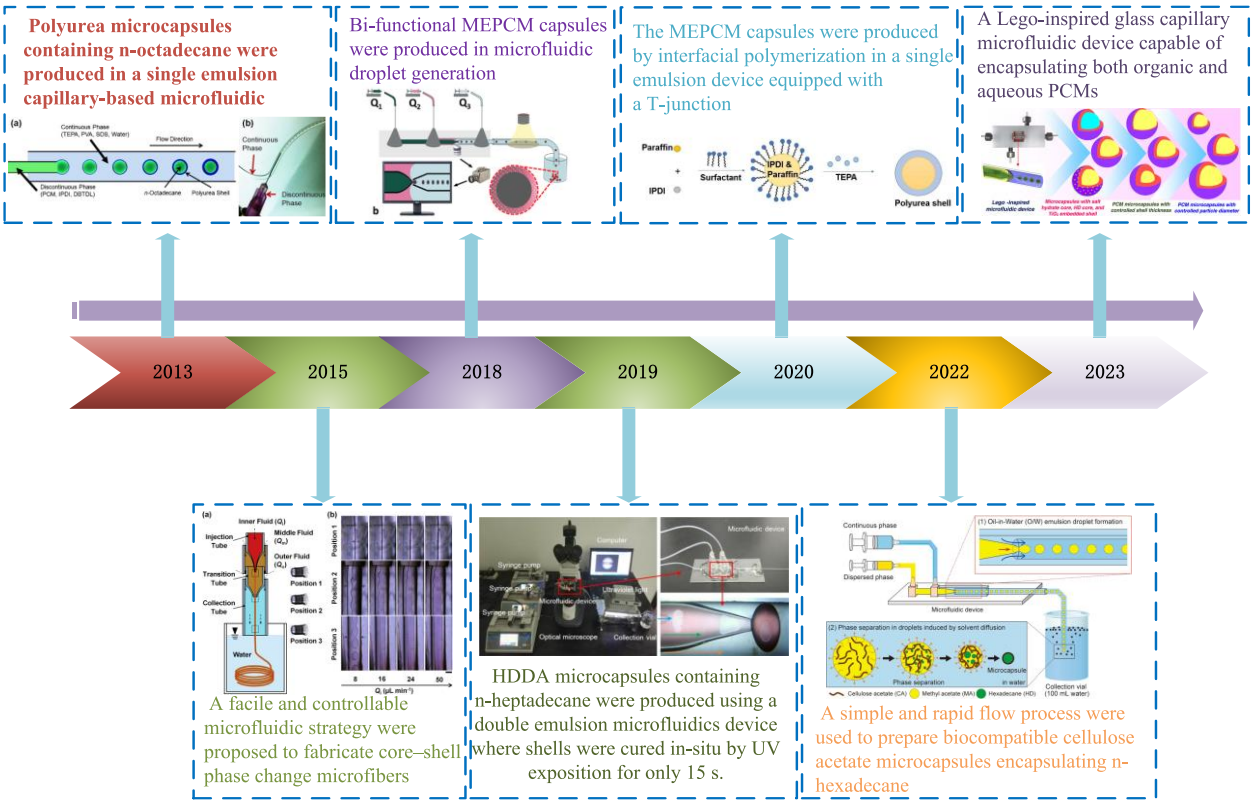

Figure 2-1 Timeline of the development history for MEPCM microcapsules [49-55].

The geometry of microfluidic devices that can be used to prepare MEPCM microcapsules is first introduced. In addition, the theoretical model of MEPCM microcapsules are discussed, and the general preparation and properties of MEPCM microcapsules reported so far are summarized.

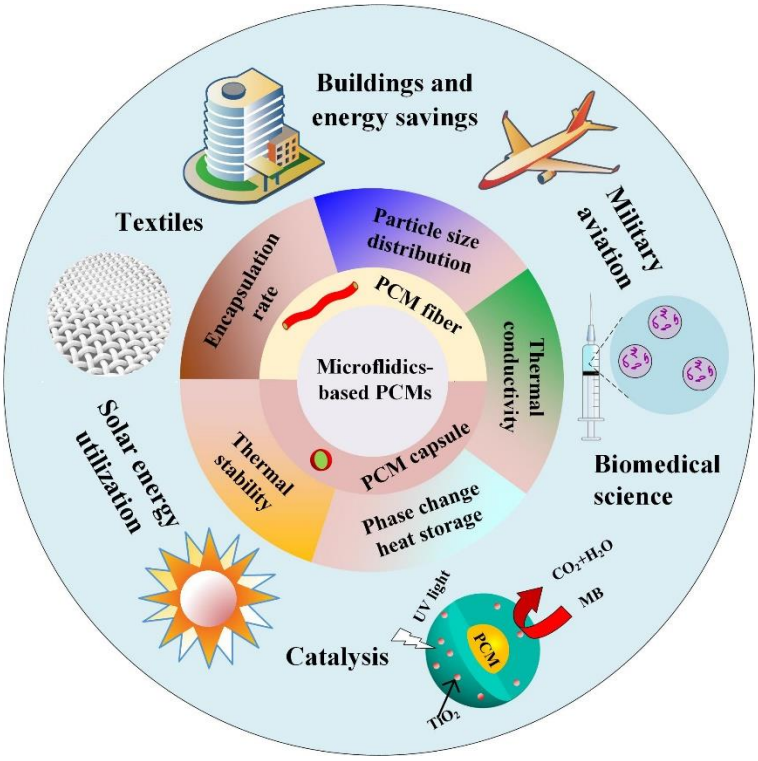

Figure 2-2 The outline of microfluidics-based PCMs from fabrication to applications.

2.1.1. Microfluidic-based double emulsion/Liquid line template formation

The double-phase microfluidic encapsulation method is developed based on microfluidic technology, which has the advantage of precise manipulation of low flow fluid interfaces in micro-channels. It is considered as a favorable tool for the preparation of functional materials, such as those applied in the fields of pharmaceuticals, foods, and phase change energy storages [42, 43, 56-59]. The key to the preparation of functional materials by double-phase microfluidic encapsulation is to first form double emulsion and laminar liquid lines with highly controllable structure, high coverage, and good monodispersity through microfluidic technology [41].

a) Double emulsion formation

Microfluidic technology is characterized by small size, automation, and high integration. It enables the stable and continuous preparation of monodisperse droplets even under low flow rate conditions. It can precisely control the size and structure of a single droplet to ensure the high encapsulation rate of internal droplets. Therefore, microfluidic technology shows incomparable advantages in the continuous and controllable generation of double emulsion. On the one hand, microfluidic chips can be categorized into two-dimensional and three-dimensional based on their structure and design, which have been developed for preparing double emulsion based on their applications. Two-dimensional microfluidic chips are usually fabricated in silicon and glass substrates using lithography and etching techniques, or in polymer substrates such as polydimethylsiloxane (PDMS) by soft lithography [60], while three-dimensional microfluidic chips are usually assembled and constructed by glass capillaries. On the other hand, microfluidic chips are classified into non-coaxial and coaxial based on their functionality and the arrangement of fluid flow within the chip. The non-coaxial T-shaped cross-flow microfluidic device [61] is shown in Figure 2.3A, where the flow directions of the internal and external fluids are perpendicular to each other. The internal fluid breaks into droplets at the intersection of the T-shaped flow channel mainly due to the shearing and extrusion caused by the external fluid. Figure 2.3B and C show two typical coaxial flow forms: co-flow type and flow-focusing type. In this device, the flow directions of internal phase and external phase fluids are located on the same axis, and the fracture generation of droplets in this device is generally affected by the viscous and shear stress of internal phase and external phase fluids.

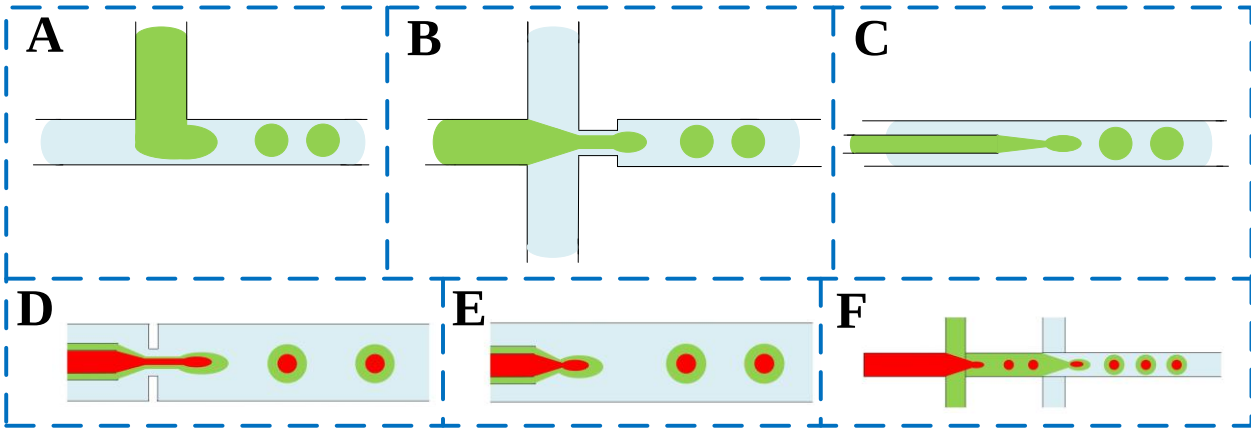

Figure 2-3 Junction geometries A: cross-flow, B: flow-focusing, and C: co-flow; D: Flow-focusing microfluidic device [62]; E: Coaxial co-flow microfluidic device [63] ; F: Dual cross-sectional microfluidic device [64]

Until now, researchers have studied the stable formation of double and multiple emulsions in microfluidic devices. Utada [62] constructed a flow-focused microfluidic device, as shown in Figure 2.3D. The experiment showed that multi-emulsion prepared by the device has high monodispersity, and the multi-emulsion with different shell thickness and different number of inner core droplets can be controlled by adjusting the three-phase flow rate independently. In order to obtain double emulsion with an ultra-thin shell, Kim et al. [65] reformed the above device and placed the internal phase tube inside the mesophase tube, so that the internal phase can form a jet in the mesophase during the flow process and then pass through the focusing hole with the external phase, thus realizing the high-frequency preparation of double emulsion with a thickness of only tens of nanometers. In addition to the flow-focusing device, the three-dimensional coaxial co-flow microfluidic device is also widely used in emulsion preparation. Fischer and Utada et al. [66, 67] studied the influence of physical parameters and velocity of each phase on droplet generation in

coaxial microfluidic devices through experiments, and observed two typical flow patterns and their conversion laws. On the basis of elucidating the droplet formation mechanism and the evolution law of main flow patterns in the co-flow device, various co-flow microfluidic devices for generating multiple emulsions with complex structures are constantly emerging. Chu et al. [63] assembled a three-dimensional co-flow microfluidic device in multiple stages, as shown in Figure 2.3E. First, they obtained double emulsion with highly controllable internal droplet nuclei. On this basis, adding a first-stage co-flow device can realize the regulation of the droplet size and the number of nuclei in the triple emulsion, and at the same time, it can ensure that the CV value of the prepared multiple emulsion is less than 1.5%. Wu et al. [68] compared the differences between the two experimental devices of co-flow and flow-focusing in the production of the simplest dual lotion through experiments. The results showed that the co-flow microfluidic device has the advantages of a stable production process and good repeatability in the preparation of double emulsion. More importantly, its monodispersity in the production of double emulsion is better than that of the flow-focusing microfluidic device. In addition to the flow-focusing and co-flow microfluidic device, the cross-sectional microfluidic device has also been used for producing double emulsions. Pannacci et al. [64] found through experiments that the cross channel has better control over the generation of double emulsion droplets than the T-channel, as shown in Figure 2.3F. Saeki et al. [69] found that if both cross channels have hydrophobic walls, and the depth of the first channel is the same as that of the central main channel, but smaller than the depth of the second channel, ultra-thin (<1 μm) W/O droplets can be formed.

In addition to the experimental study, the hydrodynamic behavior of double and multi-emulsion formation in microfluidic devices has also been numerically simulated to provide insights into the

droplet production mechanism [70, 71]. Zhou et al. [72] combined the finite element method with an adaptive grid to carry out numerical simulation and studied the formation process of single droplet and double emulsion in a flow-focusing microfluidic device and their corresponding influencing factors. It was found that the encapsulation state and encapsulation efficiency of composite droplets in the device depended on the viscosity ratio and capillary number. Vu et al. [73] used a forward tracking/finite difference method to track the unsteady evolution and rupture process of composite jet under Navier-Stokes program control system of incompressible Newtonian fluid. The results showed that the Reynolds number and Weber number of the internal phase fluid determined whether the composite jet breaks down in a drop mode or a spray mode to form droplets. In addition, the influence of velocity ratio (mesophase velocity ratio internal phase velocity, external phase velocity ratio internal phase velocity) on flow pattern transformation is also discussed. Liu et al. [68] compared the formation mechanism and process of multiple emulsions in two axisymmetric coaxial microfluidic devices by numerical simulation and expounded the influence of flow conditions and local geometry of the device on the formation of double emulsions. It was found that the existence of focusing holes in the flow-focusing microfluidic device was helpful to accelerate the fracture of the neck to form double emulsions under drip flow pattern and promote the formation of jet segments under spray flow pattern. The radius of focusing hole had an important influence on the formation of double emulsion, but the length of focusing hole had little influence on it. At the same time, the relationship between the dimensionless focusing hole radius and the capillary number of continuous phase fluid and the generated flow pattern in microfluidic devices was quantitatively described. Based on the above analysis, it can be seen that there have been many experiments and numerical simulation studies

on the stable generation of multiple emulsion templates in microfluidic devices and their precise structural regulation, which provide important guidance for the related research on controllable preparation of microspheres and microcapsule materials with good structural size uniformity.

b) Laminar liquid line template formation

In addition to producing double emulsion droplets, microfluidic technology has been considered as a favorable tool for continuous preparation of laminar liquid lines of functional microfiber materials by virtue of precise manipulation of fluids in non-coaxial T-shaped cross-flow, coaxial co-flow and coaxial flow-focusing microfluidic device, as shown in Figure 2.4A, B and C. Guillot et al. [74] used the theory of absolute instability and convection instability to explain the stability of laminar liquid line formation in the cross-flow process. In simple terms, absolute instability means that the disturbance will grow and spread from a fixed point to the upstream and downstream directions. In this case, the jet cannot be formed continuously but breaks into droplets. On the contrary, the interference in the so-called convective instability only grows and propagates in the downstream direction, which allows a long continuous liquid line to persist. Research has shown that this situation generally occurs when the working fluid velocity is large and the inertia effect of the fluid is more important than the surface tension effect [74]. The preparation process of double emulsion templates in microfluidic chips is related to many parameters such as flow velocity, viscosity, interfacial tension, and device geometry. Humphry et al. [75] found that when the width of the dispersed phase jet section is equal to or greater than the channel height in the device, its instability can be suppressed. The geometric constraints of the device can be used to suppress jet instability, promoting the stable generation of laminar liquid lines. Additionally, experimental research [76] showed that the tensile viscosity of non-Newtonian fluid as a dispersed

phase solution resists the extrusion required to form droplets, leading to the formation of long jet state. The dispersed phase of non-Newtonian fluid with high viscosity could effectively suppress the instability caused by the generation of laminar liquid lines in the flow-focusing device. Recently, in order to obtain fiber materials with structural diversity, higher requirements have been put forward for the construction of laminar liquid lines in the flow-focusing, co-flow or flow-focusing microfluidic device, as shown in Figure 2.4D, E and F. Yunru et al. [77] used a glass capillary to construct various microfluidic devices with special structures to form multi-pattern laminar liquid lines, as shown in Figure 2.4D, making it possible to prepare microfibers in different fields. This review mentions that multiple capillaries can be used in parallel as internal injection tubes, allowing various fluids flowing in the capillaries to not mix with each other before entering the collection channel for solidification, so microfibers with multi-chamber structure can be prepared. A laminar liquid line with nested structure can be generated by nesting and assembling multiple capillaries as internal injection tubes. At present, theoretical and experimental research on the factors affecting the stability of laminar liquidus has been quite rich, and there have been related studies on the construction of laminar liquidus with different structures. These flexible flow forms can be applied to the creation of ultrafine fibers with novel three-dimensional structures.

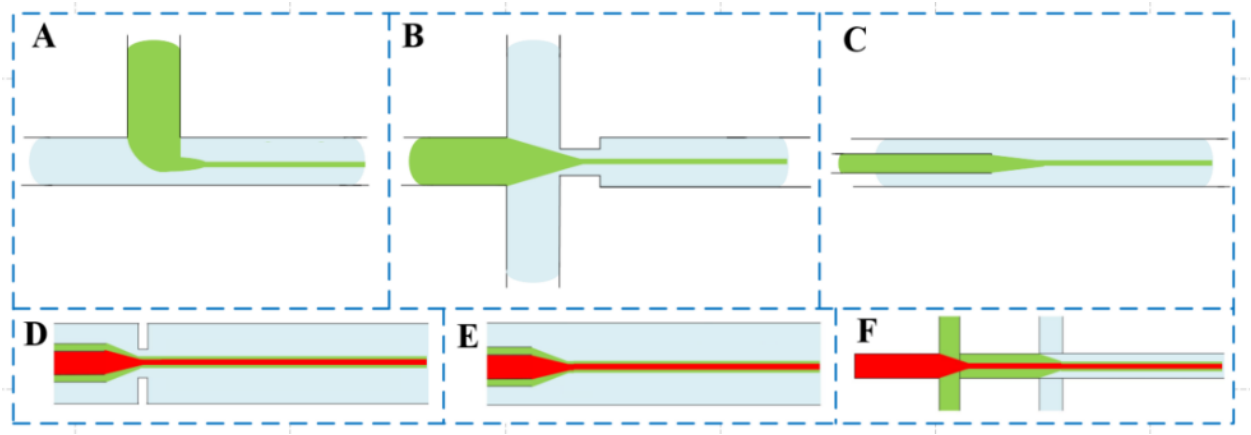

Figure 2-4 Laminar liquid line template formation; Junction geometries A: Cross-flow, B: Flow-focusing, and C: Co-flow; D: Flow-focusing microfluidic device [77]; E: Coaxial co-flow microfluidic device; F: Dual cross-sectional microfluidic device.

2.1.2. Heat transfer model of MEPCMs

Figure 2.5 shows the physical model of the PCM capsule, which comprises a sphere PCM core encapsulated by shell material. When the phase change of PCM core occur within a certain temperature range, there will be three zones with different states, including a solid zone, mushy zone and liquid zone, within the material. In dealing with the melting process of a multicomponent core-and-shell MEPCM capsule, a mathematical model is constructed based on specific assumptions [78, 79]. (1) The core encompasses both phase change material (PCM) and doping elements, (2) with the capsule's size enabling the omission of thermal convection effects in the PCM's liquid phase; (3) the core PCM experiences solid and liquid states with consistent thermophysical traits, alongside a mushy zone characterized by evolving properties. Notably, (4) the shell's characteristics remain unaffected by PCM volume changes. (5) Homogeneity characterizes the capsule's inner region.

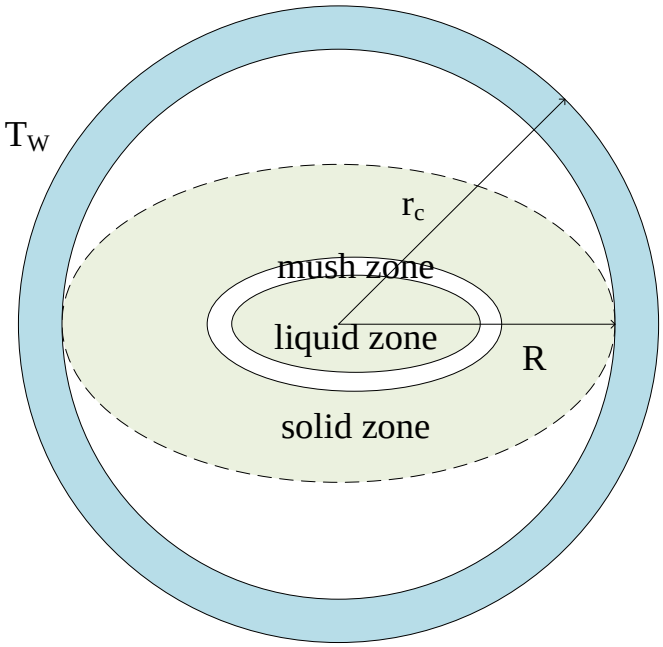

Figure 2-5 Simplified model of PCM capsule.

Leveraging these assumptions, the moving boundary problem is addressed using the apparent heat capacity method [78, 79]. The ensuing model encapsulates the entire MEPCM capsule, with the energy equation expressed in spherical coordinates as:

$$C^* \frac{\partial T}{\partial t} = \frac{1}{r^2} \frac{\partial}{\partial r}\left(r^2 \lambda^* \frac{\partial T}{\partial r}\right) \tag{2.1}$$

where C^* is the effective thermal capacity (J Kg^{-1} K^{-1}) of the ME-PCM capsule, T is the temperature (K), t is the time (s), r is the radius (m), and λ^* is the effective thermal conductivity (W m^{-1} K^{-1}). With an initial temperature of T_0, the MEPCM capsule's outer shell temperature is elevated to T_s due to an external heat source. The boundary condition can be expressed as

$$T|_{t=0} = T_0, 0 \le r \le r_c \tag{2.2}$$

$$\frac{\partial T}{\partial r}|_{r=0} = 0, t > 0 \tag{2.3}$$

$$T|_{r=r_c} = T_s, t > 0 \tag{2.4}$$

Where r_c is the radius of the core. The effective thermal capacity C^* in Equation (2.1) can be given as

$$C^* = \begin{cases} \sum m_c C_c, 0 \le r \le r_c \\ C_s, r_c \le r \le r_{cap} \end{cases} \tag{2.5}$$

where m_c and C_c denote the mass and thermal capacity of individual core components, while C_s represents the thermal capacity of the shell, and rcap stands for the radius of the ME-PCM capsule. Within the core's components, the effective thermal capacity of the PCM (C_p) necessitates consideration of latent heat across the phase change temperature range ($T_p + \Delta T$). This can be expressed as follows:

$$C_p = \begin{cases} C_{p,s}, & T < (T_p - \Delta T) \\ \dfrac{\rho_p H_p}{2\Delta T} + \dfrac{C_{p,s} + C_{p,l}}{2}, & (T_p - \Delta T) \le T \le (T_p + \Delta T) \\ C_{p,l}, & T > (T_p - \Delta T) \end{cases} \tag{2.6}$$

Here, $C_{p,s}$ and $C_{p,l}$ represent the thermal capacity of the PCM in its solid and liquid states, respectively. ρ_p pertains to the effective density of the PCM for both phases, while H_p signifies the PCM's latent heat. T_p stands for the average phase change temperature, and ΔT corresponds to half of the phase change temperature difference. Moreover, the expression for effective thermal conductivity, λ^*, as in Equation (2.1), can be formulated as follows:

$$\lambda^* = \begin{cases} \lambda_c, & 0 < r \le r_c \\ \lambda_s, & r_c < r \le r_{cap} \end{cases} \tag{2.7}$$

λ_c and λ_s represent the effective thermal conductivity of the core and shell, respectively. In the

case of MEPCM fibers, the energy equation and associated boundary conditions are transformed into a framework based on cylindrical coordinates.

2.2. Fabrication of MEPCMs microcapsules

From the above research, it can be seen that microfluidic technology can accurately control the formation and stability of fluid interface. MEPCM microcapsules with precisely controllable microstructure can be obtained by reacting or curing at the external interface of double emulsion and laminar liquidus, based on the two types of microfluidic encapsulated templates with stable phase interface.

2.2.1. Fabrication of MEPCM microcapsules

Researchers have done a lot of experimental and simulation studies on the formation of double emulsion in microfluidic devices. At present, the microfluidic encapsulation method based on double emulsion has become an important method for preparing MEPCM microcapsules.

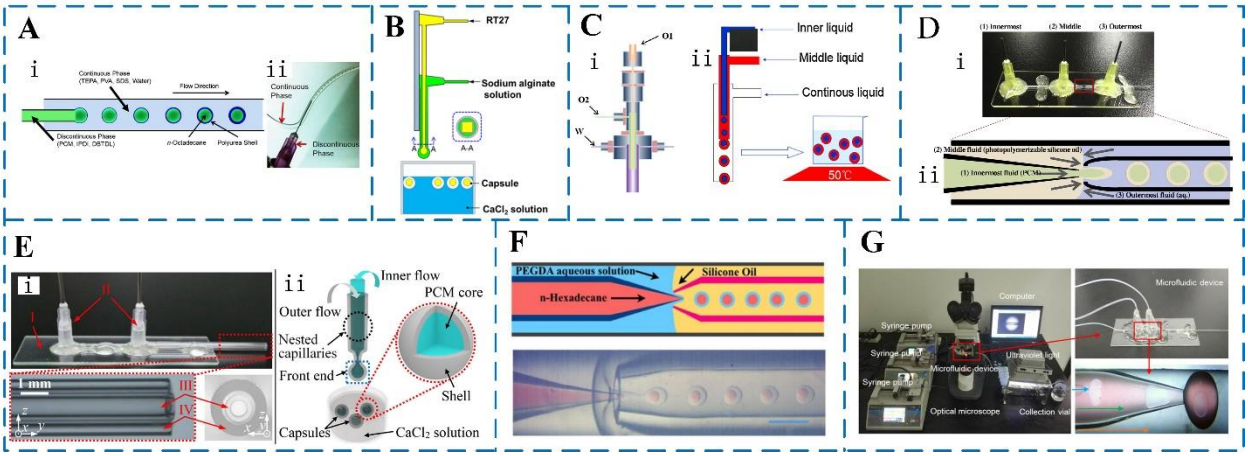

Figure 2-6 A: (i) schematic diagram of the process of creating monodisperse PCM@polyurea microcapsules in a tubular microfluidic device and (ii) photograph of the oil-in-water PCM

droplets produced at the tubular junction. Emulsification and partial polycondensation of the PCM and polyurea in the flow stream at 35°C [49]; B: Schematic illustration of the equipment and process used to prepare RT27/Ca-alginate microcapsules [80]; C: (i) the microfluidic device and (ii) the process used to fabricate double emulsions [81] ; D: (i) The glass capillary device and (ii) the process used to prepare double emulsion droplets as templates for the MEPCM microcapsules [82];E: Gravity-assisted co-flowing microfluidic device (I: glass slide, II: dispensing needles, III: inner capillary, IV: outer capillary) [52]; F: Schematic of microfluidics device [83]; G:Three-phase microfluidic device for the fabrication of MEPCM microcapsules [84].

Based on a tubular microfluidic technology, Lone et al. [49] prepared a MEPCM microcapsules with a core material of n-octadecane and a shell material of polyuria, as shown in Figure 2.6A. The results showed that the monodisperse particle size of MEPCM microcapsules could be controlled by changing the flow rate or aqueous solution. However, the polyurea shell is too thin and wrinkled, making it difficult to provide effective protection for the MEPCM microcapsules under thermal cycling conditions, possibly because the strict time and temperature requirements of the thermal curing process cannot be met in microfluidic devices. Therefore, new microfluidic technologies were further developed to manufacture double emulsion templates for generating MEPCM microcapsules [85]. For example, Liang [80] developed a simple and easy-to-control method for encapsulating PCM with calcium alginate, a biocompatible and non-toxic material. This was achieved using a microfluidic device, as shown in Figure 2.6B. The study found that adjusting the inner flow rate was more effective than adjusting the outer flow rate for controlling the size of the MEPCM microcapsules and the content of RT27, which is a type of PCM. Besides,

the MEPCM microcapsules produced using this method showed good thermo-regulating ability and were stable and reproducible. Similarly, Fu et al. [81] prepared MEPCM microcapsules with silicone resin as the shell and n-cetyl bromide as core based on co-flow microfluidics, as shown in Figure 2.6C. The findings of the study indicated that the microcapsules had a high energy storage capacity. Specifically, the melting enthalpy and freezing enthalpy of the microcapsules were measured to be 76.35 J/g and 78.67 J/g, respectively. Moreover, the thermal curing process used in the study mentioned earlier [80] typically requires several hours to complete the polymerization process [86]. However, an alternative method for polymerization is ultraviolet (UV) radiation curing, which is a photopolymerization technology that enables liquid resins to be rapidly converted into solid polymers without the use of solvents. Many studies have shown that UV curable materials have better mechanical properties than thermal curing materials [87-90]. Based on this, Akamatsu et al. [82] used a simple capillary microfluidic method (Figure 2.6D) to prepare encapsulated n-tetradecane and n-hexadecane in a silicone resin shell with the help of UV curing. The study demonstrated that the MEPCM microcapsules produced were suitable for thermal energy storage, as the stable phase transition of the microcapsules was directly observed. In a similar study, Li et al. [52] used a co-flow capillary microfluidic device and UV curing technique (as shown in Figure 2.6E) to prepare MEPCM microcapsules with n-heptane as the core and hexanediol diacrylate (HDDA) polymer as the shell. The resulting MEPCM microcapsules had a uniform particle size, smooth surface, and regular spherical shape. In addition, in order to explore the possibility of core materials for MEPCM microcapsules, Han et al. [83] proposed a microfluidic device (Figure 2.6F) for the precise manufacture of MEPCM microcapsules with adjustable thermal properties. The study found that both organic and inorganic MEPCM

microcapsules had excellent properties such as high monodispersity, good energy storage capacity, high encapsulation efficiency, and thermal stability.

However, the low thermal conductivity of commonly used PCM inhibits the overall thermal performance, such as thermal storage, thermal response, and heat release speed of MEPCM microcapsules in practical applications [91]. Therefore, in order to improve the heat conductivity of MEPCM microcapsules, Hao et al. [84] prepared microcapsules based on the microfluidic method (Figure 2.6G). To enhance the thermal conductivity of the pure PCM and improve the thermal regulation ability of the MEPCM microcapsules, multi-layer graphene was added to the PCM. The study found that the resulting microcapsules had a stable core-shell structure and high monodispersity. The size and core/shell ratio, which determines the thermal adjustment capability, could be accurately controlled by adjusting the flow rates of the inner and outer phases (as shown in Figure 2.7A and B). Additionally, the addition of multi-layer graphene (up to 2 wt%) improved the thermal conductivity of the microcapsules, while the energy storage capacity degradation was less than 5%. This allowed the MEPCM microcapsules to respond faster to changes in the surrounding thermal environment. Although all of these microfluidic devices can produce uniform and high packaging rate phase change PCMs, they are difficult to manufacture. In common glass capillary devices, not only is it troublesome, but also due to the adhesion between the capillary and the needle, it is impossible to adjust the internal structure during the preparation process [92]. In addition, PDMS channels not only rely heavily on expensive silicon master modules, but also are sensitive to organic solvents [93]. To solve these problems, Parvate et al [94] proposed a Lego-inspired microfluidic device to produce MEPCM microcapsules with a movable UV polymerization. The microfluidic device used in the study consisted of a coaxial glass capillary

and computer numerical control-milled blocks that could be easily connected and taken apart using a Stud-and-Tube system inspired by Lego blocks. The study found that the thickness of the shell and the diameter of the particles in the microcapsules could be accurately controlled by adjusting the fluid rate and capillary geometry. Table 2.1 provides a summary of the morphological characteristics and thermal properties of some MEPCM microcapsules that were prepared using microfluidic methods.

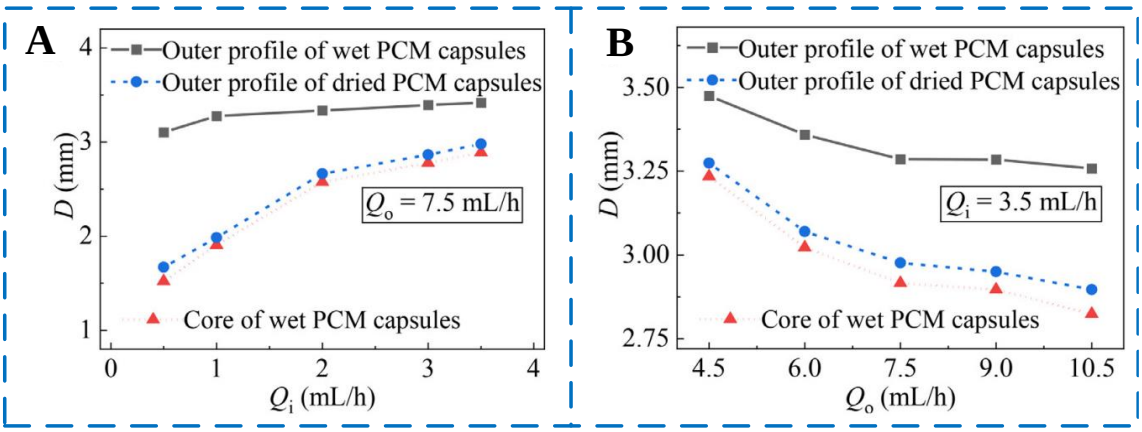

Figure 2-7 The relationship between the detailed diameters on the rates of the A: inner flow Q_i and B: outer flow Q_o [84].

Table 2-1 Thermal properties and morphological characteristics of MEPCM microcapsules

Ref.	Microfluidic	Device	Emulsions	Phases	Curing method	Core material	Shell material	Capsule size (μm)	ΔH_m (J g^{-1})	T_m (°C)	ΔH_c (J g^{-1})	T_c (°C)	W (%)	E (%)	CV
[82]	Flow-focusing	Glass capillary	Double	O/O/W	UV radiation	n-tetradecane/n-hexadecane	Photopolymerizable oil	120–200	96	19.1		8.4	44		High monodispersity
[95]	Flow-focusing	Glass capillary	Double	W/O/W	UV radiation	sodium acetate trihydrate aqueous solution	Acrylate/polystyrene	250–280	-	1.7	-	-48.3	-		Poor concentricity
[83]	Flow-focusing	Glass capillary	Double	O/WO and W/O/O	UV radiation	n-hexadecane	PEGDA/ETPTA	200–300	269.3 J g^{-1}	19.1/8	212.5	5.8/-24	87.8	82.9	<2%
[55]	T-junctions	Tubular	Single	O/W	Interfacial Polymerization	Paraffin	Polystyrene	500	87.5	29.1	94.9	24.5	96.5	96.0	<2.5%
[81]	Co-flow + collector	Tubular	Double	O/O/W	Chemically crosslinked	n-hexadecyl bromide	Elastic silicone	460	76.35	16	78.67	6	49	-	<3%

[96]	Co-flow	Glass capillary	Single	W/O	Sol-Gel	$Na_2SO_4 \cdot 10H_2O$	SiO_2 microparticles	400-600	-	34.71	25.89	-	47.07 %	2.79%
[49]	Co-flow	Glass capillary	Single	O/W	In situ Polycondensation	n-octadecane	polyurea	35–500	169.7	35	165.7	25	-	-	<3%
[80]	Co-flow	Glass capillary	Single	O/W	Physically cross linked	RT27	Ca-alginate	2600–4200	179.4	27	178.5	27	-	94.68 %	<3%
[52]	Co-flow	Glass capillary	Double	O/O/W	UV radiation	n-heptadecane	HDDA	30–150	161.6	8 and 21.2	159.7	7.6 and 21.3	73.72	73.36	<2%
[84]	Co-flow	Glass capillary	Single	W/O	calcium chloride solution ($CaCl_2$)	multilayer graphene and RT25	calcium chloride	1500-3500	150.8	26	153.5	22	84.2		<2%
[50]	Co-flow	Glass capillary	Double	O/O/W and W/O/W	UV radiation	hexadecane or salthydrate EK	norland optical adhesive SP21	250-260	157	20.3	158	16.4	65.4	62.0	<3%

[53]	Co-flow	Glass capillary	Single	O/W	cross-linking	n-hexadecane	cellulose acetate	45-89	178	16.9	176	18.5	66	<11.3%
[97]	Co-flow	Glass capillary	Double	W/O/W	UV radiation	OP18E	HDDA	about 475	19.8	19.09	18.12	12.18		

2.2.1. Fabrication of MEPCM fibers

The MEPCM fibers are designed with a core sheath structure, where the PCM and protective layer are used as the core and sheath respectively [98]. This structure allows the fibers to fully utilize the latent heat property of the PCM for temperature regulation and heat storage [99]. To increase the productivity of MEPCM fibers, microfluidic technology is used in the manufacturing process. The process involves two steps. In the first step, a liquid line template is created using microfluidic methods. The sheath material is then cured through subsequent processing to produce the MEPCM fibers. For example, Wen et al. [51] prepared MEPCM fibers with high PCM content based on a simple and controllable microfluidic technology, as shown in Figure 2.8A. It was found that the poly(vinyl butyral) (PVB) polymer shell of the obtained MEPCM fibers effectively prevents the leakage of RT27 during the phase transformation process and the enthalpy of MEPCM fibers increases with the increase of PCM content. The microfibers showed a high encapsulation efficiency of up to 70%, with a maximum melting enthalpy of about 128.2 J/g and a crystallization enthalpy of about 124.0 J/g. To improve the thermal conductivity of MEPCM fibers, researchers can add high thermal conductivity materials such as graphene nanosheets and metal oxides to the sheath [100]. Zhang et al. [100] used the microfluidic method to prepare a composite MEPCM fiber with high thermal conductivity (Figure 2.8B). This fiber consisted of an RT27 core and a PVB sheath mixed with Al_2O_3 nanoparticles. The addition of 12% Al_2O_3 resulted in a 47.1% decrease in melting time and a 39.5% decrease in crystallization time. Table 2.2 provides a summary of the thermal properties and morphological characteristics of various MEPCM fibers.

Table 2-2 Thermal properties and morphological characteristics of some MEPCM fibers.

Ref.	Geometry	Device	Emulsions	Phases	Curing method	Core material	Shell material	Fiber diameter	ΔH_m (J g^{-1})	T_m(°C)	ΔH_c (J g^{-1})	T_c(°C)	W (%)	E (%)
[101]	Co-flow	Glass capillary	Double	O/O/W	Solution extraction	paraffin wax RT27	PVB	320–350 μm	128.2	27.88	-	25.13	-	70
[102]	Co-flow	Glass capillary	Double	O/O/W	Solvent extraction	paraffin wax RT27	MWNT/PVB	400–450 μm	108.67	30		23	-	
[98]	Co-flow	Glass capillary	single	W/O	Solution extraction	Solution extraction	PVB, Al_2O_3 NPs composites	400	73.58	12	-	6	-	96.0
[100]	Co-flow	Glass capillary	Single	O/W/W	Solvent extraction	paraffin wax RT27	PVB, Al_2O_3 NPs composites	400 μm	117.3	26.39	-	23.14	-	64.8

[103]	Co-flow	Glass capillary	Single	O/W	-	PEG1000	polypropylene	850-950 μm	108.4		106.7	20.4	80.3	96.7

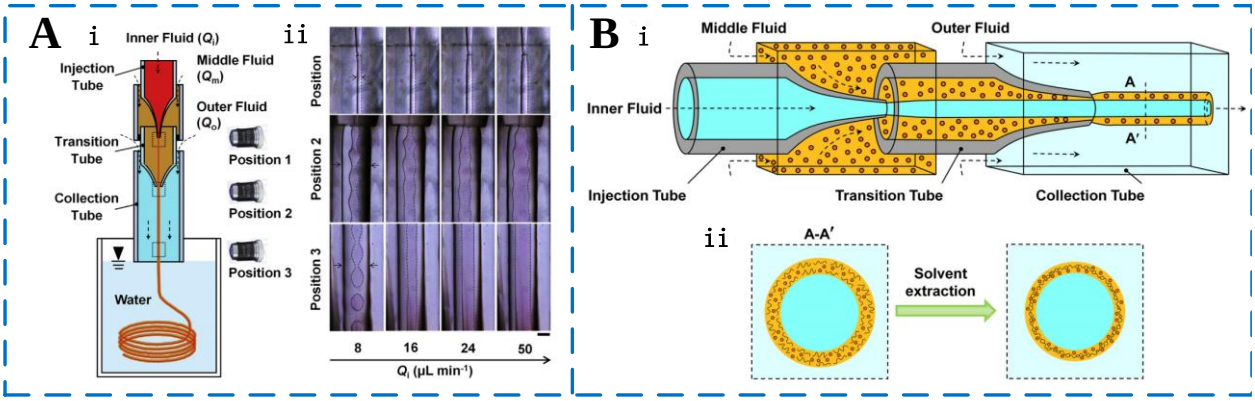

Figure 2-8 A: The setup of coaxial microfluidic device and generation process of MEPCM fibers. (i) Schematic diagram of microfluidic device for producing MEPCM fibers. (ii) high-speed images of a coaxial core-sheath flow consisting of a cylindrical jet of melting RT27 (core fluid) and an annular jet of PVB solution (sheath fluid) at various inner flow rates, Scale bar is 200 mm [51]. B: Schematic illustration of composite phase change microfibers with a core-sheath structure using a microfluidic fabrication process. (i) Micro-device for producing composite microfibers. (ii) Cross sections of the composite microfibers illustrating the solvent extraction process [100].

2.3. Characterization of MEPCM microcapsules

The properties of MEPCM microcapsules, including their physical, chemical, and mechanical characteristics, are greatly affected by the materials used for the core and shell, as well as the method used to synthesize them. These properties are important for the practical use of MEPCMs, and it's crucial to accurately measure and describe them to ensure their effectiveness.

2.3.1. Encapsulation rate

The encapsulation rate of MEPCM microcapsules is an important parameter to evaluate the thermal properties of MEPCMs. MEPCM microcapsules prepared by microfluidic device generally have a high encapsulation rate. Table 2.1 and Table 2.2 show the comparison of the encapsulation efficiency of MEPCM microcapsules prepared by some current microfluidic methods.

The encapsulation rate is an important parameter for evaluating the thermal properties of MEPCM microcapsules. The encapsulation rate of MEPCM microcapsules, also known as the effective load of ME-PCM capsule/fiber, refers to the ratio of the amount of core material covered to the total amount of core material in ME-PCM capsule/fiber. In theory, accurately weighing the mass of the core material in the MEPCM capsule/fiber is difficult. Generally, the melting latent heat of the MEPCM microcapsules measured by DSC can be compared with the melting latent heat of the pure phase change material to calculate the encapsulation efficiency, as shown in Equation (2.8) [79].

$$E = \frac{\Delta H_{m,\mathrm{ME-PCM\ capsule/fiber}}}{\Delta H_{m,PCM}} \times 100\% \tag{2.8}$$

where E is the encapsulation efficiency of MEPCM microcapsules; $\Delta H_{m,\mathrm{ME-PCM\ capsule/fiber}}$ and $\Delta H_{m,PCM}$ are, respectively, the melting latent heat of MEPCM microcapsules and core material. MEPCM capsule/fiber prepared by microfluidic device generally has a high encapsulation rate.

Table 2.1 and Table 2.2 show the comparison of the encapsulation efficiency of MEPCM microcapsules prepared by some current microfluidic methods.

2.3.2. Particle size distribution

The particle size distribution of MEPCM microcapsules will directly affect their thermal and mechanical properties. For the same MEPCM microcapsules with the same wall thickness, the smaller the particle size is, the shorter the heat transfer distance of the core material is, and the higher the heat transfer efficiency is, but it will affect the stored energy density. At the same time, smaller particles have higher mechanical strength. Scanning electron microscopy (SEM) and optical microscopy (OM) can be used to evaluate the particle size and morphological characteristics of microcapsules, while a laser particle size analyzer can explore the particle size distribution of microcapsules.

From the SEM image shown in Figure 2.9(A-E), the MEPCM microcapsules prepared by conventional methods have poor monodispersity. The size of the microcapsules and the content of PCMs are not controllable, which will also cause a great waste of reagents and increase the preparation cost of MEPCM microcapsules. Figure 10F shows the SEM diagram of the MEPCM fiber prepared by the conventional electrospinning method.

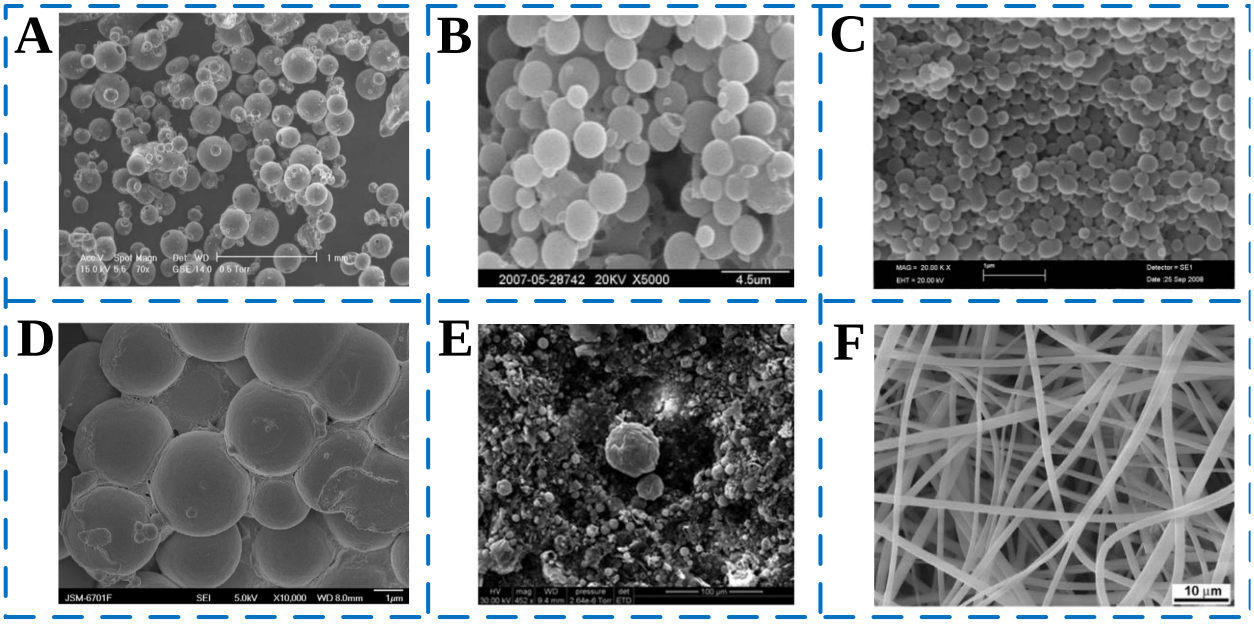

Figure 2-9 SEM micrographs of MEPCM microcapsules / MEPCM fiber prepared by conventional methods. A: Suspension polymerization [30]; B: In situ polymerization [104]; C: Emulsion polymerization [35]; D: Dispersion polymerization [36]; E: Interfacial polymerization [105]; F: Electrospinning [27].

In Figure 2.10A and B, an SEM image and corresponding particle size distribution are shown for MEPCMs produced using double-emulsion droplet templating. The MEPCMs have a highly uniform size distribution, with only a 6 μm difference between the maximum and minimum sizes. The calculated coefficient of variation in size (C_v) is approximately 1%, indicating that combining three-phase microfluidics and radiation curing approaches can result in MEPCMs with high uniformity and monodispersity [52]. Due to the incomplete or broken outer shell of MEPCM microcapsules, there is a risk of leakage of internal PCMs, which would lead to the loss of protection for the core material. Therefore, it is necessary to study the morphology and microstructure of microcapsules. Due to the fine regulation of interfacial tension by microfluidics,

the resulting MEPCM microcapsules normally have smooth surfaces and uniform morphology. The optical micrographs and SEM images presented in Figure 2.10C and D show that the MEPCMs created were almost uniform in size, with an average diameter of 460 mm [81]. The shell of the MEPCMs was transparent and had a smooth surface, with n-hexadecyl bromide liquid enclosed within. Although the transparency of the MEPCMs varied slightly due to uneven wall thickness, the maximum variation was only around 10 mm, as observed from the SEM images in Figure 2.10B. Additionally, the PVB microfibers, both with and without RT27, had uniform and smooth morphologies, as shown in Figure 2.10E and F. The coaxial microdevice used for fabrication allowed for the continuous production of microfibers that could reach several meters in length.

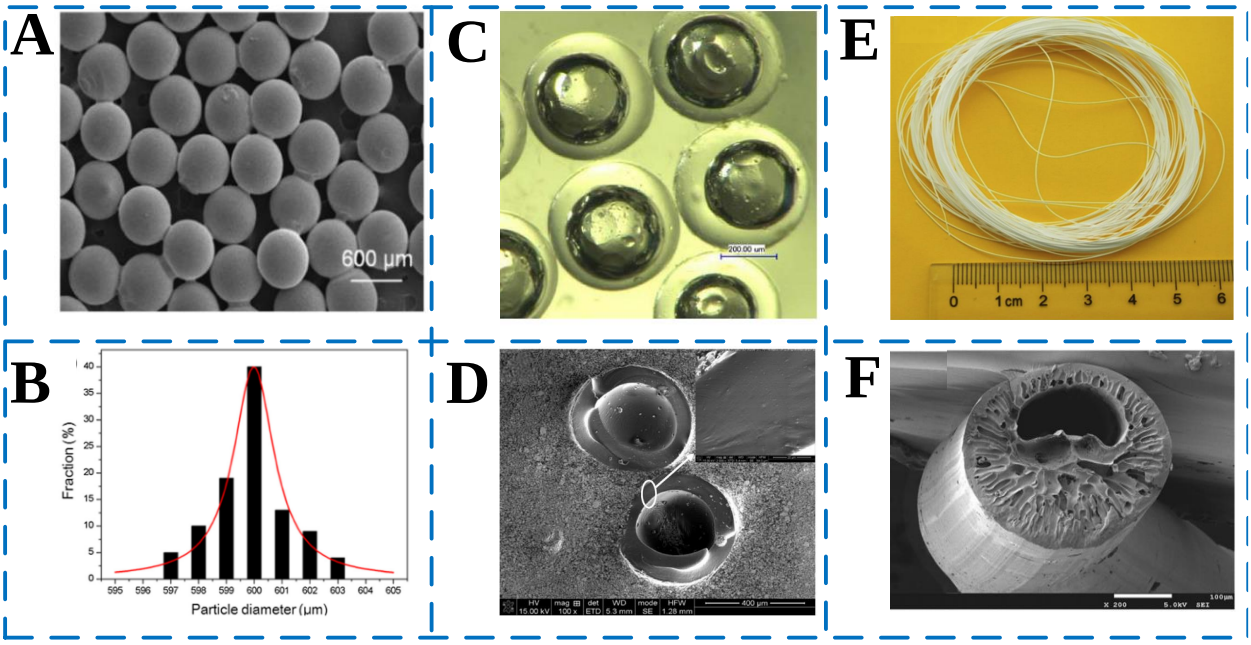

Figure 2-10 A: SEM of MEPCMs; B: particle size distribution of MEPCMs [52]; C: Optical microscope of MEPCMs; D: cross-sectional SEM image of MEPCMs [81]; SEM images of

microfibers after the removal of paraffin RT27 fabricated at Q_i of E: 8 mL/min, F: 16 mL/min. The middle (Q_m) and outer flow rate are, respectively, fixed at 100 mL/min1 and 250 mL/min [51].

2.3.3. Thermal conductivity

The thermal conductivity of MEPCM microcapsules is crucial for thermal energy storage and temperature control. A low thermal conductivity can cause a delay in the thermal response of storage and release of latent heat. Various researchers have studied the calculation method of thermal conductivity of MEPCM microcapsules. When MEPCM microcapsules are in the form of powder particles, the thermal conductivity of a single MEPCM particle can be calculated using the composite ball method [106], expressed by k_p:

$$\frac{1}{k_p d_p} = \frac{1}{k_c d_c} + \frac{d_p - d_c}{k_s d_p d_c} \tag{2.9}$$

$$\left(\frac{d_p}{d_c}\right)^3 = 1 + \frac{\rho_c\left(1 - \alpha_{m,c}\right)}{\rho_s \alpha_{m,c}} \tag{2.10}$$

where k_p, k_c and k_s are, respectively, the thermal conductivity of MEPCM particles, core material and shell material; d_p and d_c are, respectively, the diameter of MEPCM microcapsules and core material; ρ_c and ρ_s are, respectively, the density of core material and shell material; $\alpha_{m,c}$ is the mass fraction of core material.

When MEPCM particles are dispersed in the heat exchange fluid to form MEPCM suspension (i.e., functional thermal fluid), the average thermal conductivity of MEPCM microcapsules suspension

can be calculated using Maxwell's formula [91], which can be expressed by k_b:

$$\frac{k_b}{k_f} = \frac{2 + \frac{k_p}{k_f} + 2c_v\left(\frac{k_p}{k_f} - 1\right)}{2 + \frac{k_p}{k_f} - 2c_v\left(\frac{k_p}{k_f} - 1\right)} \tag{2.11}$$

where k_b and k_f are, respectively, the thermal conductivity of MEPCM microcapsules suspension and carrier fluid; c_v is the volume fraction of MEPCM microcapsules particles in MEPCM microcapsules suspension.

The low thermal conductivity of traditional polymer shell materials has limited the conduction of heat energy in the MEPCM system, resulting in low thermal efficiency during heat absorption or release. This has made it difficult to store and release heat quickly and effectively, which greatly restricts the application of phase change microcapsules. To address this issue, researchers have tried various methods. One approach is to enhance the core and shell materials of MEPCM microcapsules. Nanomaterials such as carbon nanotubes, graphene [84, 107], nano-alumina [108], nano-silicon nitride, and nano-copper [109] can be added to the shell material to improve its thermal conductivity.

2.3.4. Phase change heat storage

The phase change thermal storage performance is crucial in the practical application of MEPCM microcapsules. It is determined by two primary parameters, namely the phase change temperature and the phase change latent heat. These parameters can be measured using a differential scanning

calorimeter (DSC), which helps in evaluating the efficiency of the MEPCM system in storing and releasing thermal energy during phase transitions. Generally speaking, there are endothermic and exothermic peaks on the DSC temperature rise and fall curves of MEPCM microcapsules and phase-change core materials, while the shell materials have no endothermic and exothermic peaks. The heat absorption and release curves of phase change core materials and microcapsules are basically unchanged in the phase change range, but the peak points of phase change appear at different positions. This is because the shell material has a certain barrier effect on the heat transfer of the core material, leading to the hysteresis of the phase change point of the core material. In addition, the average phase change latent heat of microcapsules is typically lower than the average phase change latent heat of the core material. This is because the core material is encapsulated by a shell material, which affects the heat transfer of the microcapsules and reduces the phase change latent heat. In other words, the shell material acts as a barrier that slows down the heat transfer process, resulting in a decrease in the amount of thermal energy that can be stored or released during the phase change.

As mentioned earlier, scholars have attempted to add nanoparticles to microcapsules to improve thermal storage performance of MEPCM microcapsules. For example, Hao et al. [84] conducted experiments on MEPCM microcapsules with varying mass ratios of multilayer graphene, subjecting them to at least two repeated phase-change processes. The results, shown in Figure 17A and B, indicate that there is a slight decrease in the proportion of PCM in the microcapsules as the mass ratio of multilayer graphene increases from 0 to 2 wt%. However, the loss of phase-change enthalpy is minimal, at less than 5%, which means that the reduction in energy storage capacity is negligible. In other words, the addition of multilayer graphene does not significantly affect the

energy storage performance of the MEPCM microcapsules. Besides, Zhang et al. [51] studied the impact of Al_2O_3 content on the thermal energy storage and release properties of composite phase change microfibers. DSC curves were used to analyze the results. The study found that the melting onset temperature and crystallization onset temperature of paraffin RT27 were 26.66 and 24.77 ℃, respectively. When compared to RT27, the melting onset temperature and crystallization onset temperature values of the phase change microfibers with and without Al_2O_3 were almost identical. In other words, the addition of Al_2O_3 did not significantly affect the phase change temperatures of the composite microfibers. Notably, the addition of Al_2O_3 did not have a significant impact on the melting onset temperature and crystallization onset temperature values of the composite phase change microfibers. Additionally, the study found that the melting peak temperature and crystallization peak temperature of RT27 were 29.78 and 22.59 ℃, respectively, and the addition of Al_2O_3 did not cause any noticeable changes in these values. In other words, the presence of Al_2O_3 did not significantly affect the thermal energy storage and release properties of the composite microfibers.

2.3.5. Thermal stability

The thermal stability of MEPCM microcapsules is crucial in determining their service life. If the MEPCM microcapsules have good thermal stability, it means they can maintain their thermal storage performance even after undergoing multiple cycles of heat release. In other words, thermal stability is an important factor in ensuring the longevity of MEPCM microcapsules. Currently, it can be measured by TGA. The thermal stability of MEPCM microcapsules are mainly affected by the microflow control preparation conditions, the type of shell structure, the type of phase change

core material and other factors. Figure 2.11A and B showed that the MEPCM microcapsules prepared by microfluidic device still maintain good thermal storage performance after 100 thermal cycles of heat release.

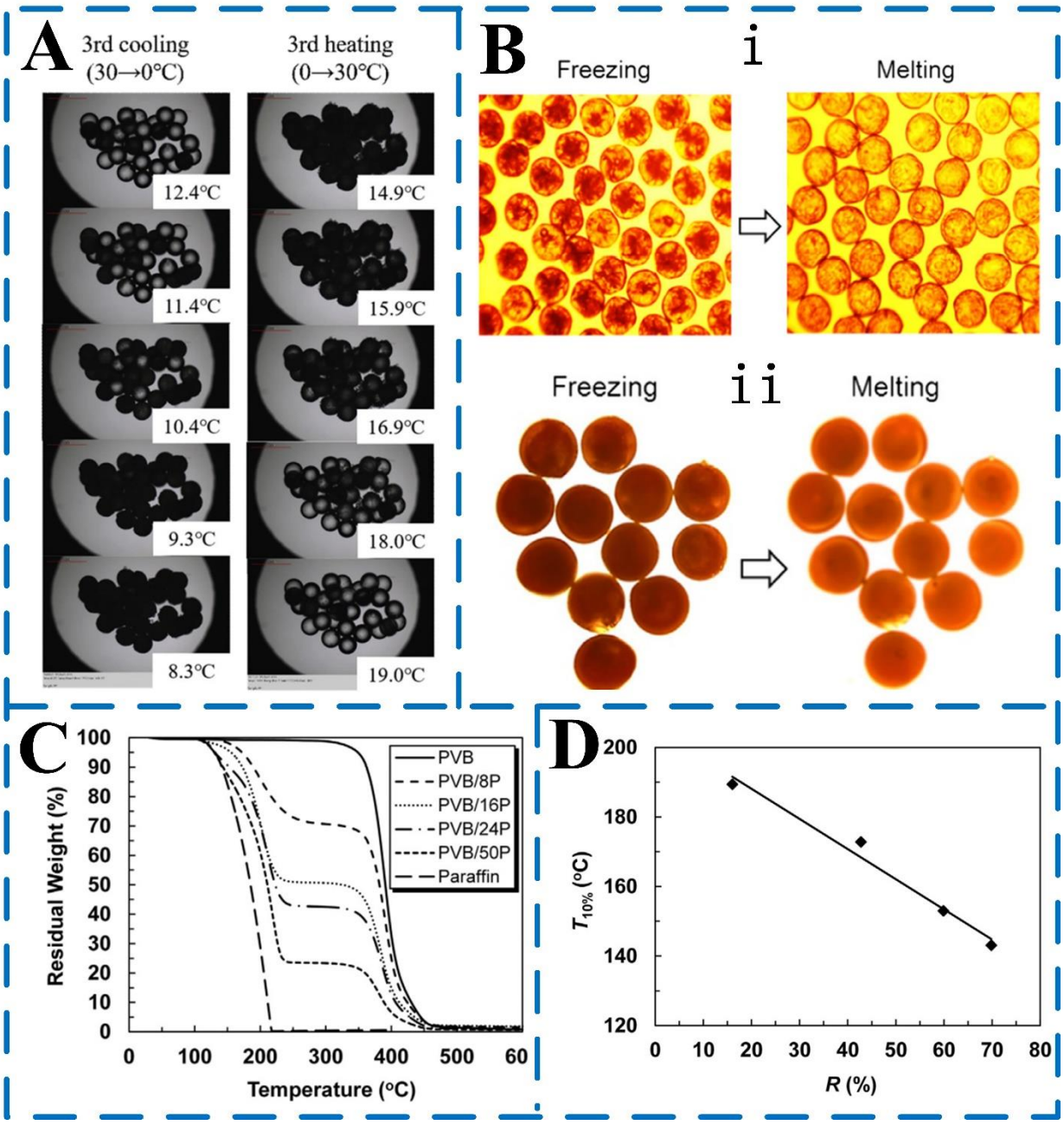

Figure 2-11 A: Optical microscope images showing the MEPCM microcapsules during the three-cycle cooling-heating program.[83]; B: Typical optical microscopy images showing the surface morphologies of MEPCM microcapsules with the shell thicknesses of (i) 30 μm, and (ii) 75 μm after 100th thermal cycling, respectively [52]**;** C: TGA curves for MEPCM fibers and paraffin RT27. D: Effect of RT27 content on T10% which is the weight of a material decreases by 10% of its original weight [51].

Figure 2.11C and D shows the TGA curves of paraffin RT27, PVB fibers, and MEPCM fibers [94]. Both paraffin RT27 and PVB fibers have only one decomposition stage, with paraffin RT27 completely decomposing at 220 ℃ and PVB fibers beginning to decompose at 300 ℃. The phase change fibers undergo two decompositions at temperatures below 300 ℃ and above 300 ℃, respectively. That is, the core layer RT27 decomposes at temperatures below 300 ℃, and the sheath layer PVB decomposes at temperatures above 300 ℃. The temperature corresponding to a 10% reduction in fiber mass (T10%) is taken as a thermal stability parameter. The T10% of two types of microfibers, RT27 and PVB, were measured and found to be 136.7 ℃ and 370.0 ℃, respectively. As the ratio of the core to the sheath (R) increased, the T10% value of the phase change microfibers decreased linearly, approaching that of RT27. Additionally, the T10% of PVB/50P microfibers was 143.1 ℃, which was 6.4 ℃ higher than that of RT27. These results suggest that using core-sheath type fibers to encapsulate paraffin RT27 can improve the thermal stability of PCMs.

2.4. The formation and breakup of LMPA PCM droplet in microfluidic channel

Because the enthalpy porosity method converges rapidly and can produce precise results for the morphology and position of the phase change front at different times with lower computational cost [110]. Therefore, a coupled VOF and enthalpy-porosity method will be used to predict the formation and solidification properties of LMPA droplets in a flow-focusing device. The effects of flow velocity, interfacial tension, continuous phase temperature and wall temperature on LMPA droplet formation and solidification process will be examined in detail.

Besides, the LMPA droplet breakup by the microfluidics normally uses a geometrically mediated passive breakup approach and heavily relies on the sophisticated design of microdevices, hence it is still expensive and technically complex in the manufacture of the microfluidic devices, making the microfluidic technology less accessible to large scale formation of LMPA microparticles. To the best of our knowledge, there has been insufficient study for LMPA microparticle formation dynamics in a straight microchannel multiphase system. The formation of LMPA particles with size less than 10 microns has rarely been reported. It remains unclear and not well understood about the key effects which are dominant in the ultra-small LMPA microparticle formation process. Hence, a novel method for rapid LMPA droplet breakup and ultra-small LMPA microparticle formation will be presented, which can be achieved in a facile approach using a straight microchannel where the droplet is subject to the oscillatory flow. A robust mathematical model has been developed, and validated by numerical simulations to elucidate the droplet breakup mechanisms. The effects of perturbation Weber number and frequencies as well as the cooling wall temperature on the fission and the solidification of LMPA droplets have been investigated.

2.5. Microchannel heat sink improvement based on novel design and graphene enhanced MEPCM

Integrated circuit, invented by Jack Kilby and Robert Norton Noyce in 1958, has changed the world, thanks to its low cost and excellent performance. It has developed rapidly and applied in various everyday electronic devices such as computers, mobile phones, and microwaves. Due to advanced semiconductor manufacturing technology, these chips year on year have become smaller allowing for more and more electronic components to be integrated [111]. One of the founders of Intel corporation, G. E. Moore [112] predicted that every 18 months, the number of electronic components on a chip and chip overall performance will double. However, with the increasing density of electronic components in these advanced chips, significant heat is generated leading to faults and performance decline. For this reason, their effective thermal management has become imperative and hence a hot research topic in recent years. According to Paik et al. [113], depending on whether input power was required, cooling methods can be divided into passive and active methods. Both cooling techniques have been applied in the thermal management of integrated circuits with varying outcomes and performances. Although passive cooling is inexpensive, its performance is comparatively worse than active cooling which also has a downside of requiring external power [113]. Among different academic cooling systems, five cooling approaches used commercially include fan-based cooling, macro-fluidics-based cooling, microelectromechanical systems-based cooling [113], refrigeration-based cooling and microfluidic-based cooling technique [114]. Microfluidic-based cooling techniques utilize small volumes of liquid coolant pushed across the integrated circuits to dissipate heat [113]. Unfortunately, few researchers

focused on this novel technique before since the limitation of manufacturing technique. With the rapid development of fabrication of miniature devices and increasing amount of heat produced by chip, microfluidic cooling method regain public attention. Microchannel heat sink (MCHS), a microfluidic cooling device, typically has several channels whose hydraulic diameter is in micron scale. These microchannels make the device have high specific surface area of coolant and low thermal resistance, which can considerably increase heat transfer performance and efficiency [115-121]. Therefore, microchannel heat sink has become hot topic of cooling technique recently. According to Tao et al. [122], there are three mechanisms of enhancing convective heat transfer: (1) Reducing the thermal boundary layers; (2) increasing the interruption in the working fluid; (3) increasing the velocity gradient near a heat transfer wall. Based on these three mechanisms, the research direction of MCHS mainly focused on the geometric structure of MCHS and various coolant which had higher heat transfer capacity. The geometric structure of MCHS primarily influences hydraulic and heat transfer performance [123-128]. For instances, several studies have shown that varying the shape and cross-section of microchannels [129-131], employing secondary flow in MCHS [132-134], using wavy microchannels [135-138], and using pin-fin structures [139-143] all influence heat and flow characteristics. Gunnasegaran et al. [130] conducted a numerical analysis to examine how different geometrical parameters affect the flow of water and heat transfer characteristics in microchannels. The investigation focused on Reynolds numbers ranging from 100 to 1000. The researchers found that microchannels with smaller hydraulic diameters, particularly those with rectangular shapes, exhibited improved uniformity in both heat transfer coefficient and temperature. Kuppusamy et al. [132] utilized a technique involving the introduction of slanted passages in the walls of MCHS. These passages were placed between adjacent channels,

alternating their orientation. The researchers discovered that this approach induced secondary flow, which resulted in a reduction in the average thickness of the thermal boundary layer. As a result, the heat transfer performance of the MCHS was enhanced, and there was only a slight increase in pressure drop. This improvement was attributed to the combined effect of the re-development of the thermal boundary layer and the mixing of the flow within the heat sink. In contrast, the study conducted by Lin et al. [138] focused on the numerical investigation of a wavy microchannel heat sink with varying wavelength and/or amplitude along the direction of flow. Their findings revealed that the performance of the heat sink improved noticeably as the thermal resistance decreased and the maximum temperature difference on the bottom wall decreased. This improvement was observed when the wavelength of the wavy units decreased or the amplitude increased. Several other articles also investigated varying configurations of MCHS. For instance, Chein and Chen [144] studied various inlet/outlet arrangements of MCHS and proved that when the coolant flows in and out vertically, better heat sink performance is achieved. Hajmohammadi, et al. [145] conducted the effect of slip condition on thermal performance of MCHS and found that slip boundary condition had smaller thermal resistance compared with no slip boundary condition. Xu et al. [146] studied hydraulic and thermal characteristics of rectangular cross section microchannels with dimples. They independently studied several parameters of dimpled MCHS, such as aspect ratio of rectangular cross section, spacing and depth of dimples. Compared with plain channels, dimpled channels reduced 3.2 K of temperature and 2% of pressure drop, also they achieved a 15% increase in the Nusselt number value. Zhang et al. [147] developed a model to examine the impact of roughness elements on laminar flow and heat transfer in a microchannel. They aimed to compare the thermal and hydrodynamic characteristics of rough and smooth

channels. It was revealed that the presence of roughness elements in the microchannel resulted in improved global heat transfer performance. However, this improvement came at the expense of increased pressure drop compared to a smooth channel. Adewumi et al. [148] studied numerical simulations to evaluate the flow and heat transfer performances in a microchannel heat sink with micro pin fin inserts. Their aim was to optimize the design of the integrated microchannel and micro pin fins to minimize the peak temperature in the configuration. Their findings showed that increasing the Bejan number led to a decrease in the minimum peak temperature. Furthermore, it is also noticed a notable enhancement in the maximum thermal conductance when the microchannel heat sink incorporated three to six rows of micro pin fin inserts in its structure.

For coolant optimization, many researchers focused on nanofluid as coolant [149-154]. Sarafraz et al [155] carried out an experimental investigation in a rectangular microchannel using silver nanoparticles/deionized water as a cooling fluid in a copper-based heat sink. They found that the heat transfer coefficient of the microchannel experienced enhancement when the traditional coolant, deionized water, was replaced with a nanofluid. However, they also observed a slight increase in fouling thermal resistance, friction factor and pressure drop parameter when the nanofluid was utilized in the system. Ali and Arshad [156] investigated water based graphene nanoplatelets (GNPs) nanofluids, and examined the angle effect of MCHS on heat transfer coefficient and thermal resistance using the nanofluid as coolant. Their result showed that MCHS with 22.5-degree channel angle achieved the lowest thermal resistance and the best thermal performance. Ijam et al. [157, 158] conducted a study on the effectiveness of using nanofluids in a microchannel heat sink for cooling purposes. They compared the cooling performance of different nanofluids, including Al_2O_3/water, TiO_2/water, and SiC/water. Their findings indicated

that the Al_2O_3/water nanofluid outperformed the other options in terms of cooling efficiency. Seyf et al. [159] developed a three-dimensional model of a microtube heat sink. They used a coolant called nanoencapsulated phase change materials (NEPCM) slurry, which consisted of octadecane as the NEPCM and polyalphaolefin as the base fluid. It was discovered that incorporating NEPCM into the base fluid led to a significant enhancement in heat transfer. Chen et al. [160] conducted an experiment to investigate the flow and heat transfer characteristics of micro-encapsulated phase change material (MEPCM) in both wavy and straight microchannels. The study found that as more MEPCM was added to the fluid, the pressure drop increased. In the phase change region, the MEPCM exhibited better heat transfer performance compared to water, attributable to the latent heat absorbed during the melting of MEPCM. However, the low thermal conductivity of MEPCM limits its effectiveness in charging and discharging latent heat for various applications. Meanwhile graphene possesses outstanding mechanical properties, a large surface area, distinctive physicochemical characteristics, and low density [161, 162]. Functionalized graphene nanocomposites, such as graphene oxide (GO), exhibit enhanced surface area and porosity, effectively mitigating graphene layer agglomeration [163]. Hu et al. [164] developed MEPCM using a combination of polyvinyl alcohol and high thermal conductivity graphene oxide (GO) as cosurfactants through an emulsion polymerization process. It was observed that the thermal conductivity of the MEPCM samples significantly increased from 0.32 W/m•K to 1.04 W/m•K with the addition of 0.5 wt.% GO. This enhancement suggests the potential for further improving the overall performance of microchannel heat sinks by using a GO/MEPCM slurry as the coolant, a novel approach that has not been explored previously. Thus, building upon the concept of a straight microchannel heat sink, a new micro-pin fin design with three different arrangements and

five different kinds of shapes within the microchannel was proposed. In this chapter, the impacts of heat sink material, arrangement, shape, and spacing distance of micro-pin fins on the thermal performance of MCHS were investigated. Parameters like Nusselt number, the total thermal resistance, pressure drop, the dimensionless temperature at the exit and the overall performance evaluation criterion (PEC) will be estimated for the optimization study. By conducting a comparative analysis, the most effective configuration was identified. Based on this, considering the earlier discussion of the beneficial effects of nanofluids and MEPCM slurry on enhancing the performance of MCHS, nanofluids with different Al2O3 volume fractions and GO/MEPCM slurry with different GO content were employed to further enhance the thermal performance of the MCHS after optimizing the micro-pin fin configuration.

2.6. Aim and Objectives

The aims of the current project are to develop high quality graphene enhanced MEPCMs, which will be further used to optimize the performance of microchannel heat sink with a reasonable operation conditions. Specifically, by numerically researching on the mechanisms of PCM droplet production and breakup progress, the experiments can be built up for optimizing the thermal performance of MEPCMs based on microfluidic device. Also, the adopting CFD approaches which can dynamically model the heat transfer process of MEPCM and microchannel heat sink, and a simulation database which contains the physical and thermal properties of MEPCMs and devices can be generated by the gained knowledge.

The main research objectives are:

- To review the literature on the research of MEPCM and its application on microchannel heat sink.

- To numerically examine the formation and breakup of PCM droplet in microchannel.
- To experimentally fabricate the graphene enhanced MEPCM with a small relative size change using economically feasible technique and materials.
- To evaluate the heat storage and mechanical performance of graphene enhanced MEPCM experimentally.
- To evaluate the thermal performance of graphene enhanced MEPCM/microchannel heat sink system numerically, considering multiple factors such as the heat sink material, arrangement, shape, and spacing distance of micro-pin fins and graphene enhanced MEPCM content in the coolant.

Chapter 3- Methodology

Compared with these conventional fluids, liquid LMPA as a PCM has obviously higher interfacial tension and density, so it is necessary to study how different factors influence the formation of LMPA droplets. Some scholars have experimentally demonstrated the feasibility of generating LMPA droplets by using microfluidic device [196-198]. However, these literatures only focused on the formation of liquid droplets, without paying attention to the solidification behavior of droplets in microfluidic devices. In order to account for the phase change, some numerical models based on the phase-field (PF) method [199-201], cellular automaton (CA) approach [202] or enthalpy-porosity method [203-205] have been explored and applied to simulate the solidification of LMPA fluid. Because the enthalpy porosity method converges rapidly and can produce precise results for the morphology and position of the phase change front at different times with lower computational cost [44]. Therefore, in this chapter, a coupled VOF and enthalpy-porosity method will be used to predict the formation, breakup and solidification properties of PCM droplets in a microchannel. The effects of key factors such as flow velocity, interfacial tension, continuous phase temperature and wall temperature on PCM droplet formation and solidification process will be numerically examined in detail. Base on the numerical results, a practical and simple needle based microfluidic device is proposed, combined with UV curing technology, to prepare microcapsules. By changing the flow rate, uniformly sized double emulsion droplets can be produced is observed. In addition, the microcapsules were characterized by optical microscopy, DSC, SEM, and UV spectrophotometer. Finally, the numerical study will be used to examine some key factors such as heat sink material, arrangement, shape, and graphene/MEPCM particle with different volume fractions on the performance of microchannel heat sink.

3.1. The formation and solidification of PCM droplet in microfluidic channel

3.1.1. Governing equations and boundary conditions

For the numerical analysis of the droplet generation and solidification process, the following assumptions were made: (1) the two-phase fluid was Newtonian and incompressible; (2) the flow in the microchannel was unsteady and laminar, with ignoring viscous dissipation; (3) The thermal properties of the liquid and solid phases were assumed to be constants; (4) The 3D convection was not taken into account as a 2D model was used in this chapter.

The numerical method in this chapter is based on the VOF and enthalpy-porosity method of the commercial code FLUENT. The governing equations for the mass conservation and momentum conservation are given as follows:

$$\frac{\partial \rho}{\partial t} + \nabla \cdot \left(\rho \vec{V}\right) = 0 \tag{3.1}$$

$$\frac{\partial \left(\rho \vec{V}\right)}{\partial t} + \nabla\left(\rho \vec{V} \cdot \vec{V}\right) = -\nabla P + \nabla \cdot \left[\mu\left(\nabla \vec{V} + \nabla \vec{V}^{T}\right)\right] + \vec{F} + \vec{S} \tag{3.2}$$

where ρ is density, $\vec{V}$ is fluid flow velocity, t , P and μ are, respectively, the time, pressure and dynamic viscosity. $\vec{F}$ is a source term and equal to interfacial tension force in this chapter since gravity acceleration term can be ignored in this micrometer scale and $\vec{F} = \vec{F}_{\sigma}$, $\vec{S}$ is the momentum source term, suitable for the phase change process when convection is considered.

The interface tracking between the phases was achieved by solving the following volume fraction continuity equation:

$$\frac{\partial \alpha}{\partial t} + \nabla \cdot \left(\alpha \vec{V}\right) = 0 \tag{3.3}$$

For the single emulsion, the density and dynamic viscosity in equation Equation (2) can be calculated as follows:

$$\rho = \alpha_C \rho_C + (1 - \alpha_C)\rho_D \tag{3.4}$$

$$\mu = \alpha_C \mu_C + (1 - \alpha_C)\mu_D \tag{3.5}$$

where α is the proportion of fluid phase in every grid, subscript C and D represent continuous phase and discrete phase respectively.

For the double emulsion formation, the properties appearing in the transport equations which are determined by the volume-fraction-averaged density and viscosity in each control volume are given by Equation (3.6), and Equation (3.7), respectively

$$\rho = \alpha_o \rho_o + \alpha_m \rho_m + \alpha_i \rho_i \tag{3.6}$$

$$\mu = \alpha_o \mu_o + \alpha_m \mu_m + \alpha_i \mu_i \tag{3.7}$$

Continuum surface force (CSF) method was applied to achieve the interfacial surface force term in Equation (3.8), where

$$\vec{F}_\sigma = \sigma \kappa \nabla \alpha \tag{3.8}$$

where σ is the surface tension coefficient and κ is the local curvature which is given by

$$\kappa = \nabla \cdot \hat{n} \tag{3.9}$$

where $\hat{n}$ is the surface unit norm defined as

$$\hat{\mathrm{n}} = \frac{\nabla\alpha}{|\nabla\alpha|} \tag{3.10}$$

By defining the contact angle at the channel wall θ to consider wall adhesion and calculate the surface normal at the reference cell close to the channel wall by the following formula

$$\hat{\mathrm{n}} = \hat{n}_w cos\theta + \hat{t}_w sin\theta \tag{3.11}$$

where $\hat{t}_w$ and $\hat{n}_w$ are the unit vectors tangential and normal to the wall, respectively.

Energy equation can be written as Equation (3.12):

$$\frac{\partial}{\partial t}(\rho H) + \nabla \cdot \left(\rho \vec{V} H\right) = \nabla(k\nabla T) \tag{3.12}$$

where T is temperature, k is the thermal conductivity, and H is the specific enthalpy. The specific enthalpy can be received by the sum of the enthalpy change caused by the phase change γL and the sensible enthalpy, $H = H_{ref} + \int_{T_{ref}}^{T} C_P dT$, where H_{ref} is the reference enthalpy, T_{ref}, C_P is the specific heat, L is the specific melting enthalpy, and γ is the liquid fraction during the phase transition which happens in $T_S < T < T_L$ region, defined by Equation (3.13)

$$\gamma = \begin{cases} = 0, & T < T_S \\ = \frac{T - T_S}{T_L - T_S}, & T_S < T < T_L \\ = 1, & T > T_L \end{cases} \tag{3.13}$$

where T_S and T_L are the liquidus temperature and solidus temperature of the dispersed phase, respectively, which are 285.85 and 288.85, respectively.

The source term $\vec{S}$ in the momentum equation is defined as:

$$\vec{S} = A(1-\gamma)^2 \frac{\vec{V}}{\gamma^3 + \varepsilon} \tag{3.14}$$

where A is a constant, which is used to describe how sharply the velocity is suppressed during phase material solidification, and it can be normally changed from 10^4 to 10^7 (10^6 is used in present chapter). ε is a small value (0.001) to prevent divergence.

The boundary conditions are as follows:

Inlet:

$$\mathrm{V_C} = Constant \tag{3.15}$$

$$\mathrm{V_D} = 0.01\ m/s \tag{3.16}$$

$$\mathrm{T_C} = Constant \tag{3.17}$$

$$\mathrm{T_D} = 290\ K \tag{3.18}$$

Outlet:

$$\mathrm{P} = \mathrm{P}_{atm} \tag{3.19}$$

Wall:

$$\mathrm{T_W} = \mathrm{Constant} \tag{3.20}$$

where V_C and V_D are respectively the velocity of continuous phase and dispersed phase; T_C and T_D are the temperature of continuous phase and dispersed phase respectively; P_{atm} is the atmospheric pressure and T_W is the cooling wall temperature.

It is a complex and time-consuming to conduct a 3D simulation for the process of droplet generation. Although the 2D model is vulnerable to some errors, but its computational cost is lower than that of the 3D model and the 2D plot of the dispersed phase versus continuous versus contours in the literature [47], which indicated that the depth curvature can be negligible and it is sufficient for the 2D assumption to eliminate the general features of the system. The 2D numerical method

used in this chapter is validated in section 4 by comparing with the experimental results of the LMPA droplet formation in a 3D microchannel junction proposed by Hutter et al. [35].

The equations are solved in the Ansys Fluent 2021R1 software. A two-dimensional model is established. The PRESTO! scheme is employed to compute the pressure equation. The pressure-velocity coupling term is discretized using PISO scheme and the second-order upwind scheme is adopted for the momentum equation and the interpolation of the interface geometry is solved by Geo Reconstruct method.

3.1.2. Simulation setups

A schematic view for a cross flow-focusing device case model used for simulation in present study is shown in Figure 3.1(a). Material properties and the initial values used in the simulation were given in Table 3.1. The liquid LMPA which has been heated to 290 K was used as the dispersed phase and silicon oil was used as the continuous phase. The LMPA liquid phase entered from inlet 1, and the silicon oil phase entered from inlets 2 and 3. In this research, rectangular mesh were used as shown in Figure 3.1(b).

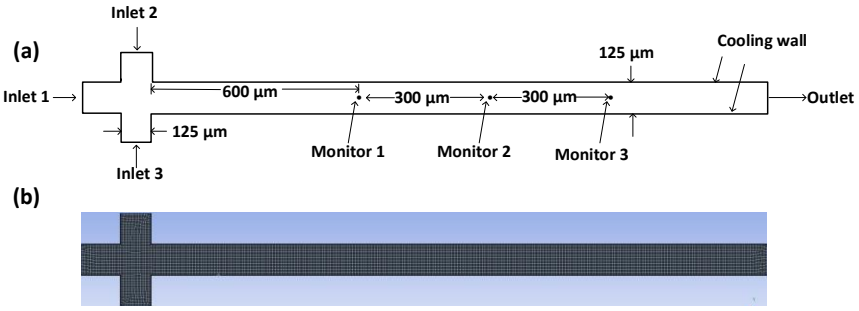

Figure 3-1 (a) A schematic view for the microfluidic case model used for simulation; (b) Geometry of cross flow-focusing device with mesh.

Table 3-1 Material properties and initial parameters of oil-LMPA system.

Material	Density (Kg/m^3)	Liquid dynamic viscosity (Pa · s)	Specific heat (J/kg K^{-1})	Thermal conductivity (W/m K^{-1})	Liquidus temperature (K)	Solidus temperature (K)	Latent heat of fusion (J/kg)	Molecular weight (J/kg mol^{-1})	Reference temperature (K)
Continuous phase	960	0.0451[35]	1630	0.16	218.15	218.15	220000	90	298.15
Dispersed phase	6250	0.00199 [35]	197	18	288.85	285.85	36800	190	298.15

The dependency on cell size and time steps was examined by using four mesh elements (4802, 12046, 23498 and 42418) and three time steps (0.0001s, 0.00001s and 0.000001s), and the droplet generation frequency are almost the same with 23498 and 42418 mesh elements or with 0.00001s and 0.000001s time steps as shown in Table 3.2 and Table 3.3. Therefore, a step size of 0.00001 s and the model with 23498 cells were used for the balance of precision and computational cost.

Table 3-2 Droplet generation frequency at different mesh elements.

Mesh elements	4254	12046	23498	42418
Frequency (Hz)	98.03	94.27	89.29	90.10

Table 3-3 Droplet generation frequency at different time-steps.

Time step	0.0001	0.00001	0.000001
Frequency (Hz)	107.52	89.29	89.01

The coaxial microcapillary fluidic device to generate double emulsion droplet is shown in Figure 3.2. A simplified two-dimensional domain for computation is illustrated in Figure 3.2(a), a rectangular mesh were used as shown in Figure 3.2(b).

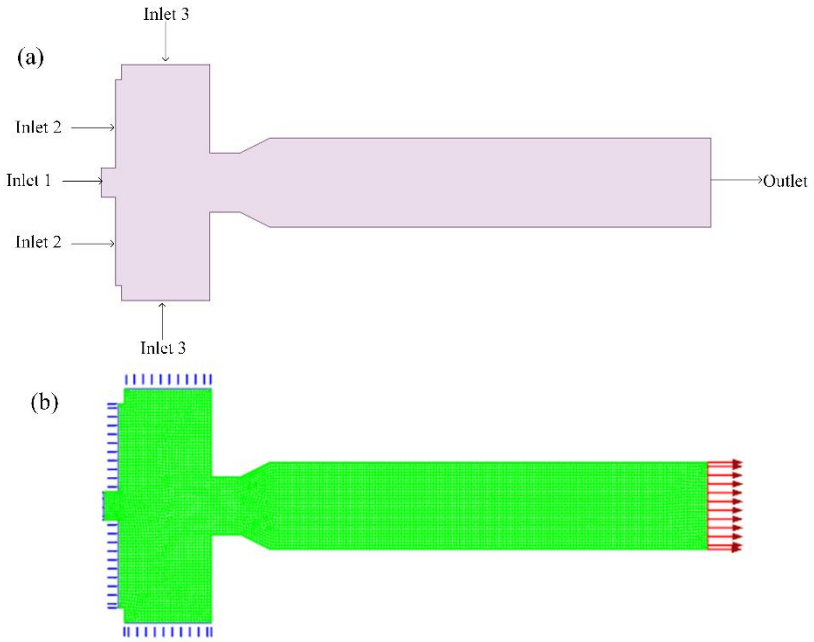

Figure 3-2 Schematic of double emulsion formation in a coaxial flow-focusing microfluidic device: (a) simplified computational domain; (b) Geometry of cross flow-focusing device with mesh.

The Global Courant Number is defined as a dimensionless number which is the ratio of the time step to the characteristic time of transit of a fluid element across a control volume, and in this part, it is no more than 0.35 to ensure a better balance of convergence and computational cost.

3.1.3. Model validation

As there is no suitable reported experimental results for simultaneously realizing the formation and solidification process of LMPA droplet in microfluidic device, so in order to verify our simulation method, this chapter only simulated the formation process of droplets, and compare it with the relevant experimental results.

The coupled VOF and enthalpy-porosity method was used to numerically simulate the formation of LMPA liquid droplets in a flow-focusing microchannel, and verified by the experimental results of microfluidic device [165]. Figure 3.3(a) is the design of the microfluidic device with 80 μm nozzle geometry, the depth of the channel was 75 μm, and Figure 3.3(b) shows the geometric structure for simulation. The droplets were made of EGaIn (75.5% Ga and 24.5% In by weight) liquid metal solution and the continuous phase was silicone oil. As the working fluids and geometry of this experimental study were very similar to our designed microchannel, these experimental results were selected for verification in present chapter. In the simulation, the initial temperature and the inlet temperature of both phases were kept at 300 K, and the wall was insulated. Therefore, the droplets had no heat transfer in the microfluidic channel. A value of 0.09 N/m for interfacial tension between the LMPA phase and silicone oil phase tested by Hutter et al. [165] was employed in this simulation and other material properties used was given in Table 3.4. In order to achieve the numerical results, the simulations were carried out by considering several flow ratios

(the ratio of the volumetric flow rate of continuous phase Q_C to the volumetric flow rate of dispersed phase Q_d). The frequency was obtained by the quantity of the produced droplets between two similar frames and the time between these two frames.

Table 3-4 Material properties and initial parameters of oil-LMPA system.

Material	Density (Kg/m^3)	Liquid dynamic viscosity (Pa · s)	Specific heat (J/kg K^{-1})	Thermal conductivity (W/m K^{-1})	Liquidus temperature (K)	Solidus temperature (K)	Latent heat of fusion (J/kg)	Molecular weight (J/kg mol^{-1})	Reference temperature (K)
Continuous phase	960	0.0451[35]	1630	0.16	218.15	218.15	220000	90	298.15
Dispersed phase	6250	0.00199 [35]	197	18	288.85	285.85	36800	190	298.15

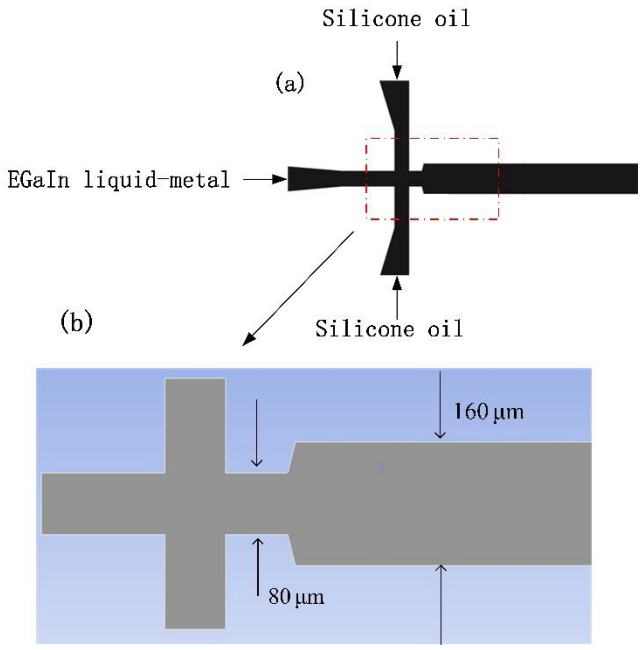

Figure 3-3 Schematic diagram of microfluidic device for verification; (a) Schematic diagram used by Hutter et al. [35] for experimental investigation; (b) Geometric structure of simulated channel in Fluent software.

The optimum contact angle should be ascertained before the simulation. Therefore, in this chapter, different contact angle values of θ, including 0°, 45°, 90°, 135°, 150°, 160° and 180°, were carefully simulated at a given flow rate before performing the verification. For an assigned $\frac{Q_C}{Q_D} = 1$ and the total flow rate $Q = Q_C + Q_D = 2000\ \mu L\ h^{-1}$, when the contact angle is 160°, the droplet generation frequency is 312.5, which is almost the same as the value of 315.97 obtained in the experiment [165] and the simulation results were the most consistent with the experimental results in terms of shape and equivalent diameter, as shown in Figure 3.4. Therefore, the contact angle was assumed to be 160° in all simulations.

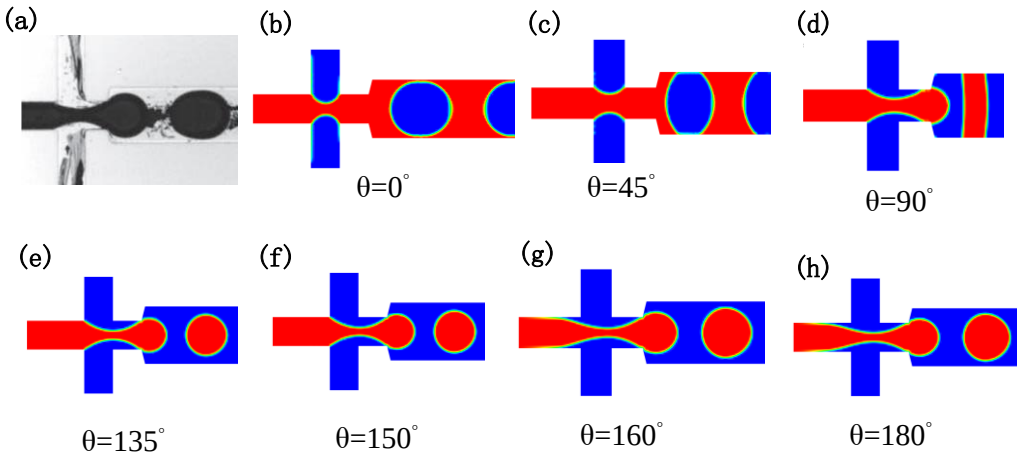

Figure 3-4 Determining the best contact angle of the simulated droplet formation process; (a): Hutter et al's experimental results [35]; (b)-(h): simulating different contact angles of 0°, 45°, 90°, 135°, 150°, 160° and 180° for $\frac{Q_C}{Q_d} = 1$ and the total flow rate $Q = Q_C + Q_d = 2000\ \mu L\ h^{-1}$, the most accurate results were obtained when the contact angle was 160° .

After ascertaining the optimal contact angle value, the simulations were carried out. In Figure 3.5, the droplet generation frequency obtained by numerical simulation was in good agreement with the experimental results. Figure 3.6 showed that the equivalent diameters obtained by simulations were slightly smaller than that achieved by experiment. It is possible that some variations of experimental physical properties (such as small fluctuations of temperature, flow rate, or incomplete straight channel wall) might cause the deviation between observed droplets and simulated sizes. The roughness of the downstream channel might also influences the length of larger droplets.

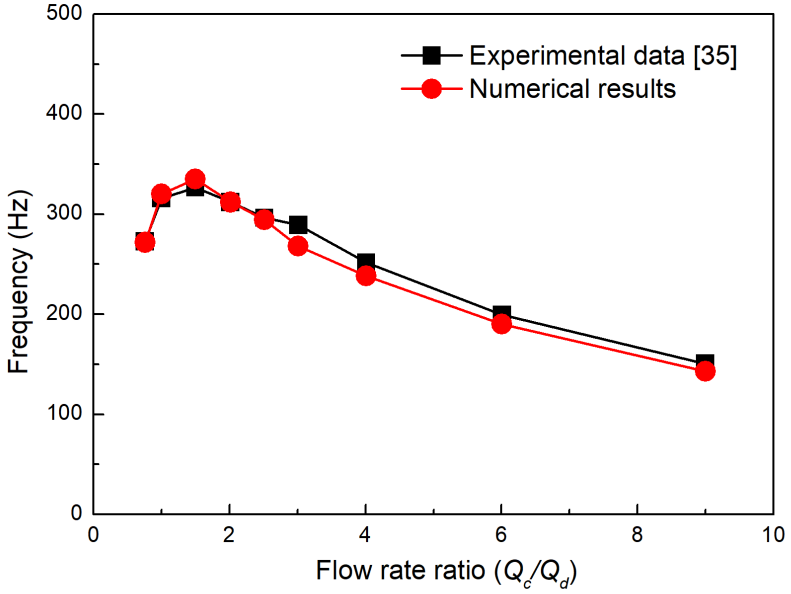

Figure 3-5 Comparison of droplet generation frequency between numerical results and experimental data.

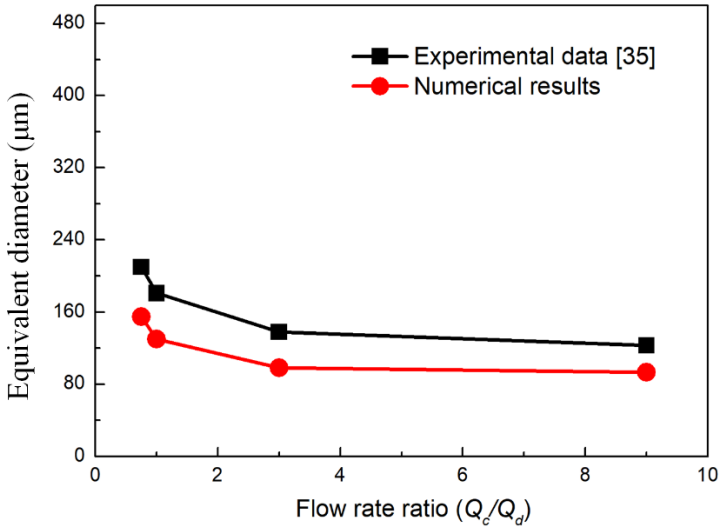

Figure 3-6 Comparison of equivalent diameter between numerical results and experimental data.

In this part, the effect of mesh elements was examined by using the number of 4802, 12046, 22823 and 40441, and the droplet generation frequency were almost the same with 22823 and 40441 mesh elements as shown in Table 3.5. Therefore, an optimal grid resolution containing 22823 elements was used for the balance of precision and computational cost. The effect of time-steps was also checked and it is shown that the frequency droplet generation frequency were with 0.00001 and 0.000001. Thus simulations were carried out using a timestep of 0.00001 s.

Table 3-5 Droplet generation frequency at different mesh elements.

Mesh elements	4802	22823	40441
Frequency (Hz)	306.122	312.5	311.7

3.2. The breakup of LMPA in microfluidic channel

3.2.1. Numerical Model

In this section, the numerical model has been developed to investigate the response of a liquid droplet to various oscillating flow applied at the inlet of a straight microchannel, with the aim to understand the underlying physical mechanisms of droplet breakup phenomenon in a microchannel, as illustrated in Figure 3.7.

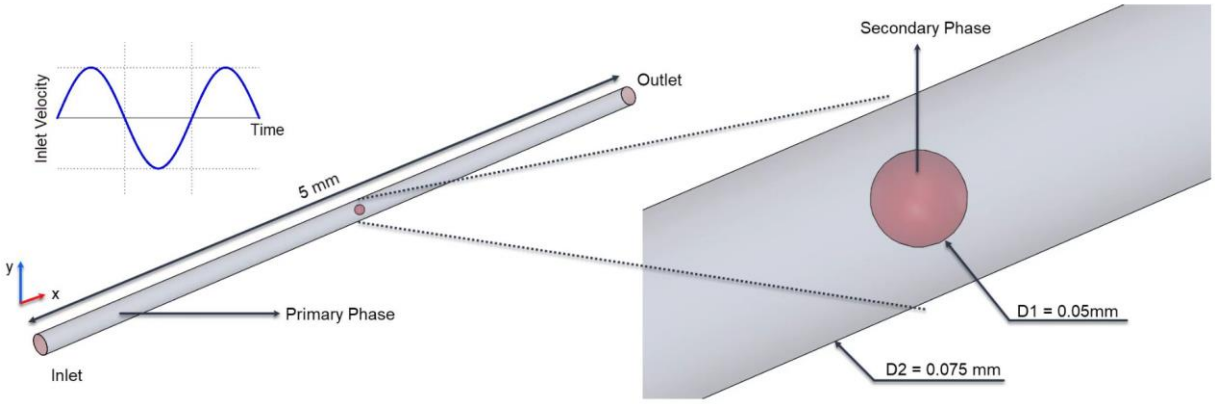

Figure 3-7 An illustrative sketch of the numerical model.

A cylindrical microchannel with the length of 5 mm and the diameter of 0.075 mm was adopted in the present study. A liquid droplet of diameter 0.05 mm was initially positioned at 2 mm downstream from the inlet, suspending in the center of a simple straight microchannel, as shown in Figure 3.3, which can be simulated as 2D system, because of the extremely low ratio of radius versus axial length of the microchannel, i.e., 0.0075, and the low Re flows. The wall of the microchannel was considered rigid. The oscillating flow could be studied by altering the frequency and amplitude of the periodic disturbance of the continuous phase, which was achieved by applying the velocity of an oscillating flow as the inlet boundary condition, and the axial and radial direction components of velocity can be expressed as follows:

$$V_x = A \cdot \cos(2\pi f t) \tag{3.21}$$

$$V_y = 0 \tag{3.22}$$

where V is the velocity, A is the amplitude, t is time, f denotes disturbance frequency, and x- and y- directions are defined as the axial and radial directions, respectively, as shown in Figure 3.7. The outlet was set with zero-gauge pressure.

The LMPA droplet is dispersed in the continuous phase of water, and the formation process of LMPA particles was examined. The solidification process of LMPA microdroplets was realized by applying a temperature T_C lower than the melting point of LMPA at the wall of the microchannel. The material properties of LMPA-in-water system are listed in Table 3.6.

Table 3-6 Material properties of the LMPA–in-water system.

LMPA *(Secondary Phase)*	
Latent heat (J/kg)	36800
Density (mg/m^3)	9160
Viscosity (kg/m s^{-1})	0.0024
Specific heat (J/kg K^{-1})	197
Thermal conductivity (W/m K^{-1})	18
Liquidus temperature(K)	320
Solidus temperature (K)	318
Surface tension (N/m)	0.15799
Initial temperature (K)	321
Water *(Primary Phase)*	
Density [mg/m^3]	995.6
Viscosity [kg/(m s)]	0.0007972
Thermal conductivity (W/m K^{-1})	0.6
Surface tension (N/m)	0.0728
Initial temperature (K)	300

The numerical method in this research is based on the VOF and enthalpy-porosity method of the commercial code FLUENT.

Weber number is defined as:

$$\mathrm{We} = \frac{\rho_C A^2 h}{\sigma} \tag{3.23}$$

where ρ_C is the density of continuous phase, A is the velocity amplitude and h is the width of the microchannel.

The capillary number can be calculated by:

$$\mathrm{Ca} = \frac{\mu_c A}{\sigma} \tag{3.24}$$

where μ_c represents the viscosity of continuous phase.

The liquidus temperature is 318 K, while the solidus temperature is 320 K. as shown in Table 3.6. The temperature at the inlet is 300 K.

Conducting a 3D simulation to model droplet generation is a complex and time-consuming process. However, using a 2D model reduces computational costs, despite its vulnerability to some errors. Previous research (Serra et al., 2007) demonstrates that a 2D plot representing the dispersed phase and continuous phase contours shows that the depth curvature is often negligible. Hence, assuming a 2D system can effectively capture the main behaviors of the droplet generation process. In this research, the 2D numerical method employed is validated in Section 4 by comparing its results to the experimental findings of the LMPA droplet deformation in a 3D microchannel proposed by Olbricht and Kung [166] .

The pressure equation was computed using PRESTO! Interpolation scheme. The convective term was discretized using a second-order upwind scheme, while the diffusion term was discretized using central difference scheme.

The momentum equation adopted the second-order upwind, and the volume fraction was solved by Geo Reconstruct method. The simulation study has been carried out by ANSYS Fluent software. The size of the droplets was analysed by ImageJ, which is used to measure the surface area of particles, and then equate it to a circle to calculate its radius. A mesh sensitivity study was conducted to determine the best mesh elements for this model, and this proposed numerical model is also validated with existing experimental results found in the literature.

3.2.2. Model validation

In order to verify the accuracy of the numerical model, the simulation results of the deformation process of droplets are compared with the reported experimental results by Olbricht and Kung [166], in which the coupled enthalpy-porosity and VOF methods were used to numerically study the deformation of liquid droplets in a microchannel. Figure 3.8 shows that when the viscosity ratio of phases is 0.99, the experimental droplet size is in good agreement with the simulation results under different capillary numbers. Figure 3.9 shows that the ratio of droplet velocity and average fluid velocity obtained by the simulation has small deviation from that obtained by the experiment, which might attribute to some changes in experimental physical properties such as small thermal and flow fluctuations. The roughness of microchannel walls may also affect the velocity of droplets but is ignored in the present chapter.

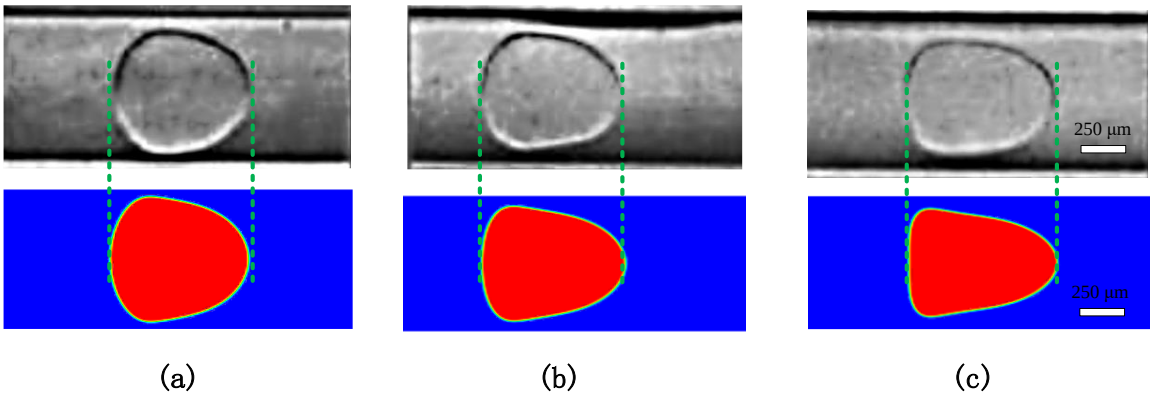

Figure 3-8 Comparison of equilibrium droplet shapes when the viscosity ratio is 0.99 and scale ratio is 0.95. Top panel: Experimental results Olbricht and Kung [166] and Bottom Panel: Present work. Three different Capillary numbers are considered, (a) Ca = 0.05, (b) Ca =0.10, (c) Ca =0.16.

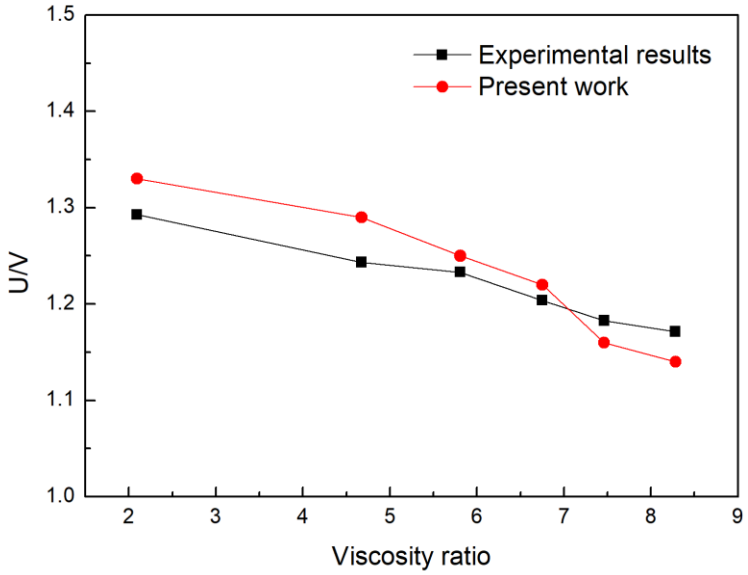

Figure 3-9 Comparison of the velocity of a droplet *U* relative to the average velocity of the flow *V* under different viscosity ratio, with Ca = 0.056. The experimental data is obtained from the work by Olbricht and Kung [166] .

3.3. Microchannel heat sink improvement based on novel design and graphene enhanced MECPM

3.3.1. Model description

Figure 3.10 shows isometric views of four MCHS with an integrated circuit in the middle. One MCHS is without micro pin-fins, the other three have different configurations of micro pin-fins and they are labelled Structure A, B and C. Structure A has thirteen (13) evenly spaced micro pin-fins on the surface of the lower channel wall while Structure B has two rows of evenly spaced micro pin-fins on the surfaces of the upper channel wall (6 fins) and lower channel wall (7 fins). Structure C is a novel concept of MCHS with thirteen (13) micro pin-fins in total. With this structure the upper, left and right channel walls each have three (3) evenly spaced micro pin-fins and within the lower channel wall itself there are four (4) evenly spaced micro pin-fins.

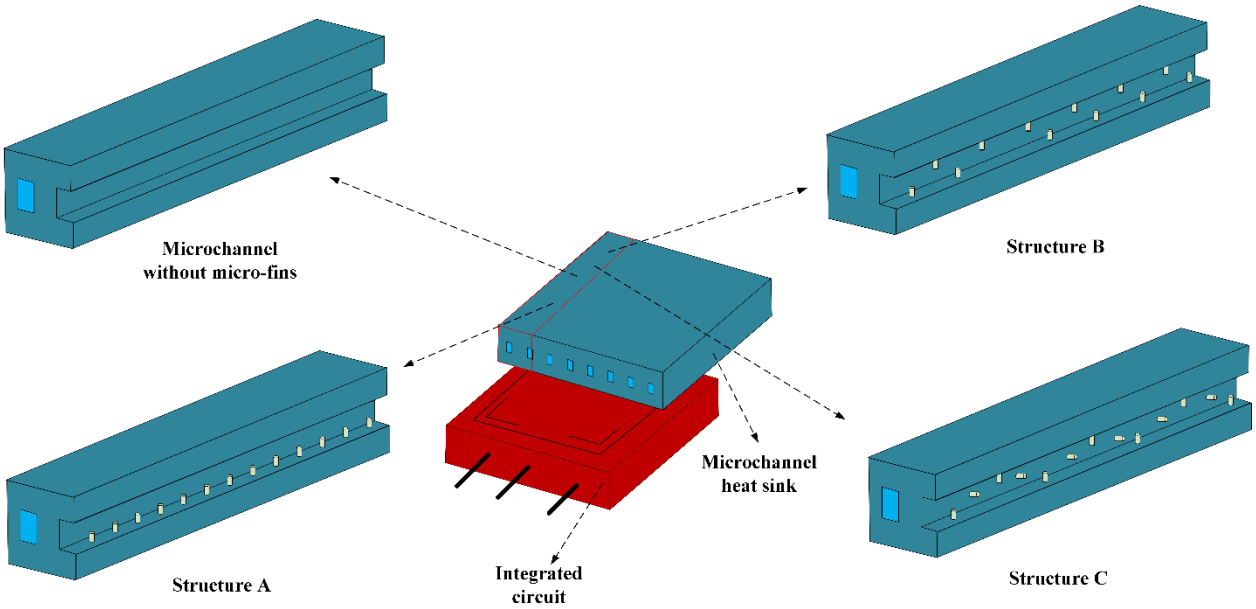

Figure 3-10 Isometric view of MCHS without micro pin-fins and other three arrangements of MCHS with micro pin-fins.

Figure 3.11(a) shows the annotated geometric structure of the Structure C MCHS. The length L, width W and height H of the MCHS are 12 mm, 10.4 mm and 2.2 mm, respectively. The height h_c and width w_c of each channel are set as 0.8 mm and 0.5 mm, and the length of channel is equal to the length l. Figure 3.11(b) shows the different geometrical shapes of the micro pin-fins. The height of micro pin-fins h_p is 0.2 mm, while the characteristic lengths for the different geometries. All the micro pin-fin configurations in Figure 3.11(b) have the same volume, equivalent to the volume of the circle shaped fin determined by $0.05^2\pi \times 0.2\ mm^3 (A_{circle} \times h_p)$. This eliminates the effect of different volumes in the channels on the flow rate, which can lead to errors in thermal performance. Spacing of adjacent micro pin-fins varies from 0.3 mm to 0.9 mm with an increment of 0.3 mm. A constant heat flux q_{in} is applied to the bottom of the MCHS. u_{in} and u_{out} are inlet and outlet velocity, respectively. Table 3.7 gives the dimensions of MCHS.

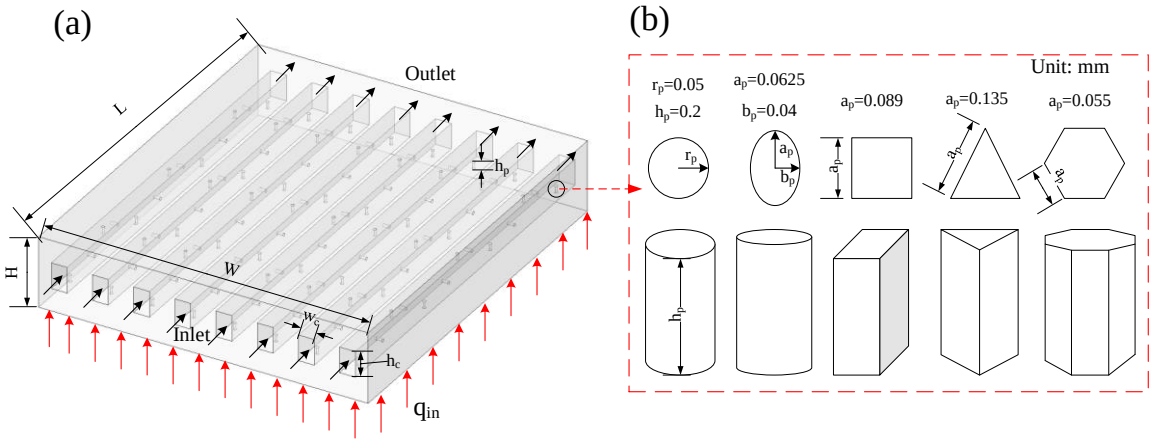

Figure 3-11 (a) View of Structure C and (b) Geometrical shapes of the micro pin-fins.

Table 3-7 Dimensions of MCHS

Dimensions of MCHS	
L	12 mm
W	10.4 mm
H	2.2 mm
h_c	0.8 mm
w_c	0.5 mm
h_p	0.2 mm

3.3.2. Governing equations

Below are the equations that govern the fluid flow in a single microchannel.

Equation (1) shows how the continuity equation for the incompressible flow was determined:

$$\rho\left(\frac{\partial u}{\partial x}+\frac{\partial v}{\partial y}+\frac{\partial w}{\partial z}\right)=0 \tag{3.25}$$

With the thermal properties assumed constant, X, Y and Z momentums were determined using Equations (3.26, 3.27 and 3.28):

X-momentum:

$$\rho\left(u\frac{\partial u}{\partial x}+v\frac{\partial u}{\partial y}+W\frac{\partial u}{\partial z}\right)=\frac{\partial}{\partial x}\left(\mu\frac{\partial u}{\partial x}\right)+\frac{\partial}{\partial Y}\left(\mu\frac{\partial u}{\partial y}\right)+\frac{\partial}{\partial z}\left(\mu\frac{\partial u}{\partial z}\right)-\frac{\partial p}{\partial x} \tag{3.26}$$

Y-momentum:

$$\rho\left(u\frac{\partial v}{\partial x}+v\frac{\partial v}{\partial y}+W\frac{\partial v}{\partial z}\right)=\frac{\partial}{\partial x}\left(\mu\frac{\partial v}{\partial x}\right)+\frac{\partial}{\partial Y}\left(\mu\frac{\partial v}{\partial y}\right)+\frac{\partial}{\partial z}\left(\mu\frac{\partial v}{\partial z}\right)-\frac{\partial p}{\partial x} \tag{3.27}$$

Z-momentum:

$$\rho\left(u\frac{\partial w}{\partial x}+v\frac{\partial w}{\partial y}+W\frac{\partial w}{\partial z}\right)=\frac{\partial}{\partial x}\left(\mu\frac{\partial w}{\partial x}\right)+\frac{\partial}{\partial Y}\left(\mu\frac{\partial w}{\partial y}\right)+\frac{\partial}{\partial z}\left(\mu\frac{\partial w}{\partial z}\right)-\frac{\partial p}{\partial x} \quad (3.28)$$

Ignoring the viscous energy dissipation, which is defined by $\mu_f\left[2\left(\frac{\partial u_i}{\partial x_i}\right)^2+\left(\frac{\partial u_j}{\partial x_i}+\frac{\partial u_i}{\partial x_j}\right)^2\right]$, energy was determined using Equation (3.29):

$$\rho c_p\left(u\frac{\partial T}{\partial x}+v\frac{\partial T}{\partial y}+W\frac{\partial T}{\partial z}\right)=\frac{\partial}{\partial x}\left(k_f\frac{\partial T}{\partial x}\right)+\frac{\partial}{\partial y}\left(k_f\frac{\partial T}{\partial y}\right)+\frac{\partial}{\partial z}\left(k_f\frac{\partial T}{\partial z}\right) \quad (3.29)$$

Where k_f is the thermal conductivity of coolant.

3.3.2. Boundary conditions

In the case of microchannel cooling, the following assumptions were made:

- Working fluid is in a steady flow.
- Working fluid is incompressible.
- Working fluid flow is laminar with Reynolds number ranging from 100 to 1000, since the cross-section of microchannels used is very small.
- Gravitational effect can be neglected.

In Figure 1b, the boundary condition were used as follows: A consistent velocity and temperature were utilized for the inlet:

$$u=u_{in}, v=0, w=0, T=T_{in}=293K \quad (3.30)$$

The outlet boundary condition was set as zero pressure. Standard wall functions were applied for the near-wall treatment. In the solid-fluid interface:

$$\vec{V}=0, T=T_s, k_f\nabla T=k_s\nabla T_s \quad (3.31)$$

An adiabatic boundary condition was applied to the insulated walls:

$$k_s \nabla T_s = 0 \tag{3.32}$$

For the bottom wall:

$$q_w = -k_s \frac{\partial T_s}{\partial n} \tag{3.33}$$

The used in this research is 100 kW/m^2, when using water as the coolant, specific heat was set as 4.182 kJ/kg·K, density was equal to $998.2\ \mathrm{kg/m^3}$, viscosity was set to $1.003 \times 10^3\ \mathrm{kg/m \cdot s}$ and thermal conductivity was $0.6\ \mathrm{W/m \cdot K}$. For the respective of materials of heat sink, the possible candidate materials for MCHS fabrication includes aluminum, copper, silicon, and silver [167], which were chosen as the simulated heat sink materials in this chapter. The related properties (ρ_s, $c_{p,s}$, k_s) are shown in Table 3.8. Pressure boundary condition can be considered that outlet of channels pressure value is equal to atmospheric condition (1 gauge bar).

Table 3-8 Properties of heat sink materials in simulation [167].

Materials	Density ρ_s ($\mathrm{kg/m^3}$)	Specific heat capacity $c_{p,s}$ ($\mathrm{J/kg \cdot K}$)	Thermal conductivity k_s ($\mathrm{W/m \cdot K}$)
Silicon	2329	710	149
Aluminum	2719	871	202.4
Copper	8978	381	387.6
Silver	10490	235	429

3.3.3. Physical parameters of the GO/MECPM slurry

The physical parameters of graphene oxide/MEPCM with different GO content used in the simulation is in Table 3.9 [164].

Table 3-9 Thermophysical properties of GO/MEPCM slurry with different GO weight fraction.

Sample	Tm (°C)	Tc (°C)	ΔHm(J/g)	Thermal conductivity (W/m·K)
MEPCM	27.33	26.03	223.6	0.225
GO/MEPCM-(0.1 w.t.% GO)	26.64	25.61	208.9	0.285
GO/MEPCM-(0.2 w.t.% GO)	26.97	25.05	210.5	0.369
GO/MEPCM-(0.3 w.t.% GO)	26.59	25.92	206.1	0.504
GO/MEPCM-(0.4 w.t.% GO)	26.66	25.92	207.6	0.672
GO/MEPCM-(0.5 w.t.% GO)	26.65	25.79	190.4	0.706

The density of the GO/MEPCM slurry is expressed as follows [160]:

$$\frac{1}{\rho_S} = \frac{\omega}{\rho_p} + \frac{1-\omega}{\rho_w} \tag{3.34}$$

Where ω is mass fraction of GO/MEPCM, which is set as 5 wt% in this research, the density of the MEPCM was 1033 kg/m^3 [164].

The slurry viscosity is calculated by Batchelor model and the complex derivation process can be found in [168]:

$$\mu_S = \mu_w(1 + 2.5\phi + 6.5\phi^2) \tag{3.35}$$

Where the ϕ is the volume fraction of GO/MEPCM, The thermal conductivity of GO/MEPCM slurry is determined using Maxwell model and the detailed complex derivation process can be found in [169]:

$$k_S = \frac{2k_w + k_p + 2\phi(k_p - k_w)}{2k_w + k_p - \phi(k_p - k_w)} \cdot k_w \tag{3.36}$$

$$\phi = \omega\frac{\rho_s}{\rho_p} \tag{3.37}$$

The piecewise model is employed to describe the heat capacity of GO/MEPCM slurry [164]:

$$c_{p,S} = \begin{cases} \omega c_{p,p} + (1-\omega)c_{p,w} & T < T_1 \\ \omega c_{p,p} + (1-\omega)c_{p,w} + \frac{h_{sf}}{T_2 - T_1} & T_1 < T < T_2 \\ \omega c_{p,p} + (1-\omega)c_{p,w} & T > T_2 \end{cases} \tag{3.38}$$

where h_{sf} is the latent heat of the GO/MEPCM slurry, calculated by multiplying the mass fraction by the latent heat of the MPCM particles. T_1 and T_2 denote the initial and final temperatures of the melting range, respectively.

3.3.5. Data reduction

The hydraulic diameter of microchannel is very important to calculate Reynolds number and average Nusselt number. It can be expressed by Equation (3.39):

$$D_h = \frac{2h_c w_c}{h_c + w_c} \tag{3.39}$$

where h_c and w_c are height and width of microchannel mentioned in Figure 3.5.

The hydraulic diameter of each channel in the current work, h_c and w_c for all models were found to be constant, at D_h = 0.6154 mm.

The Reynolds number was calculated using Equation (3.40):

$$Re = \frac{\rho_f u_{in} D_h}{\mu} \tag{3.40}$$

Where u_{in} is mean velocity. To ensure laminar flow within the microchannel, Re in the range from 100 to 1000 is employed, and corresponding uniform velocity is provided at the inlet face of fluid domain.

In this work, uniform inlet velocity of working fluid was calculated at a given Reynolds number using Equation (3.41).

$$u_{in} = \frac{Re\mu}{\rho_f D_h} \tag{3.41}$$

The thermal resistance of water ($R_{\mathrm{heat},mean}$) is influenced by factors such as the density, flow rate and specific heat of the fluid. If considering the fluid's reference temperature as T_{ref}, we can calculate the average thermal resistance of the fluid using Equations (3.42 and 3.43) as follows [170]:

$$R_{\mathrm{heat},mean} = \frac{T_{ref} - T_{in}}{q_{in}} \tag{3.42}$$

$$T_{ref} = \frac{T_{in} - T_{out}}{2} \tag{3.43}$$

Where T_{in} is inlet temperature and T_{out} is the outlet temperature of the coolant.

The average convective thermal resistance can be calculated using Equation (3.44), which takes into account the average temperature of the base of the heat sink ($T_{base,mean}$):

$$R_{conv,mean} = \frac{T_{base,mean} - T_{ref}}{q_{in}} \tag{3.44}$$

The average thermal conductivity thermal resistance is expressed by Equation (3.45):

$$R_{cond,mean} = \frac{T_{base,mean} - T_{ref}}{q_{in}} \tag{3.45}$$

Where $T_{base,mean}$ is the average surface temperature inside the microchannel.

The total average thermal resistance can be determined by employing Equation (3.46):

$$R_{tot} = R_{\mathrm{heat},mean} + R_{conv,mean} + R_{cond,mean} \tag{3.46}$$

The pressure drop was calculated using Equation (3.47):

$$\Delta p = p_{in} - p_{out} \tag{3.47}$$

Based on the boundary conditions, p_{out} is atmospheric pressure. Thus, the expression can be simplified by Equation (3.48).

$$\Delta p = p_{in} \tag{3.48}$$

Inlet temperature of fluid was set to 20 ℃. Dimensionless temperature at the outlet of channels can be defined by Equation (3.49):

$$T' = \frac{T_{out} - T_{in}}{T_{w,avg} - T_{in}} \tag{3.49}$$

where the $T_{w,avg}$ is the average temperature of the wall. The larger outlet temperature makes larger T', resulting from the increased heat dissipated by fluid; thus, it is a direct way to measure the value of T' to evaluate the heat transfer capacity.

The local convective heat transfer coefficient and the local Nusselt number are defined as

$$h(x) = \frac{q_{in} A_f}{A_c \left[T_W(x) - T_f(x) \right]} \tag{3.50}$$

$$Nu(x) = \frac{h(x) D}{k_f} \tag{3.51}$$

where q_{in} represents the heat flux at the silicon substrate, A_f is the contact surface area of coolant and silicon in a single microchannel, A_c is the convection heat transfer area of different shapes of pin-fins, as shown in Table 3.10, and the and k_f is the thermal conductivity of the coolant.

$T_W(x)$ and $T_f(x)$ are the local conduction wall temperature and the local bulk fluid temperature, respectively, defined as:

$$T_W(x) = \frac{1}{y} \int_y T_w(x, y, 0) \cdot \mathrm{d}y \tag{3.52}$$

$$T_f(x) = \frac{\int_{Ac} \rho u(x, y, z)\, c_p T_f(x, y, z) \cdot dA_c}{\int_{Ac} \rho u(x, y, z) c_p \cdot dA_c} \tag{3.53}$$

The average Nusselt number can be obtained by:

$$Nu = \frac{1}{L} \int_L Nu(x) \cdot \mathrm{d}x \tag{3.54}$$

The friction factor is given below;

$$f = \frac{2 \Delta p D_h}{\rho_f L u_m^2} \tag{3.55}$$

The overall performance evaluation criterion (PEC) was proposed by Webb [171] to evaluate a comprehensive effect on heat transfer performance and fluid flow characteristics, which can be calculated as:

$$PEC = \frac{\left(\frac{Nu}{Nu_0}\right)}{\left(\frac{f}{f_0}\right)^{\frac{1}{3}}} \tag{3.56}$$

where Nu_0 and f_0 are Nusselt number and friction coefficient of a rectangular straight microchannel

Pumping power is evaluated as;

$$P = v_f A_{cs} \tag{3.57}$$

Table 3-10 Convection heat transfer area of different shapes of pin-fins.

Fin geometry	Convection heat transfer area A_c (m^2)
Un-finned	0.0002496
Circle	0.00025611
Ellipse	0.00025634
Square	0.00025697
Triangle	0.00025801
Hexagon	0.00025646

3.3.6. Simulation Methodology

ANSYS 2022 R2 was used to simulate the thermal behaviour of MCHS with micro pin-fins. 3D models developed in SolidWorks 2022 were imported, labelled, and meshed in ANSYS Workbench. Second order upwind scheme and the SIMPLE algorithm [172] were chosen to discretize the momentum and energy equations and the pressure velocity coupling. For residuals, apart from the criterion of energy was set to 10^{-6}, the criteria for continuity and velocity in x, y and z directions are set to 10^{-3}.

3.3.7. Grid independence study

The models were meshed based on finite volume method (FVM). The grid independence test is necessary to ensure not only the accuracy and reliability of results but the minimum number of grids that can help shorten simulation time and maintain the integrity of results. The test was carried out using the Structure A model with 0.9 mm-spaced micro pin-fins and Re=100. Figure 3.12 shows grid distribution of MCHS with grid number of 3124528. Hexahedral structured grids were used to discretize the entire computational domain. Six different sizes as shown in Table 3.11 were evaluated and the outlet temperature obtained presented in Figure 3.13. It was clearly noticed that the value obtained when grid numbers were between 3124528 and 3751895 was so similar that any error can be ignored. Thus, to increase computational speed, Grid 5 with grid number: 3124528, was selected for all the numerical simulations.

Table 3-11 Grid size and number

	Grid 1	Grid 2	Grid 3	Grid 4	Grid 5	Grid 6

Number of grids	534994	1118684	1602276	2729716	3124528	3751895

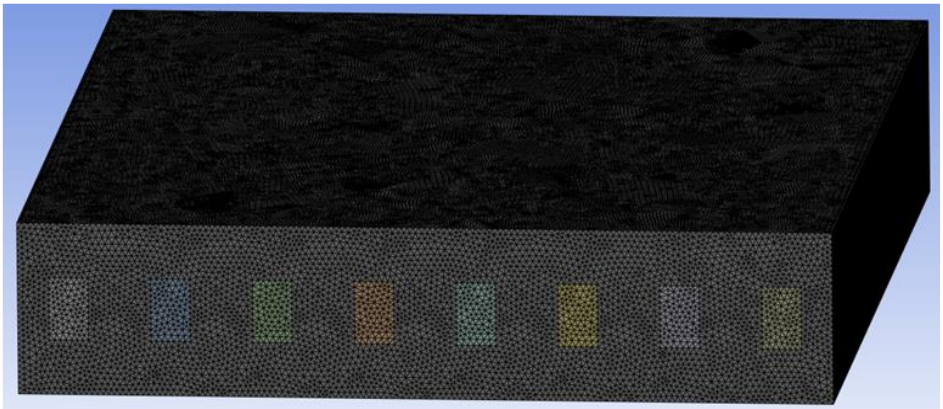

Figure 3-12 Meshing of the heat sink with grid number of 3124528.

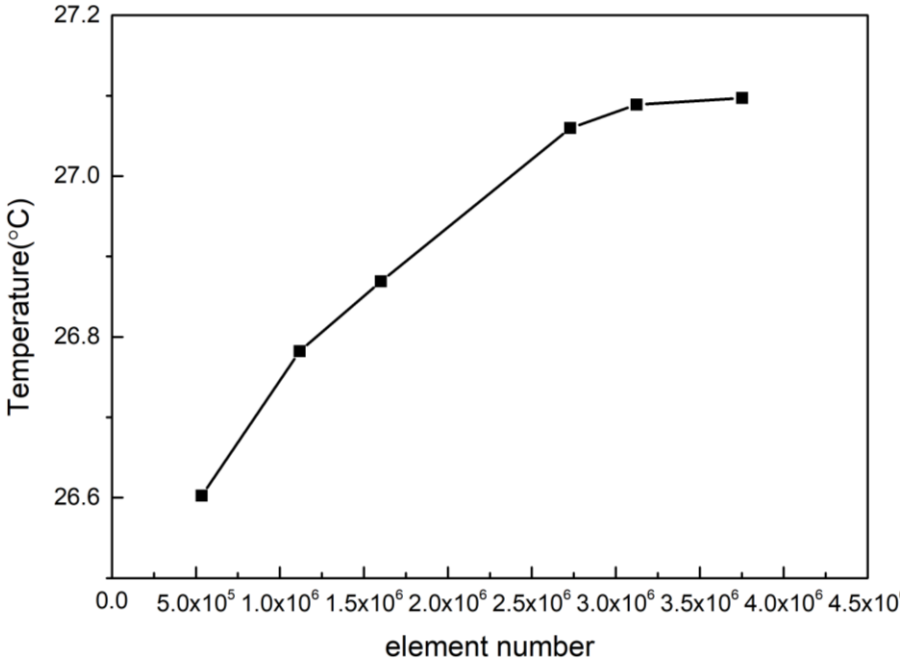

Figure 3-13 Result of grid size validation

3.3.8. Model validation

Before proceeding to the numerical model of MCHS with micro pin-fins, it is necessary to validate the model with published results. The present data was reproduced and compared to the simulation conducted by Gunnasegaran et al. [130]. The comparative results presented in Figure 3.14 shows consistency in the relationship between temperature rise of working fluid and increasing Reynolds number for rectangular shaped microchannel. Our present numerical results show great agreement with work by Gunnasegaran et al. [130], providing validation for our MCHS model with micro pin-fins.

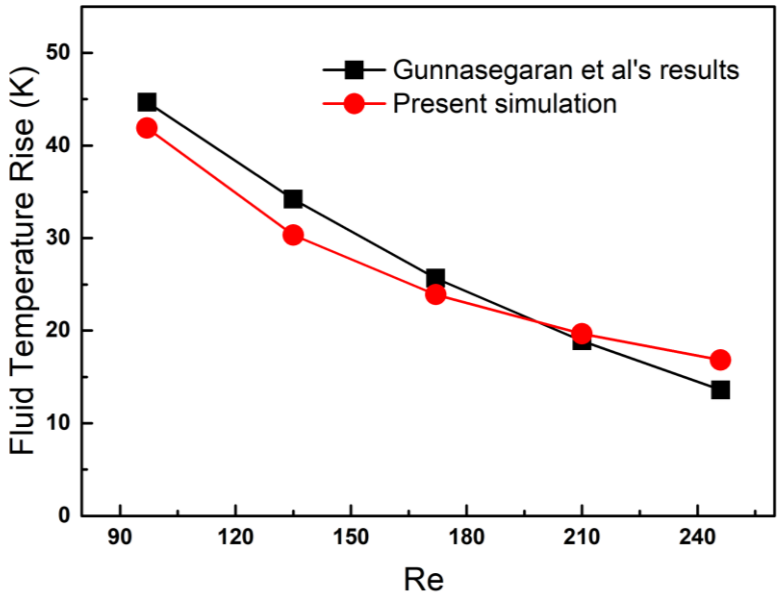

Figure 3-14 Validation of present simulation of rectangular shaped microchannel with similar work by Gunnasegaran et al. [130].

3.4. Synthesis of Graphene/MEPCM based on Microfluidic device

3.4.1. Microfluidic devices fabrication

The needle-based microfluidic device comprise of some readily available items, including transparent polyethylene (PE) tubing, transparent polypropylene (PP), cross-links PP male luer fittings, stainless steel dispensing needles, transparent silicone tubing and transparent PP tee-links. As shown in Figure 3.15, the coaxial microfluidic device comprise of the coaxial part and the coflow part, which were constructed using three dispensing needles, two male luer fittings, one tee-ink and one cross-link. A 1/2 inch 19 G dispensing needle (ID = 0.84 mm, OD = 1.08 mm), a 1 inch 18 G capillary glass tube (ID = 0.9 mm, OD = 1.1 mm), and a 1.6 mm cross-link were utilized to form the coaxial part. Then, insert the 2.0 inch 23G neelde (ID=0.33 mm, OD=0.63 mm) into the 19G needle through the T-shaped connector (TL= 20 mm, ID= 1.0 mm, OD=1.6 mm) and the male luer connector (TL=14 mm, ID=1 mm, OD=1.6%) to assemble coflow part.

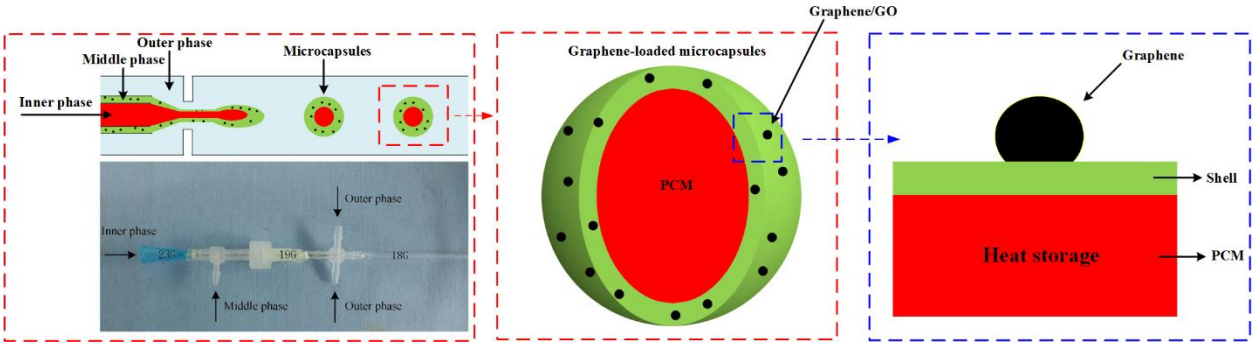

Figure 3-15 Schematic diagram of the graphene-loaded PCM microcapsules fabricated by the needle-based microfluidic device and the thermal control system.

3.4.2. Fabrication of MEPCM and graphene modified MEPCM

Paraffin materials as PCMs have been widely used in many fields due to their advantages of cheap, reliable, safe and high latent heat [21]. In this chapter, n-hexadecane (Aladdin Chemistry Co., Ltd., China) was selected as the paraffin material and utilized as the inner phase fluid. HDDA (Aladdin

Chemistry Co., Ltd., China), 2.0 wt% 2-hydroxy-2-methyl-1-phenyl-1-propanone (HMPP, Aladdin Chemistry Co., Ltd., China) with or without certain content of graphene/GO was used as the middle phase fluid. HMPP (Aladdin Chemistry Co., Ltd., China) was the photoinitiator, which enables to trigger the polymerization of HDDA under UV radiation. Deionized water containing 8.0 wt% polyvinyl alcohol (PVA, Aladdin Chemistry Co., Ltd., China) and 2% poly(ethylene alycol)-block- ran poly(propylene glycol)-block-poly(ethylene qlycol) (Aladdin Chemistry Co., Ltd., China) was used as the outer phase fluid. The single emulsion droplets were formed at coaxial section, then the droplets further develop into double emulsion droplets after flowing into the coflow section. The geometric structure and size the O/O/W double emulsion droplets were adjusted by controlling the flow rate of inner phase. The prepared droplets completed the photopolymerization reaction in the capillary glass tube under UV radiation (365nm), forming microcapsules with core-shell structure. After being filtered, washed and dried, microcapsules were finally obtained.

3.4.3. Characterization of MEPCM and graphene modified MEPCM

O/O/W micro droplets were monitored by an optical microscope (N-800F, Yongxin Optec Instrument Co., Ltd., China) equipped with a high-speed camera (20 megapixel, NOVEL, Yongxin Optec Instrument Co., Ltd., China). Scanning electron microscope (JCM 7000, ZEISS, Germany) was used to examine the surface morphology of microcapsules. The mechanical strength of microcapsules was measured using a Discovery Hybrid Rheometer (DHR-30, WATERS Co., Ltd., China). The average size and coefficient of variation (C_v) of the droplets/capsules were determined by measuring the size of the double emulsion droplets from the recorded pictures using ImageJ, where C_v is the value calculated by the ratio of the average size of the microcapsules to the

standard deviation of particle size. The phase change properties of microcapsules were measured by differential scanning calorimetry (DSC 214, Netzsch, Germany). In order to evaluate the thermal stability and durability of microcapsules, 80th thermal cycle tests were conducted and the phase change processes were monitored using an optical microscope to observe the morphological changes of the shell material. In this project, DSC and SEM tests were carried out more than 3 times under every fixed condition to reduce the uncertainty of experiments.

3.4. Summary

In this chapter, the methodology used for simulations and experiments has been summarized. This mainly includes the model description of the generation and rupture of phase change material droplets in microchannels, the equations used, boundary conditions, and solution methods. In addition, this chapter also summarizes the model description, control equations, boundary conditions, physical parameters and solution methods used to simulate the impact of graphene enhanced phase change microcapsule slurry on microchannel heat dissipation performance. Finally, the development of microfluidic devices to produce graphene/MEPCM, the techniques for creating MEPCM and graphene/MEPCM, as well as the methods used to characterize the properties of both MEPCM and graphene/MEPCM are discussed.

Chapter 4 - The Formation and Solidification of PCM droplet in microfluidic channel

To study the effect of continuous phase velocity, interfacial tension, continuous phase temperature and cooling wall temperature on the droplet formation and solidification process, various combinations of parameters are used for simulation and the different cases are summarized in Table 4.1.

Table 4-1 Details of different cases.

Study		Continuous phase flow rate (m/s)	Interfacial tension (N/m)	Continuous phase temperature at inlet (K)	Cooling wall temperature (K)
Effect of continuous phase flow rate	Case01	0.02	0.09	260	260
	Case02	0.04	0.09	260	260
	Case03	0.06	0.09	260	260
	Case04	0.08	0.09	260	260
Effect of interface tension	Case05	0.04	0.05	260	260
	Case06	0.04	0.12	260	260
	Case07	0.04	0.16	260	260
Effect of continuous	Case08	0.04	0.09	250	260
	Case09	0.04	0.09	255	260

phase temperature at inlet	Case10	0.04	0.09	265	260
Effect of cooling wall temperature	Case11	0.04	0.09	260	250
	Case12	0.04	0.09	260	255
	Case13	0.04	0.09	260	265

4.1. Characteristics of LMPA droplet formation and solidification

Figure 4.1 and Figure 4.2 respectively shows the simulation results of the LMPA droplet formation and solidification process in the flow-focusing microfluidic device for case 2, where the dispersed phase temperature at inlet is set as 290 K in all considered cases. The mixed phase in the phase transition state is described by liquid fraction. As shown in the Figure 4.2, the continuous phase is always in liquid state, for the dispersed phase, liquid fraction $F = 1$ represents liquid LMPA, $0 < F < 1$ represents solidifying LMPA, and $F = 0$ represents solidified LMPA droplet. In early stage, there is no solidified LMPA, as dispersed phase temperature inside droplet is still higher than solidifying temperature and the LMPA droplet is still liquid. As the formed droplet goes along the microchannel, the LMPA solidification ratio increases gradually. As shown in Figure 4.3, the temperature of the liquid droplets in the microchannel is obviously higher than that of the continuous phase. Besides, the temperature of the liquid droplets gradually decreases along the microchannel, and there exists a critical position in the microchannel where the liquid droplets are completely solidified. Figure 4.4 shows the temperature curves of the three different monitor points (monitor point 1, 2, 3 as shown in Figure 3.1(a)) in the microchannel with time. It can be seen that,

after a certain period of time, the temperatures of the three monitor points change periodically with basically fixed frequency and amplitude. This is because there exists a relatively large temperature difference between the continuous phase and the dispersed phase. When there is no liquid droplet observed at the monitor point, the temperatures at the monitor points are greatly influenced by the cooling wall temperature and the continuous phase temperature, which will result in a lower However, when the LMPA droplets pass by the monitor points, as the liquid droplets have not received enough time to reach the thermal equilibrium with surrounding continuous phase. Therefore, the temperatures are still high in the monitor positions. However, as can be seen from Figure 4.4, the maximum and minimum temperature values of monitoring points 1, 2 and 3 decrease in turn, which is because the droplets exchange heat with the surrounding continuous phase during passing through these monitor points. As only when the droplets reach the monitor points, the temperature at the monitor points will rise, while the temperature at the monitor points will drop after the droplets leave. Therefore, the required time for producing a single droplet can be calculated by $\Delta t = t_1 - t_2$, as shown in Figure 4.4, where t_1 and t_2 are the times when two consecutive droplets pass through monitor point 2 respectively. The generation frequency of LMPA droplet is the reciprocal of Δt.

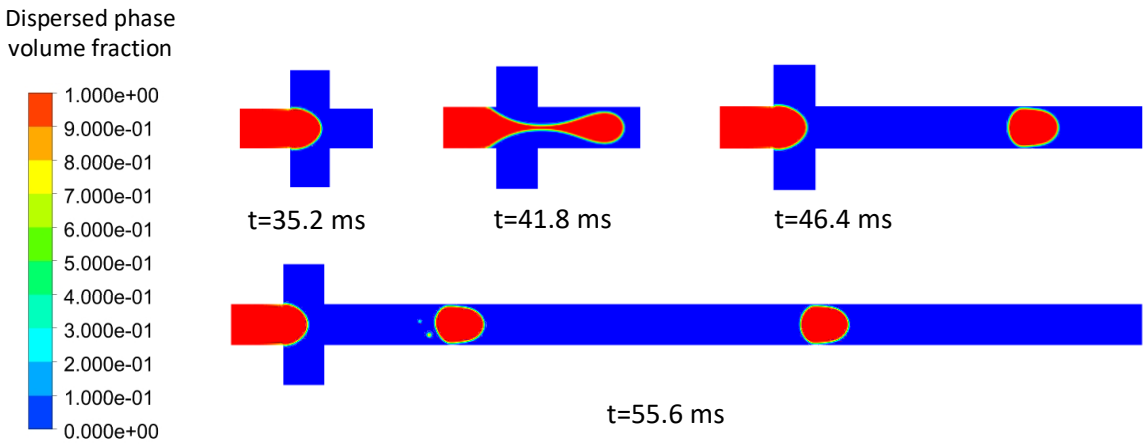

Figure 4-1 Dispersed phase volume fraction changes with time.

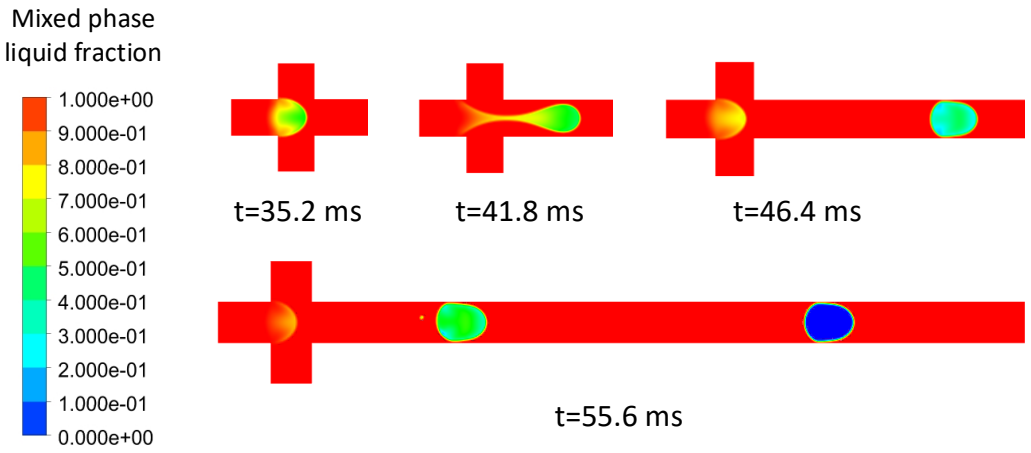

Figure 4-2 Mixed phase liquid fraction changes with time.

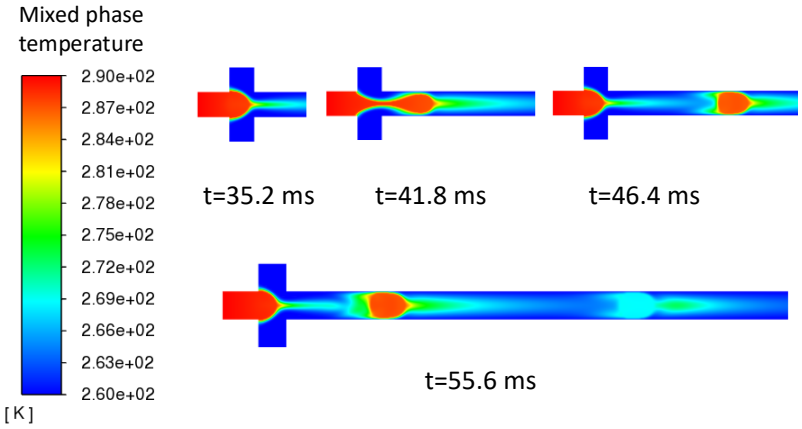

Figure 4-3 Profile of mixed phase temperature at different time.

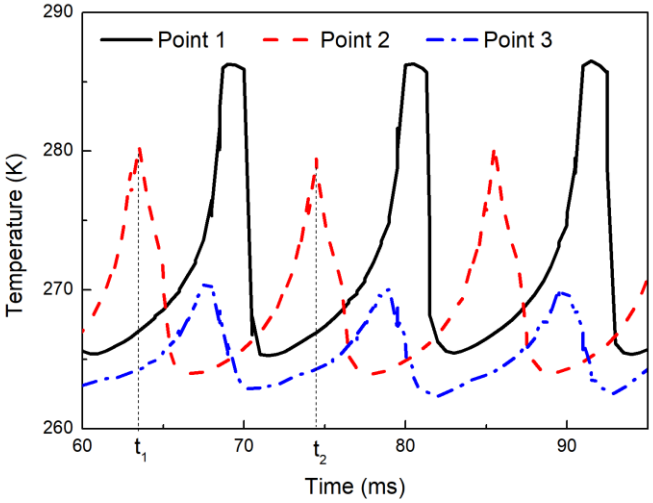

Figure 4-4 Temperature variations at monitoring points 1~3, for case 3.

4.2. Effect of continuous phase velocity

In this section, the velocity of the continuous phase was changed from 0.02 m/s to 0.08 m/s and kept all the other parameters unchanged as Table 4.1 (case1, 2, 3, 4). The visual comparison for

the generation and solidification process of LMPA droplets at different continuous phase velocities is given in Figure 4.5. It is can be seen that the continuous phase velocity greatly affects the droplet generation process, and the equivalent diameter gradually decreases with increasing continuous phase velocity, which is due to the shear force of the continuous phase as a pressure acting on the dispersed phase to detach the droplet. Table 4.2 gives that the frequency of droplet generation increases as the continuous phase velocity increases. This is because the shear force leads to faster splitting into the continuous phase, thus increasing the droplet formation frequency. These results are consistent with the previous experimental data [48]. In addition, Figure 4.5 also shows that at a lower flow rate, the droplets are completely solidified closer to the inlet, which means that increasing the continuous phase velocity can increase the distance between the first solidified droplet and the inlet of the microchannel under given conditions. Figure 4.6 indicates that the temperature distribution of the continuous phase in the channel is almost unaffected by the continuous phase velocity. However, it is clearly given in Figure 4.7 that the time required for a single droplet from initial formation to complete solidification first increases and then decreases with the increase of continuous phase velocity, which is possibly due to the comprehensive effect of lower temperature when the larger droplets are generated and the rapid heat transfer rate between the smaller droplets and the surrounding environment. Within the given continuous phase velocity range, LMPA droplets with relatively large size are produced when the velocity is less than or equal to 0.04 m/s (case 1, 2), and the temperature of the larger droplets (case 1) is lower than that of the smaller droplets (case 2) just produced. In this case, the influence of the lower temperature on the solidification time exceeds that of the rapid heat transfer between the smaller droplets and the surrounding environment, and thus the time required for a single droplet

solidification increases with the increase of continuous phase temperature. On the contrary, when the continuous phase velocity is greater than or equal to 0.04 m/s (case 2, 3, 4), although the larger droplets just formed have relatively lower temperature, the rapid heat transfer between the smaller droplets and the surrounding environment has more influence on the solidification time than the lower temperature, and thus the time required for a single droplet solidification decreases with the increases of continuous phase temperature.

Table 4-2 The frequency of droplet generation at different continuous phase velocities.

Continuous phase velocity (m/s)	0.02	0.04	0.06	0.08
Frequency (Hz)	70.42	89.29	111.11	128.0

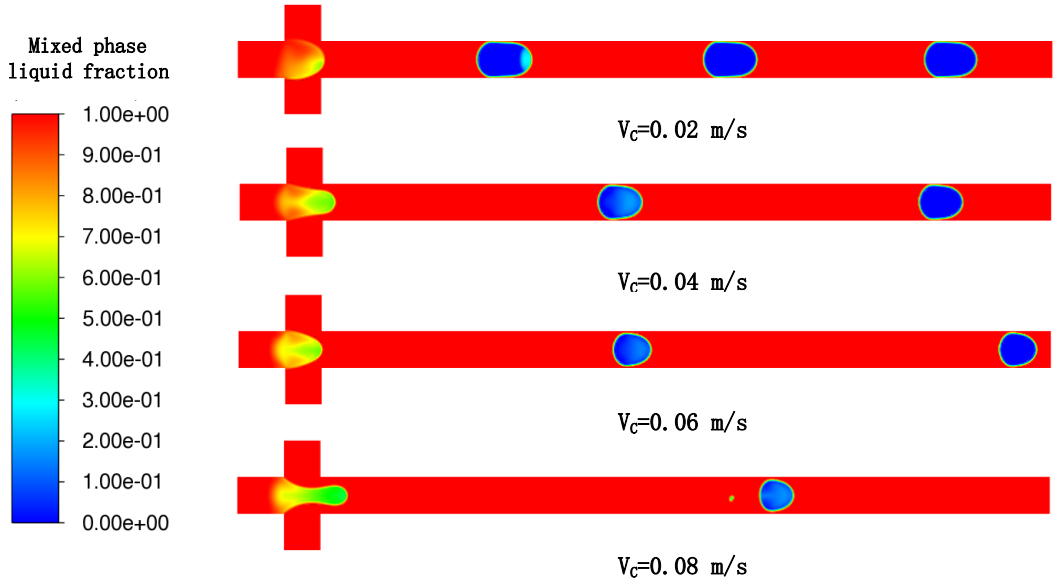

Figure 4-5 Variation of mixed phase liquid fraction at different continuous phase velocities.

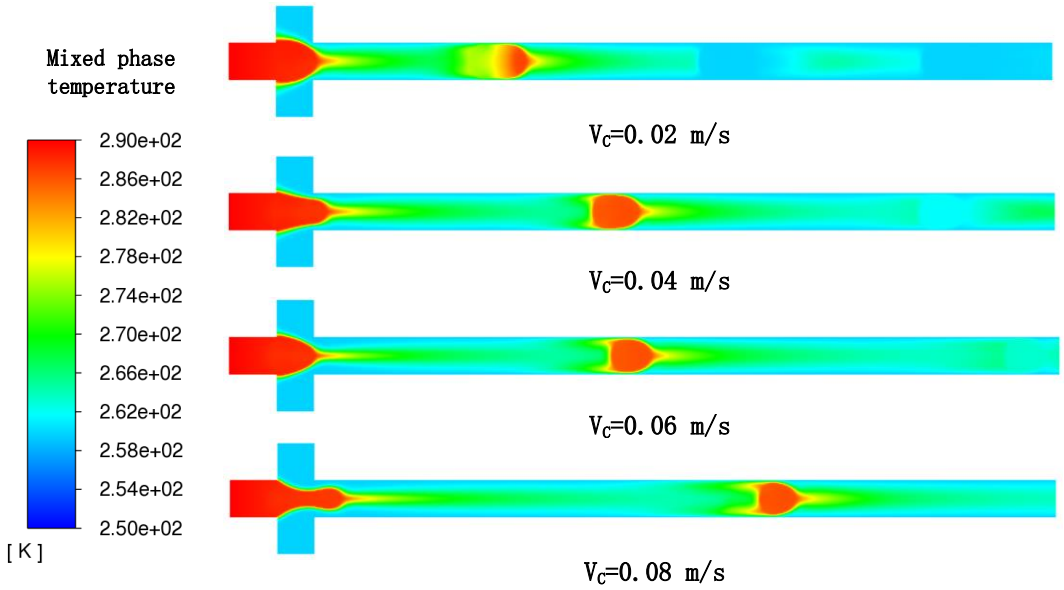

Figure 4-6 Profile of mixed phase temperature at different continuous phase velocities.

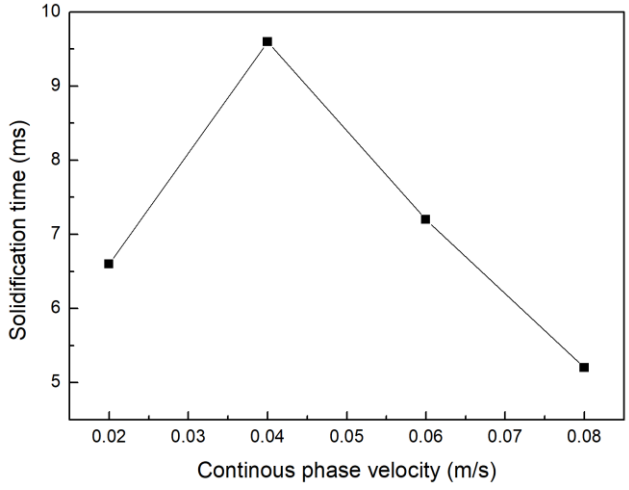

Figure 4-7 Required solidification time per droplet at different continuous phase velocities.

4.3. Effect of interfacial tension

Previous study shows that interfacial tension has a significantly effect on droplet stability and break up time [49]. In this section, the interfacial tension was changed from 0.05 to 0.16 N/m and all the other factors kept unchanged as Table 4.1 (case 2, 5, 6, 7). The visual comparison for the LMPA droplet generation and solidification at different interfacial tensions can be seen in Figure 4.8, which distinctly indicates that the droplet size increases with the increasing interfacial tension. For the frequency, Table 4.3 shows that it constantly decreases as the interfacial tension grows. This is because the viscous and shear force are suppressed at a higher surface tension value, which leads to the inward contraction of the liquid droplets due to the pressure affected by the interfacial tension. The higher interfacial tension between the two liquids contributes to lower frequency and higher droplet size. On the other hand, when the interfacial tension between liquids is lower, droplet with higher frequency and size are obtained. Figure 4.9 shows that the effect of interfacial tension on the temperature distribution of the continuous phase in the microchannel is not obvious. However, as shown in Figure 4.10, the required time for a droplet solidification constantly decreases with the increasing interfacial tension. This is mainly because, within a given interface tension range, the influence of the temperature at the initial formation of droplets on the solidification time exceeds the rapid heat transfer between smaller droplets and the surrounding environment. Therefore, the interface tension and the time required for droplet solidification are linearly related under given conditions.

Table 4-3 The frequency of droplet generation at different interface tensions.

Interfacial tension (m/s)	0.05	0.09	0.12	0.16
Frequency (Hz)	100.00	89.29	83.33	79.37

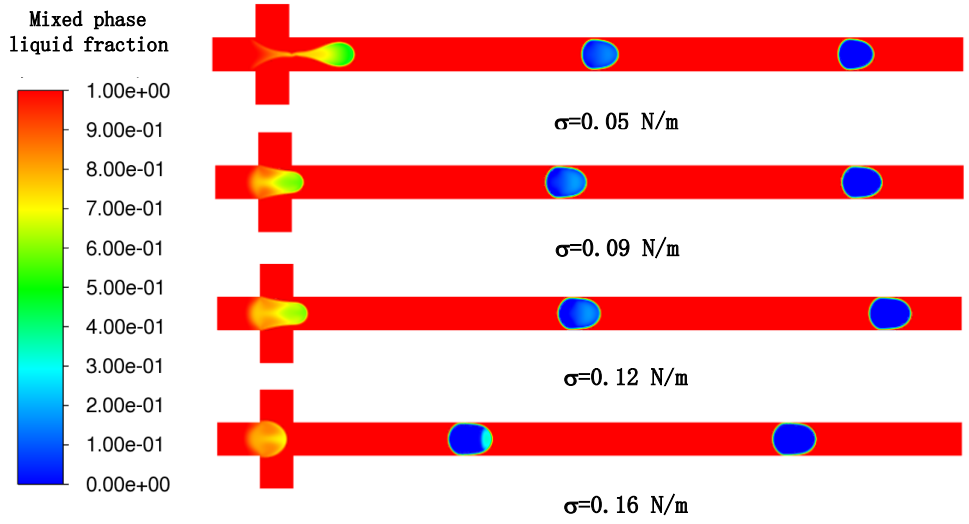

Figure 4-8 Profile of mixed phase liquid fraction at different interfacial tensions.

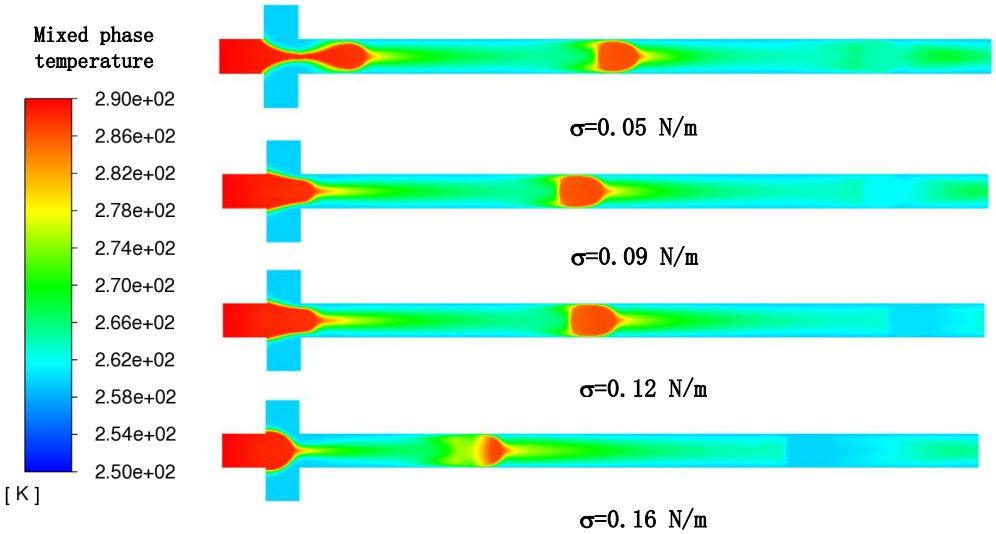

Figure 4-9 Profile of mixed phase temperature at different interfacial tensions.

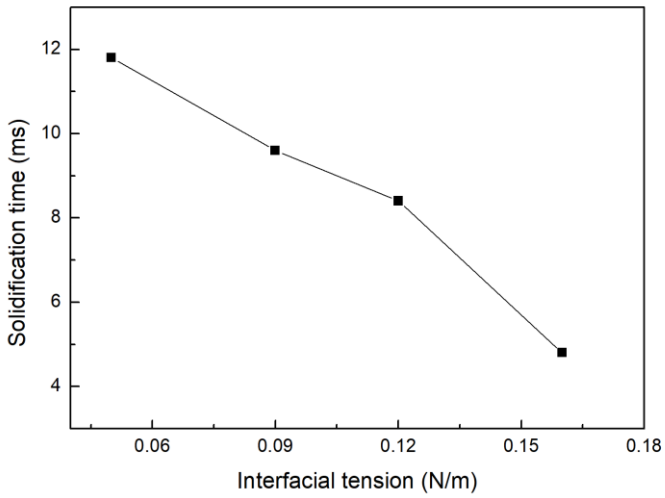

Figure 4-10 Required solidification time per droplet at different interfacial tensions.

4.3. Effect of continuous phase temperature

In this section, the continuous phase temperature was changed from 250 to 265 K and all the other parameters kept unchanged as Table 4.1 (case2, 8, 9, 10). The comparison of droplet formation and solidification progress at different continuous phase temperatures can be seen in Figure 4.11, which clearly indicates that the LMPA droplet size almost keeps unchanged as the continuous phase temperature increases. Besides, Table 4.4 shows that the droplet generation frequency also almost keeps unchanged with the increase of continuous phase temperature. These are possibly because the influence of the continuous phase temperature on the shear force or the velocity are not obvious under given temperature difference and thus barely affect the frequency and droplet size. However, the effect of continuous phase temperature on the droplet solidification process is

relatively obvious, it is observed from Figure 4.11 that the droplet that is almost completely solidified in the microchannel at different continuous phase temperatures is located in different positions in the microchannel. This is because increasing continuous phase temperature will reduce the temperature gradient along the main microchannel as it is shown in Figure 4.12, thus, it can be obtained that the droplets will solidify closer to the inlet at a lower continuous phase temperature. Figure 4.13 shows that the time required for a single droplet solidification increases with the increase of continuous phase temperature, which is mainly because increasing continuous temperature will reduce the heat transfer between droplets and the environment, and further slower the solidification process.

Table 4-4 The frequency of droplet generation at different continuous phase temperatures.

Continuous phase temperature (K)	250	255	260	265
Frequency (Hz)	90.91	90.91	89.29	89.29

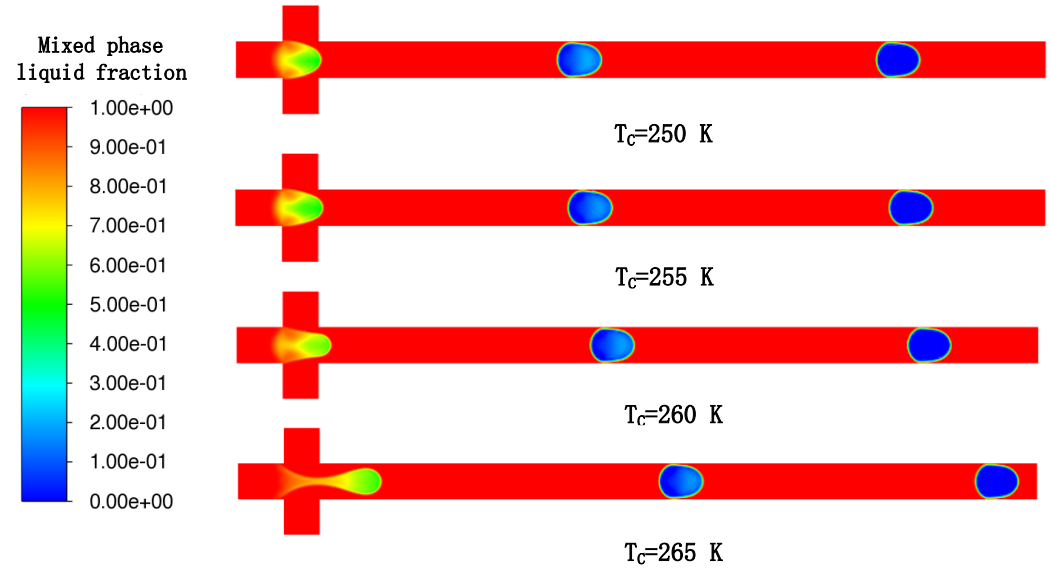

Figure 4-11 Profile of mixed phase liquid fraction at different continuous phase temperatures.

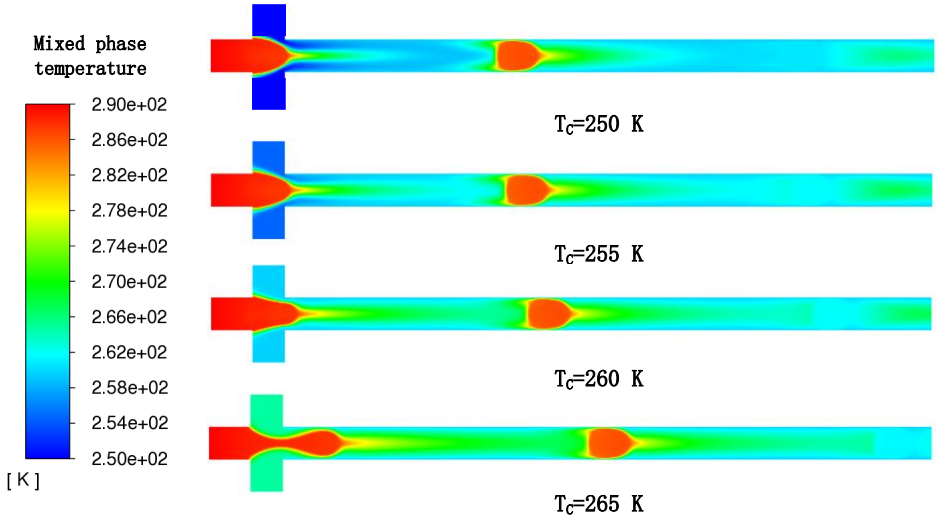

Figure 4-12 Profile of mixed phase temperature at different continuous phase temperatures.

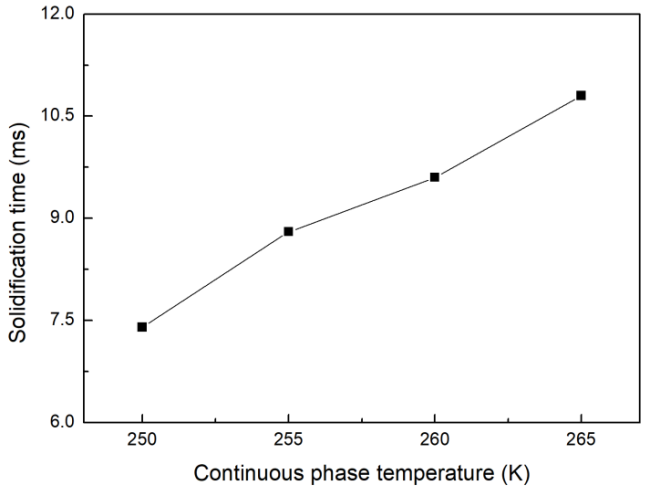

Figure 4-13 Required solidification time per droplet at different continuous phase temperatures.

4.4. Effect of cooling wall temperature

In this section, the cooling wall temperature was changed from 250 to 265 K and all the other parameters kept unchanged as Table 4.1 (case2, 11, 12, 13). The comparison of LMPA droplet formation and solidification progress at different cooling wall temperatures can be seen in Figure 4.14, which also clearly indicates that the droplet size almost keeps unchanged as the cooling wall temperature increases. Table 4.5 shows that the droplet generation frequency almost keeps unchanged with the increase of cooling wall temperature. This is possibly because that the influence of the cooling wall temperature on the shear force or the phase velocity are not obvious under given temperature difference and thus barely affect the frequency and droplet size. However, similar to the effect of continuous phase temperature on droplet solidification process, it is observed from Figure 4.14 that the droplet that is almost completely solidified in the microchannel at different cooling wall temperatures is located in different positions in the microchannel. This is because increasing cooling wall temperature will reduce the temperature gradient along the main

microchannel as shown in Figure 4.15, thus, it can be obtained that the droplets will solidify closer to the inlet at a lower continuous temperature. Figure 4.16 shows that the time required for a single droplet solidification increases with the increase of cooling wall temperature, which is mainly because increasing cooling wall temperature will reduce the heat transfer between droplets and the environment, and further slow down the droplet solidification process.

Table 4-5 The frequency of droplet generation at different cooling wall temperatures.

Continuous phase temperature (K)	250	255	260	265
Frequency (Hz)	90.91	89.29	89.29	89.29

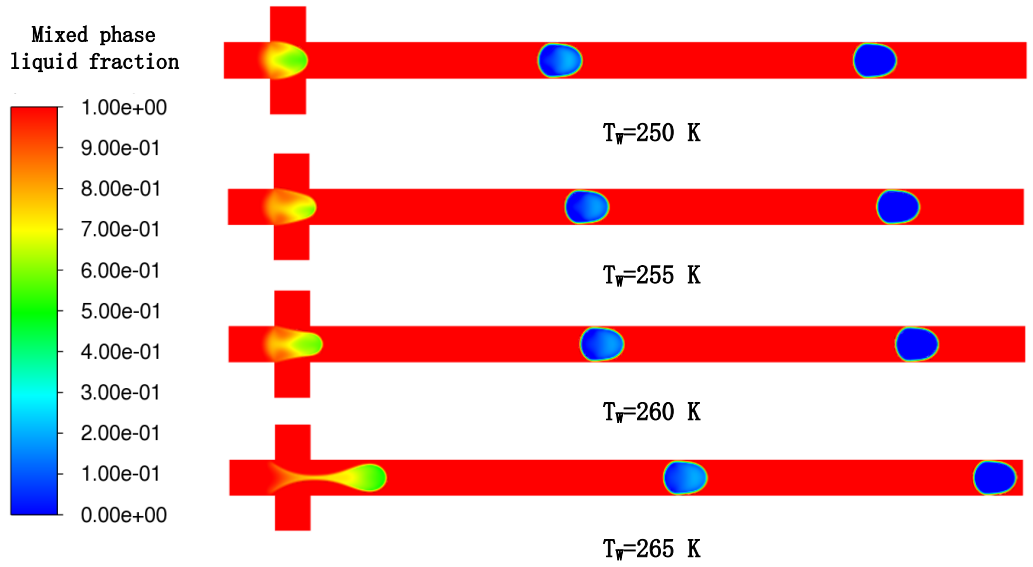

Figure 4-14 Profile of mixed phase liquid fraction at different cooling wall temperatures.

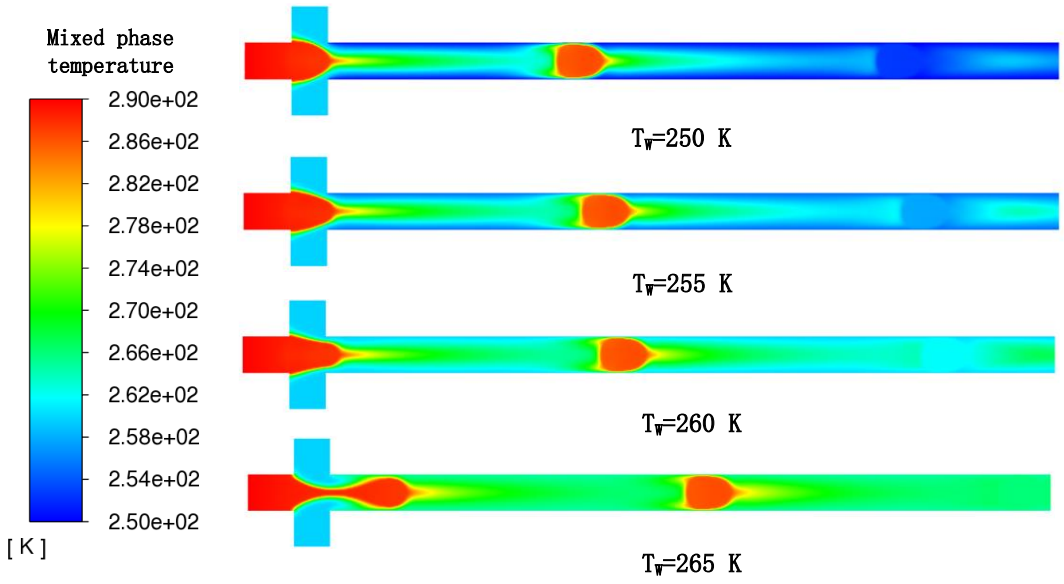

Figure 4-15 Profile of mixed phase temperature at different cooling wall temperatures.

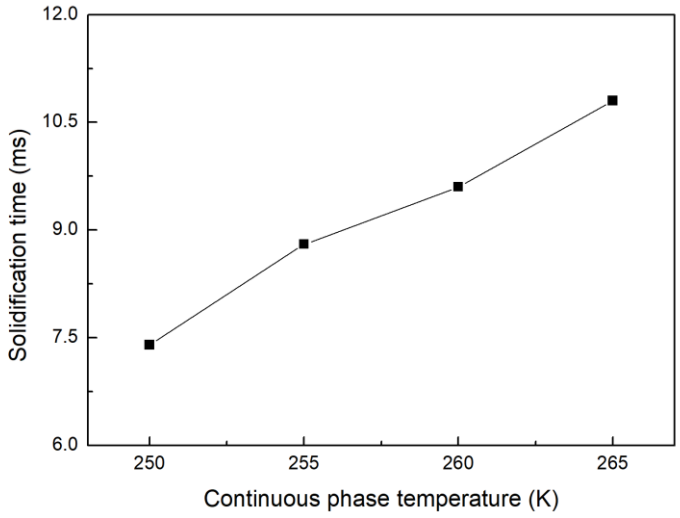

Figure 4-16 Required solidification time per droplet at different cooling wall temperatures.

4.5. Summary

In this chapter, a simplified two dimensional cross flow-focusing geometry model is given. Then a combination of VOF method and enthalpy-porosity method based on FLUENT code was applied to examine the effects of some key factors on the LMPA droplet formation and solidification process in a microfluidic device. The main results are as follows:

- Increasing the continuous phase velocity reduces the LMPA droplet size and simultaneously increases the droplet generation frequency. The variation of continuous phase velocity has little effect on the temperature distribution in the microchannel. The required time from droplet generation to complete solidification first increases and then decreases with increasing continuous phase velocity.
- Increasing the interfacial tension can increase the LMPA droplet size and simultaneously reduce the droplet generation frequency. The interface tension and the time required for droplet solidification are linearly related. The higher the interfacial tension, the shorter the required time from droplet generation to complete solidification.
- The continuous phase temperature has no obvious influence on the size and frequency of the generated droplets. However, it has a significantly influence on the temperature distribution and the process of LMPA droplet solidification in the microchannel. With the increase of continuous phase temperature, the required time for droplet solidification gradually decreases.
- Similar to the influence of continuous phase temperature on the droplet generation and solidification process, the wall temperature has no obvious effect on the size and frequency of generated LMPA droplets. However, it has a great effect on the temperature distribution and the process of droplet solidification in the microchannel. With the increase of wall temperature, the required time for droplet solidification gradually decreases.

Chapter 5 - The breakup and solidification of LMPA PCM droplet in microfluidic channel

The varying of LMPA liquid volume fraction with time in the microchannel under varying cooling wall temperatures was analysed when the Weber number We =43.51, and the oscillating frequency f= 2000 Hz. The breakup mechanism for LMPA-in-water system is dramatically different from that of water-in-oil system is observed, owing to the different viscosity ratio of continuous phase to dispersed phase, which is 103.96 for water-in-oil system, while 0.33 for LMPA-in-water system. Moreover, as the LMPA microparticles may lead to wide range of applications in food sciences, drug encapsulations and micro phase change materials, the influences of different Weber numbers and frequencies on the LMPA particle distribution are further analysed. The operating condition parameters are shown in Table 5.1.

Table 5-1 Operating conditions used in the LMPA-in-water system

Parameters	Values
Cooling wall temperature, T_C (K)	290, 295, 300, 305
Weber number	0.11, 0.44, 2.71, 10.87, 43.51, 174.04
Oscillation frequency, f (Hz)	30, 50, 100, 500, 1000, 2000

5.1. The effect of cooling wall temperature

The solidification process of the original LMPA droplet with a low Reynolds number at different cooling wall temperatures was analysed when We=43.51, and f=1000 Hz. Figure 5.1 shows the liquid volume fraction of LMPA phase varies with time under different wall cooling temperatures. Figure 5.2 shows the change of the total count of LMPA particles in the microchannel at $t = 3$ ms under different cooling wall temperatures. It can be seen that the total number of LMPA particles increases first and then decreases with the increases of cooling wall temperature, meanwhile, the largest diameter of formed LMPA particles first decreases and then increases with increasing cooling wall temperature, demonstrating that the size of daughter droplets can be tuned via control over the wall temperature. For example, if the temperature of the wall is sufficiently low and the solidification fraction is sufficiently large, no further droplet rupture happens resulting in larger daughter droplets. This holds for the higher temperature, when much smaller daughter droplets undergo coalescence. The required solidification time of LMPA droplet increases with the increase in cooling temperature, but solidification progress will be completed by $t = 3$ ms under the proposed cooling temperatures. The total number of LMPA particles decreases with the decrease of cooling wall temperature, which means that lowering cooling wall temperature can prevent the further rupture of LMPA particles. The LMPA particle diameter distribution in the microchannel varying with time is shown in Figure 5.3. With the increase of time, the diameter of the largest particles gradually decreases from 14 μm to 8 μm, and the peak diameter moves towards the small diameter direction. This is because the larger LMPA droplets break up into smaller ones due to the interaction with the continuous phase and wall during the breakup and their sizes remain unchanged during the solidification progress. Different sizes of LMPA particles can be subsequently collected by a filtration technique. Figure 5.4 illustrates the total count of LMPA

particles in the microchannel at different times, and the total number of LMPA particles can increase to about 210 at t=3ms.

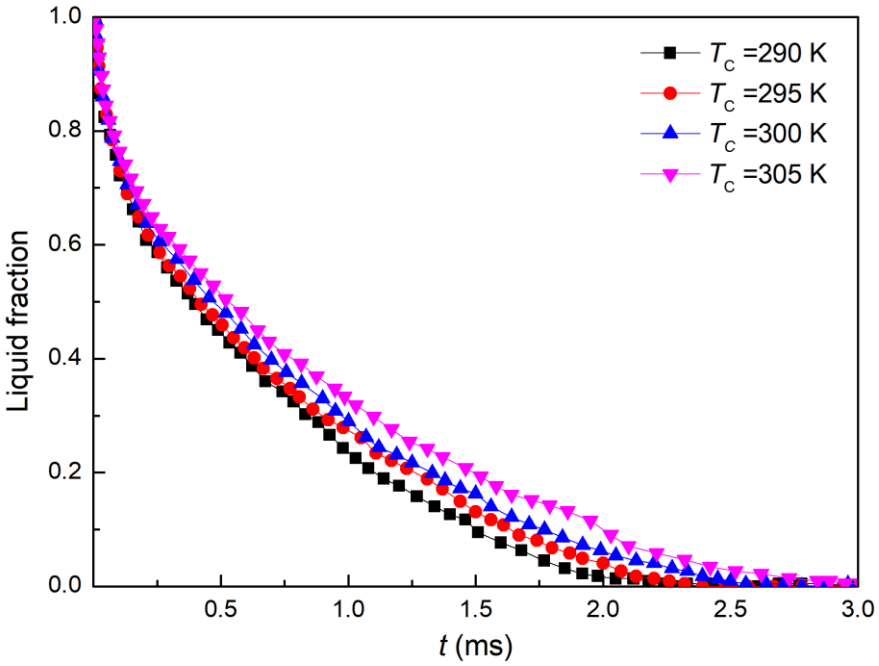

Figure 5-1 LMPA liquid volume fraction varies with time at different cooling temperatures, when *We*=43.51, and *f*=1000 Hz.

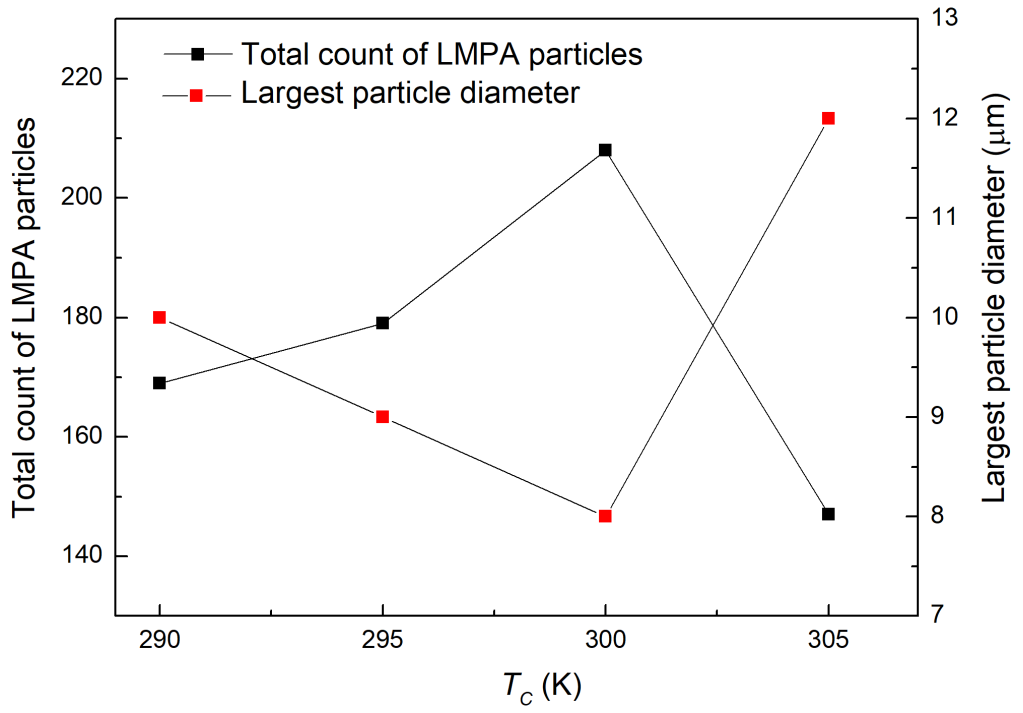

Figure 5-2 Effects of cooling wall temperature on the total count of LMPA particles and largest particle diameter at t=3 ms, when We= 43.51 and f= 1000 Hz.

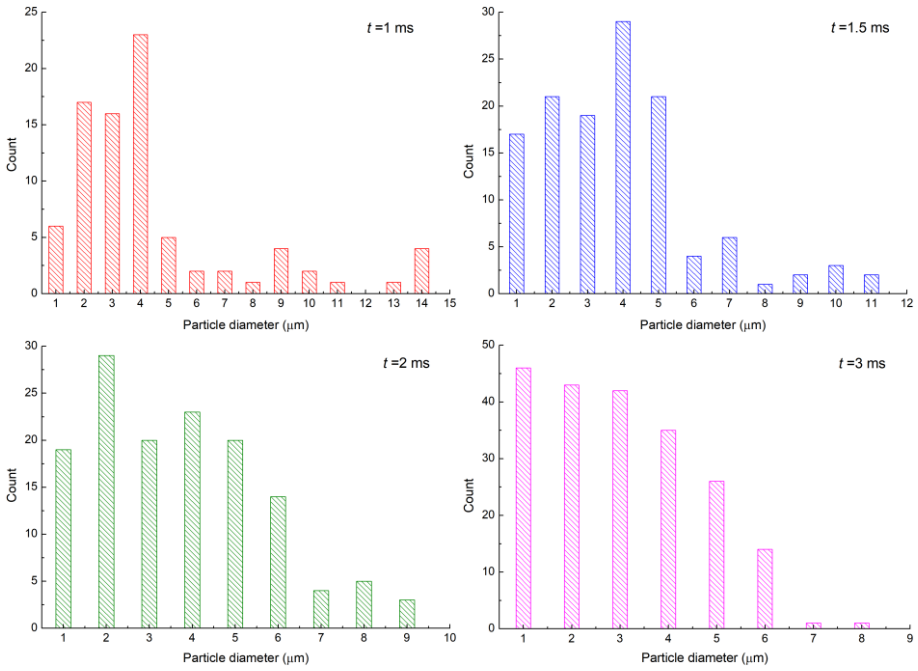

Figure 5-3 LMPA particle size distribution at different time, when *We*=43.51, *f*=1000 Hz, and T_c = 300 K.

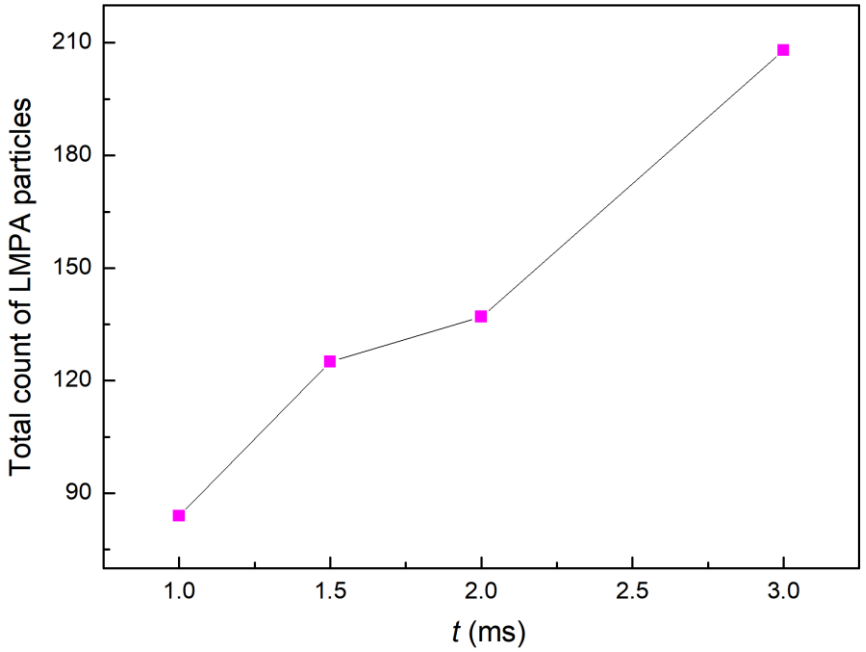

Figure 5-4 The total number of LMPA particles varies with time, when *We*=43.51, *f*=1000 Hz, and T_c = 300 K.

5.2. The effect of Weber number

It shows the LMPA particle size distribution under different Weber numbers when the velocity oscillating frequency is 2000 Hz and the cooling wall temperature is 300 K at $t = 3$ ms in Figure 5.5. The count of LMPA particles shows a downward trend with the increases in diameter size under certain velocity frequencies. The diameter of the largest particles gradually decreases from around 13 μm to around 7 μm when the Weber number increases from 2.71 to 174.04, and the number of particles with a diameter less than 7 μm in the microchannel increases, while the number of particles with a diameter greater than 7 decreases with the increase of Weber number, indicating that the droplets that remain unbroken at low Weber number will split into smaller particles at higher Weber number. This verifies our theoretical results that external disturbances help breaking droplets. Figure 5.6(a) shows the influence of Weber number on the total count of LMPA particles when the oscillation frequency is 2000 Hz and the cooling wall temperature is 300 K at t=3 ms. The total count of LMPA particles gradually increases to more than 100 as the Weber number increases from 0.11 to 174.04. It should be noted from inset in Figure 5.8(a), that when the Weber number is 0.11 to 0.44, the total count of LMPA particles remains one implying that the main droplet in the microchannel under these Weber numbers doesn't break up during the solidification. However, the LMPA droplet does deform under these Weber numbers as shown in Figure 5.6(b), indicating that there is a threshold breakup Weber number for droplet rupture, above which the LMPA droplet in the water phase will break. In this LMPA-water system, the threshold breakup Weber number is about 2.71 under given operating conditions.

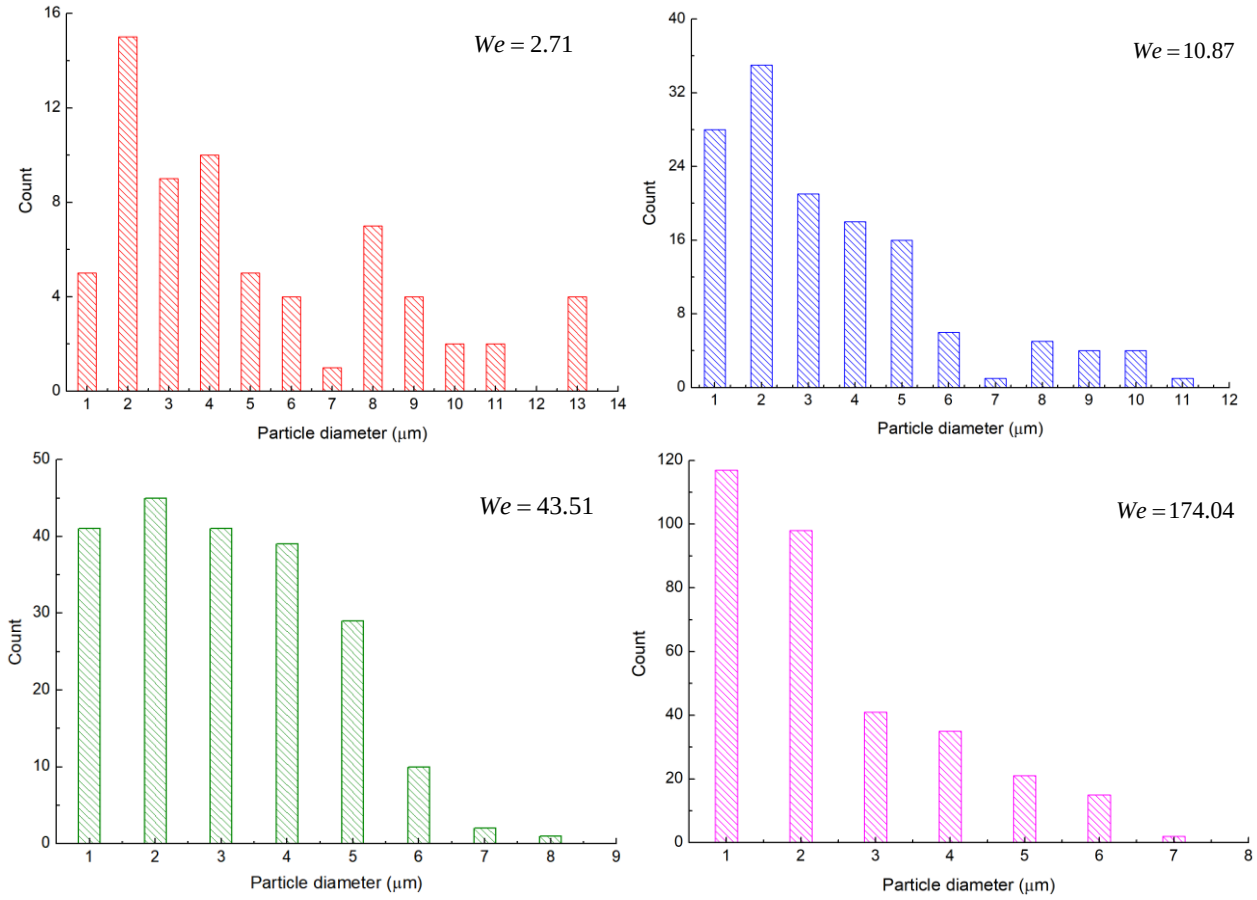

Figure 5-5 The influence of Weber number on LMPA particle size distribution at $t = 3$ ms, when f=2000 Hz, and T_c = 300 K.

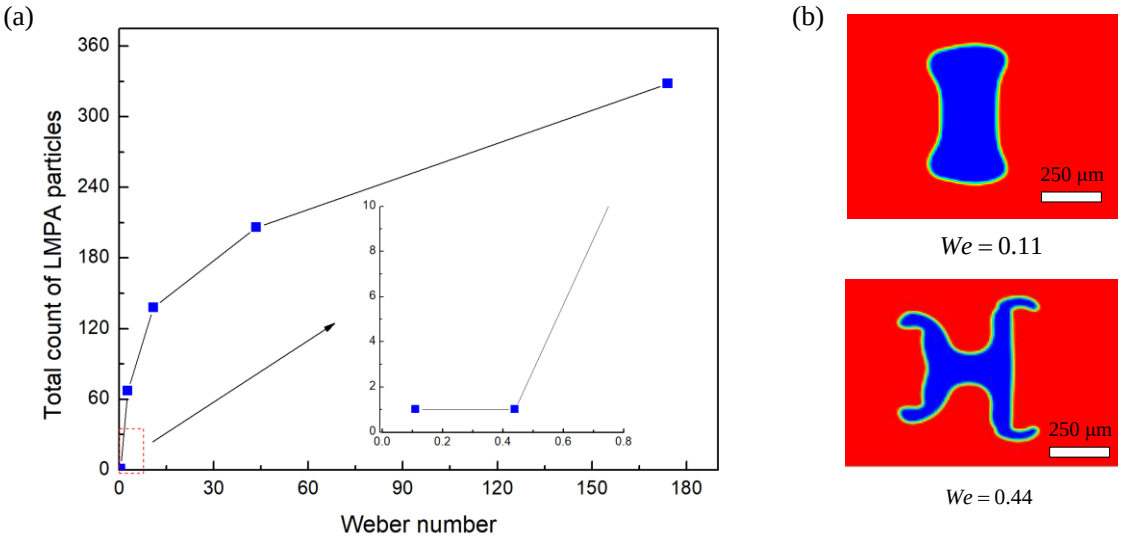

Figure 5-6 (a) Effect of the Weber number on the total number of LMPA particles at *t*=3ms, the oscillation frequency is 2000Hz, cooling wall temperature is 300 K; (b) The deformation of the LMPA particle when the Weber number is 0.11 and 0.44 at $t = 3$ ms, *f*=2000 Hz, and T_c = 300 K.

5.3. The effect of oscillation frequency

It shows the change of LMPA particle size distribution under different velocity frequencies when the Weber number is 2.71, the cooling wall temperature is 300 K in Figure 5.7. The microchannel contains more LMPA particles smaller than 4μm than that above 4 μm under the same frequencies. It also shows the prominent effect of perturbed flow frequencies on the LMPA particle size distribution. The diameter of the largest particles gradually decreases from about 44 μm at f=100 Hz to about 13 μm at f=2000 Hz, which indicates that LMPA particles with a larger diameter that remain unbroken at low oscillating frequencies will split into smaller particles at the higher velocity frequencies. This also verifies our theoretical results as given in Section 2. Figure 5.8(a) shows the influence of oscillating frequencies on the total number of LMPA particles when the

Weber number is 2.71 and the cooling wall temperature is 300 K at t=3 ms. It can be seen that the total count of LMPA particles gradually increases to about 65 as the oscillating frequency increases from 30 Hz to 2000 Hz. It is worth noting from inset in Figure 5.8(a), that when the frequency is 30 Hz or 50 Hz, the main droplet of the microchannel does not experience break up during the solidification process. However, the LMPA droplet deforms under these oscillating frequencies as shown in Figure 5.8(b) implying that there is a threshold disturbance frequency for droplet rupture, above which the droplet will break. This is also consistent with our theoretical results. The slight difference between theoretical and simulation results may be due to our neglect of viscosity in the theoretical part, while the simulation part takes into account the influence of viscosity. In the LMPA-in-water system, the threshold oscillating frequency is about 100 Hz for LMPA droplet breakup under given operating conditions.

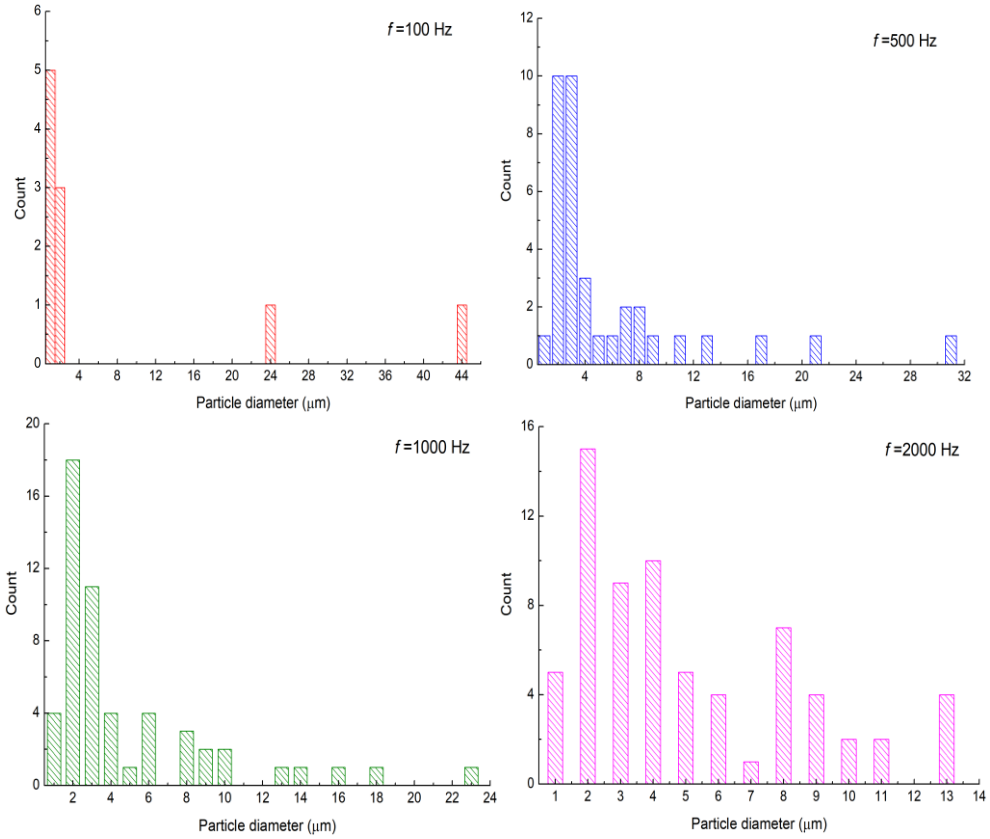

Figure 5-7 The influence of oscillating frequency on LMPA particle size distribution at $t = 3$ ms, when *We*= 2.71, and T_c= 300 K.

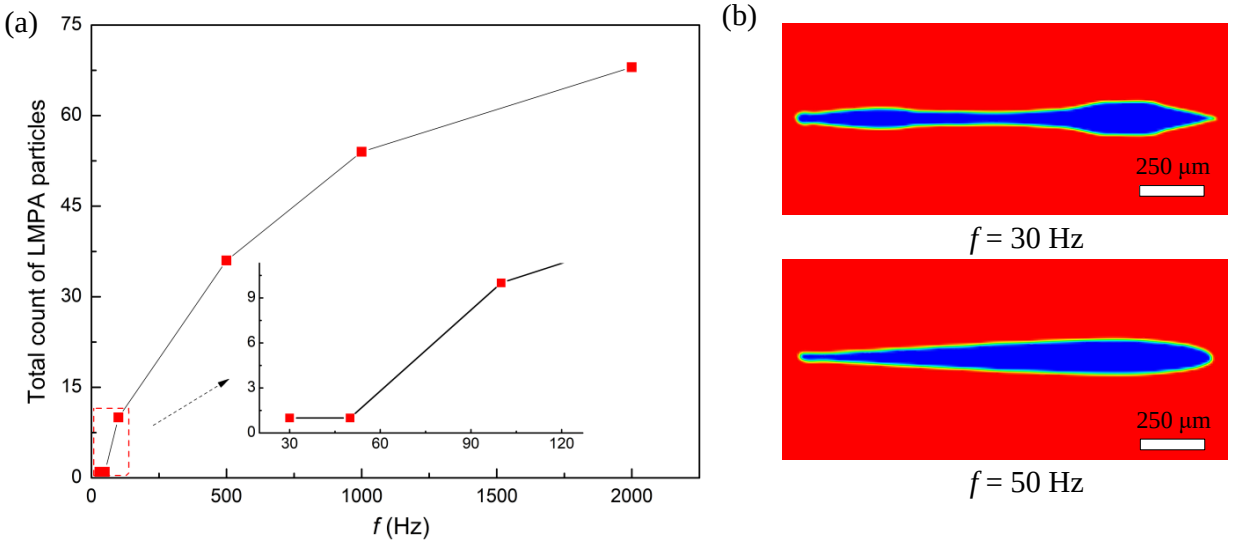

Figure 5-8 (a) The influence of oscillating frequency on the total number of LMPA particles at $t = 3$ ms when the Weber number is 2.71, cooling wall temperature is 300 K; (b) The deformation of the LMPA particle at $t = 3$ ms when the oscillating frequency is 30 Hz and 50 Hz, *We*= 2.71, and T_c= 300 K.

5.4. Summary

A type of multiphase flow in a microchannel has been investigated in the present study for investigating the droplet breakup dominated by oscillating flows. When the LMPA droplet is dispersed in the continuous phase of water, droplet breakup occurs when the Weber number is above 2.71, perturbation frequency is more than 100 Hz or Re is beyond 49.6. Decreasing the cooling wall temperature triggers the solidification progress and LMPA droplet, which can be completely solidified in 3 ms. However, decreasing the cooling wall temperature can hinder the further breakup of LMPA droplets during solidification processes. Increasing the Weber number makes the size of the largest LMPA particle decreases but increases the total number of LMPA particles concurrently. The LMPA droplets that remain unbroken at low Weber numbers will split into smaller droplets at higher Weber numbers. However, the LMPA droplet deforms under certain low Weber numbers. Increasing the oscillation frequency reduces the size of the largest LMPA particles, and increases the number of LMPA particles with small diameters and the total number of LMPA particles. The LMPA droplets with a larger diameter that remain unbroken at low velocity frequencies will split into smaller droplets at higher velocity frequencies. In summary, a novel approach for droplet breakup can be achieved in simple microchannel configurations driven by an oscillatory flow, and the current theoretical and

numerical results will guide designing appropriate microfluidic systems for the fabrication of LMPA microparticles with ultra-small size and well-tailored properties for energy and environmental applications.

Chapter 6 - Synthesis of Graphene/MEPCM based on microfluidic device

6.1. Double emulsion droplet formation in a microchannel

In comparing the droplet morphology of the double emulsion based on the geometry shown in Figure 6.1, the experimental results and simulation results are presented in Figure 6.1 [173]. The close agreement between the two validates the accuracy of the current numerical method in simulating the double emulsion's morphology. However, slight discrepancies exist due to the utilization of a two-dimensional domain in computation, while the experiment was three-dimensional. In Figure 6.1(a), the interfaces are closely spaced, making it difficult to distinguish the double emulsion. In Figure 6.1(b), the red color denotes the intermediate fluid separating the outer and inner fluids represented in blue. Figure 6.2 numerically shows the droplet formation under the certain condition, which can be a guidance for the experimentally study in the following part.

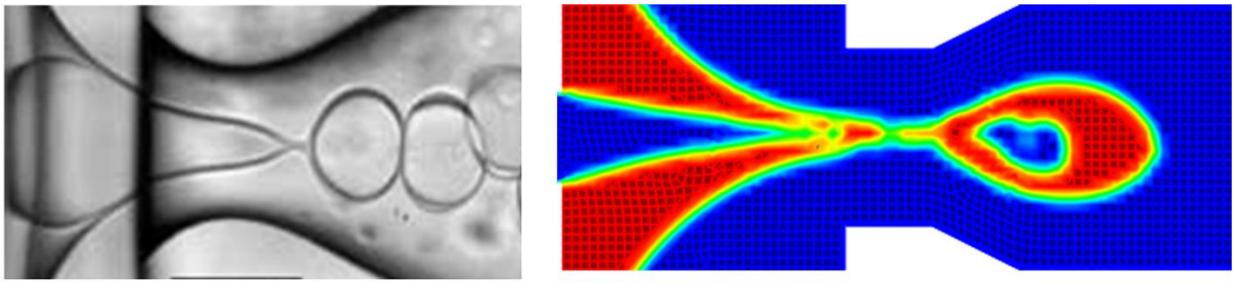

Figure 6-1 Experimental validation: (a) experimental image of double emulsion in dripping regime[173]; (b) the droplet formation simulated by numerical method.

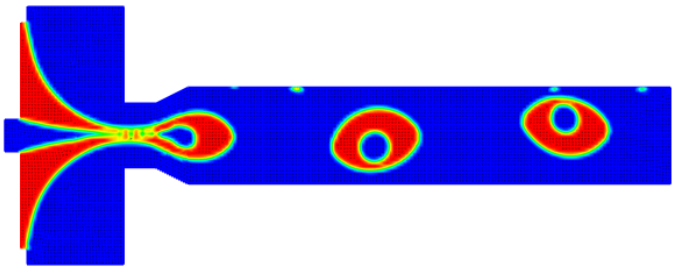

Figure 6-2 The variation of the double emulsion droplet under the condition U_m =0.009 m/s, Ui =0.009 m/s, Ui =0.025 m/s, μo =0.02 Pa· s, μ_m =0.02 Pa·s, μi =0.05 Pa·s. σ_o =0.03 N/m, σ_i =0.005 N/m.

6.2. Microfluidic fabrication of MEPCM and graphene modified MEPCM

The encapsulated droplet can be generated only when $\gamma_{i-o} > \gamma_{m-o} + \gamma_{i-m}$, in which γ_{i-o}, γ_{m-o} and γ_{i-m} are respectively the inner-outer interface, the middle-outer interface and the inner-middle interface. In this chapter, the formation of the microcapsules was examined by only changing the ratio of inner and middle flow rates, all the experiments were conducted under follow conditions: $Q_o = 400\ \mu L\ min^{-1}$ and $Q_m + Q_i = 45\ \mu L\ min^{-1}$, where the Q_o and Q_m are respectively the outer and middle flow rate. Figure 6.3(a) showed the formed double emulsion droplets at different Q_i/Q_m ratios, where the Q_i is the inner flow rate. Obviously, the obtained O/O/W droplets had regular structure as well as small relative size change in the MEPCM particles. Figure 6.3(b) showed the corresponding outer diameter (D_o), inner diameter (D_i) and shell thickness (T_s) of the O/O/W droplets. Evidently, by fixing the middle and outer flow rate, the average outer diameter increases while the shell thickness decreases with the increases of the Q_i/Q_m value. This is because the D_o only depends on the flow rate of Q_o and the sum of the $Q_i +$

Q_m for a certain microfluidic device. For an encapsulated droplet with a fixed D_o, the T_s and D_i are only determined by the value of the Q_i/Q_m. Figure 6.4 showed the optical microscope images of graphene modified MEPCM with different graphene content under $Q_i/Q_m = 4/5$. Figure 6.5 show the MEPCM and graphene/MEPCM particle with 2 wt% graphene.

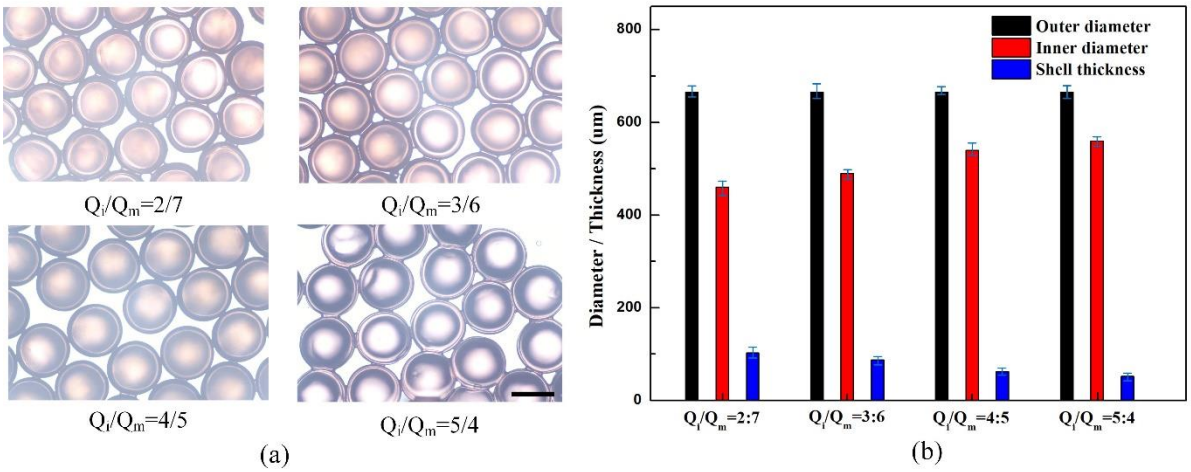

Figure 6-3 (a) Optical microscope images of the O/O/W droplets produced with a needle-based microfluidic device at different Q_i/Q_m, and (b) the corresponding outer diameter, inner diameter, shell thickness. Scale bars on (a) denote 500 μm.

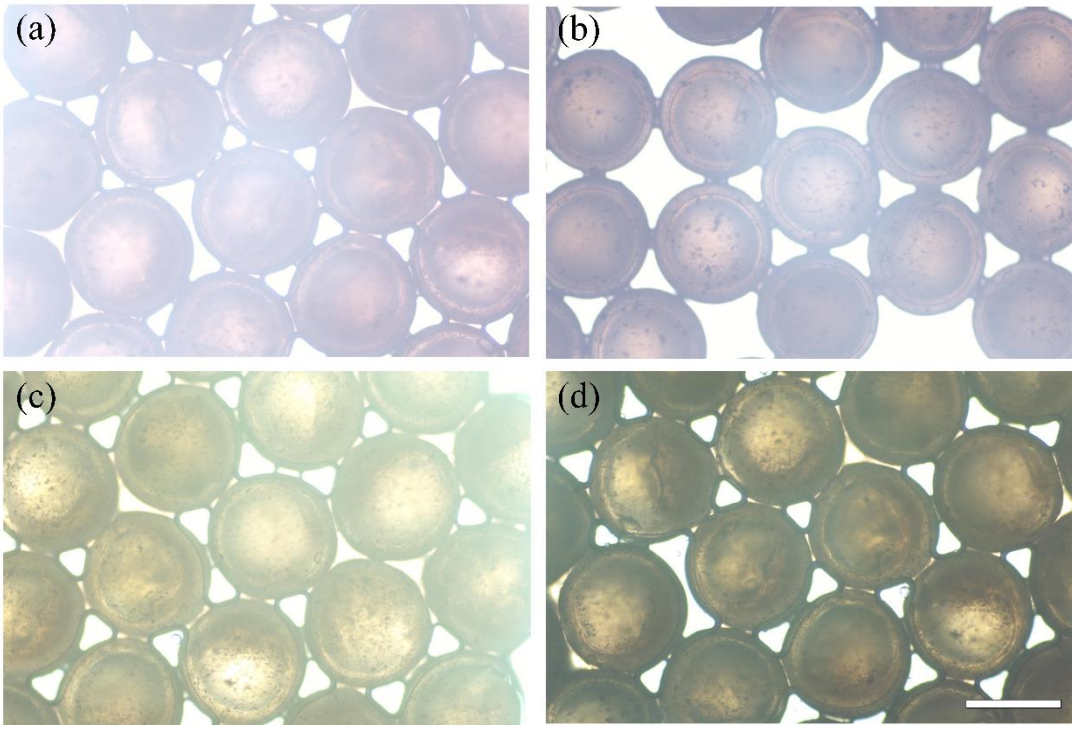

Figure 6-4 (a) Optical microscope images of the O/O/W droplets produced with a needle-based microfluidic device at different graphene content in the middle phase; (a) 0.5 wt% content; (b) 1 wt% content; (c) 1.5 wt% content and (d) 2 wt% content. Scale bars denote 500 μm.

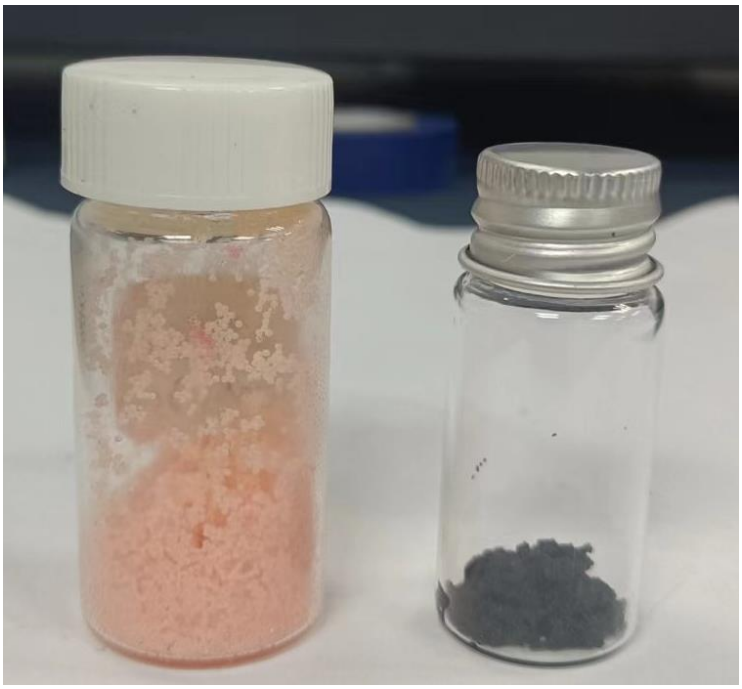

Figure 6-5 MEPCM and Graphene/MEPCM particle with 2 wt% of graphene.

6.3. Microstructure of the MEPCM and graphene/GO modified MEPCM

UV radiation curing was utilized to permanently fix the concentric structure of double-emulsion droplets through photopolymerization. This process allowed for the creation of microcapsules with a polymer shell. The sealing tightness and flexibility of the shell are crucial properties for numerous applications of microcapsules, and these attributes depend on the chemical structure of the shell itself. To achieve microcapsules with a smooth surface and excellent compactness, it is necessary to expose them to UV radiation for an adequate amount of time. Figure 6.6 displays the microstructure of these microcapsules, formed directly by employing double-emulsion droplets as templates. As evident from the image, the fabricated MEPCM microcapsules exhibit a regular spherical shape and possess a smooth surface. Importantly, they still preserve the symmetrical core-shell structure of the double-emulsion droplets. Comparing the double-emulsion droplets and

the final microcapsules, it was found that they have similar geometric dimensions. The differences in outer diameter, shell thickness, and core size between the two were less than 5% in this chapter. Figure 6.7 gives the SEM images of multilayer graphene, which clearly shows the multilayer structure. The SEM images of graphene/ MEPCM particles after UV curing, which haves been mechanically crushed core-shell microcapsules are shown in Figure 6.8. It is clearly shown the core-shell structure from the SEM image. Figure 6.9 gives SEM images of GO, and the Figure 6.11 shows the images of GO/ MEPCM particles after UV curing. From Figure 8(a), it can been seen that the microcapsule is not as smooth as the MEPCM without GO. This is because the addition of GO, which affect the surface structure of the microcapsules, as clearly shown in Figure 6.10.

These observations indicate that UV radiation curing is an effective method for transforming double-emulsion droplets into microcapsules via high-rate polymerization, without causing any significant changes in their size and structure.

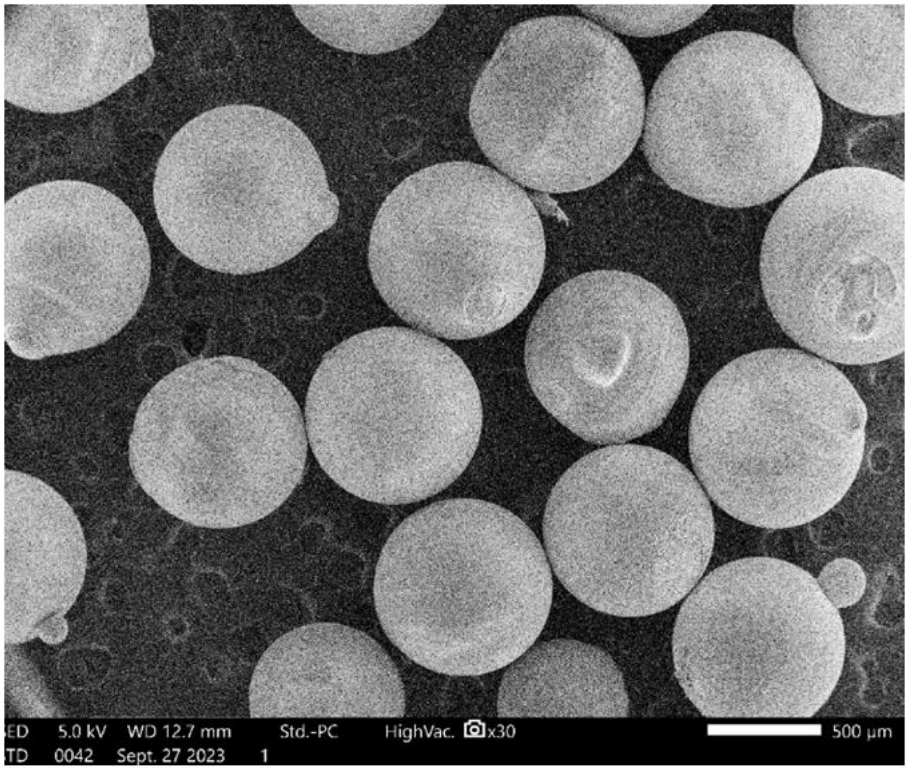

Figure 6-6 SEM images of MEPCM particles after UV curing.

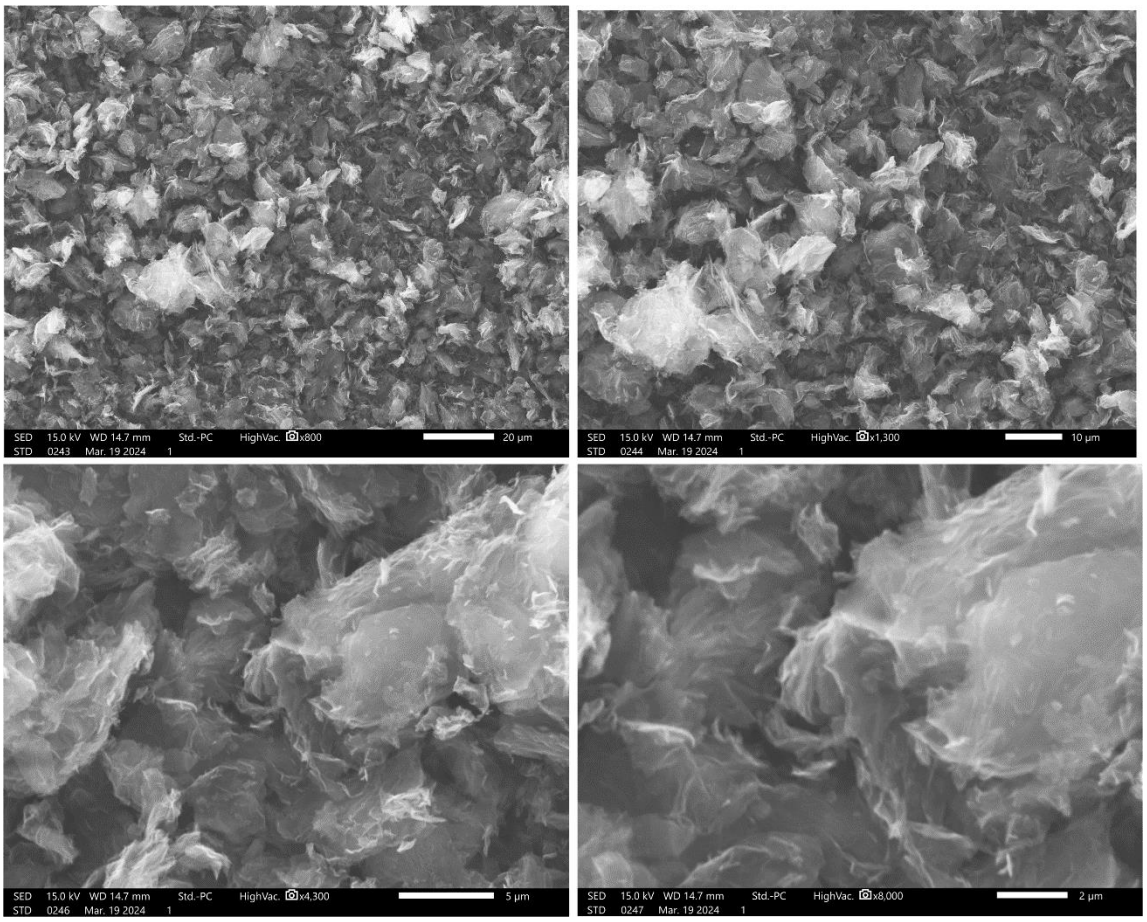

Figure 6-7 SEM images of multilayer graphene

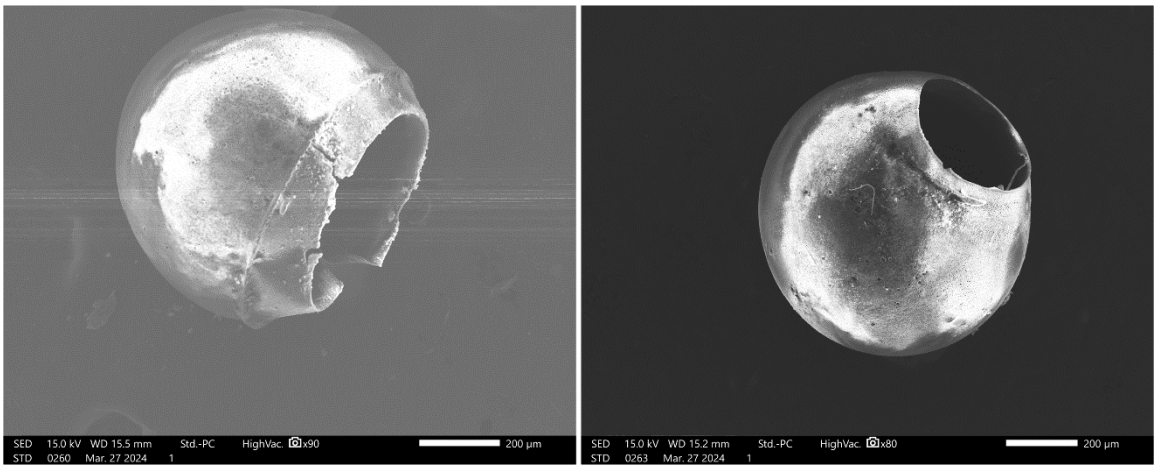

Figure 6-8 SEM images of graphene/ MEPCM particles after UV curing; Mechanically crushed core-shell microcapsules.

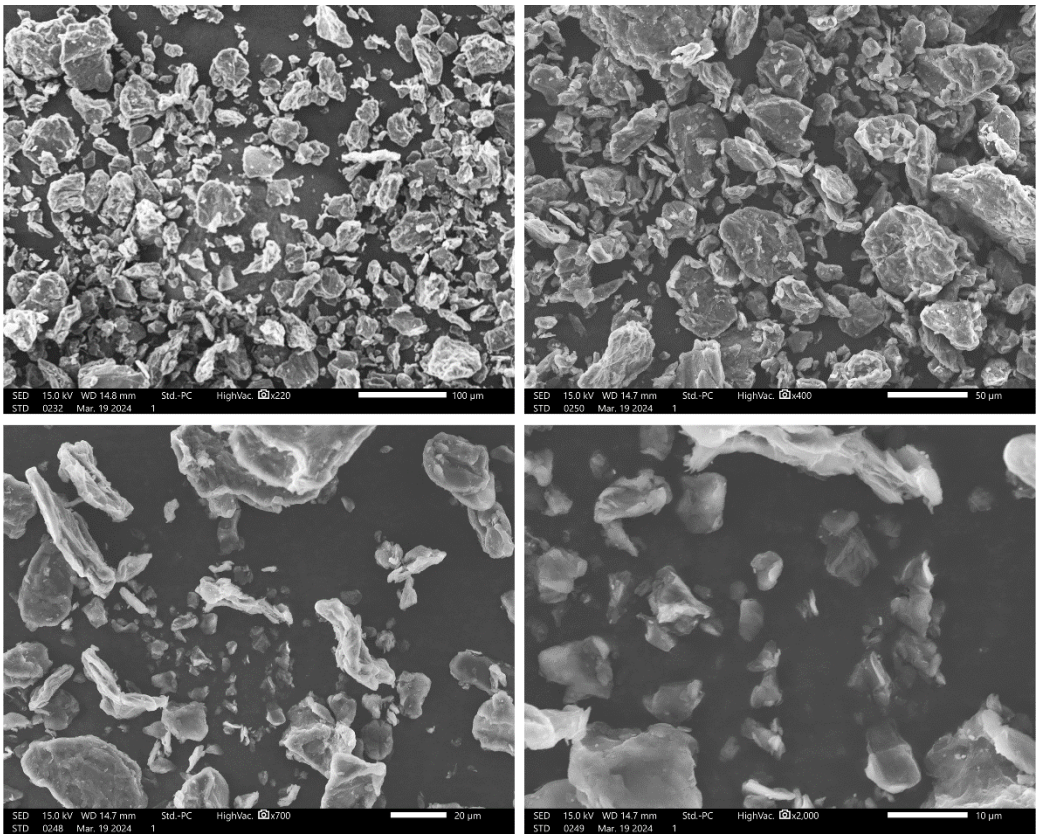

Figure 6-9 SEM images of GO.

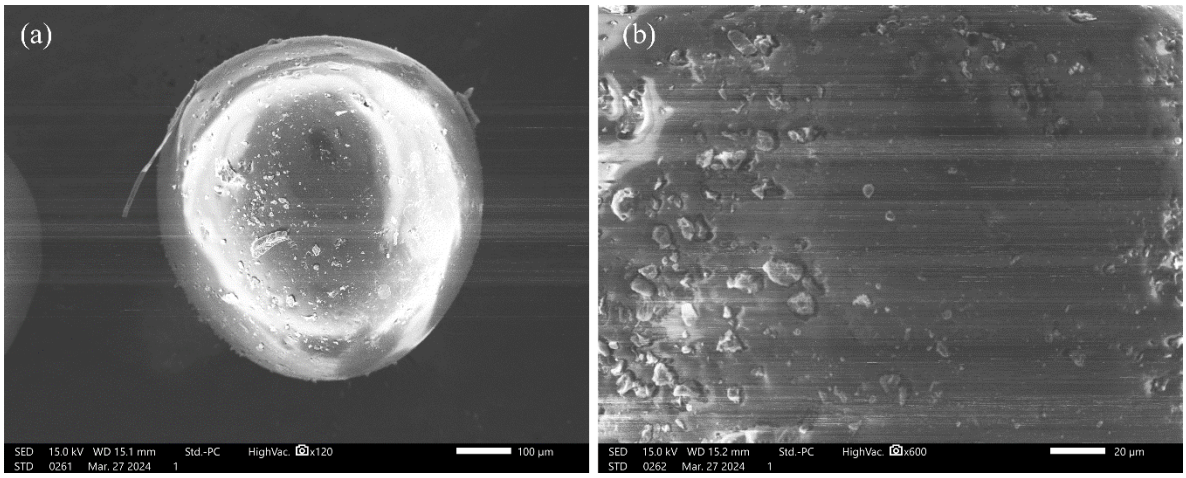

Figure 6-10 SEM images of GO/ MEPCM particles after UV curing.

6.4. Size distribution of graphene/MECPM

Size monodispersity is an important indicator for evaluating graphene modified microcapsules prepared by a combination of UV curing and microfluidic methods. As shown in Figure 6.11, the particle size distribution under the condition of $Q_o = 400$ μL min^{-1}, $Q_m = 25$ μL min^{-1}, $Q_i = 20$ μL min^{-1} and 1 wt% graphene content indicates that the microcapsules have a narrow range of size distribution. The size change is about 30 μm. The relative size change in the MEPCM particles is approximately 5.5%. Through repeated experiments, the maximum value of coefficient of size variation was confirmed under different Q_i/Q_m is less than 6%, which proves that the combination of radiation curing and needle based microfluidic methods can obtain dual functional microcapsules with good monodispersity and high uniformity.

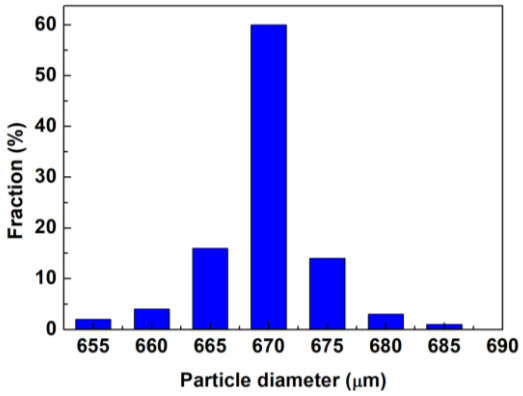

Figure 6-11 Particle size distribution of microcapsules.

6.5. Thermal properties of MEPCM and graphene/MEPCM

The thermal storage performance of MEPCM microcapsules can be obtained through DSC analysis. Figure 6.12 shows the freezing and melting DSC curves of microcapsules prepared with pure n-hexadecane and an internal and middle phase flow rate ratio of 5/4. Due to the fact that only n-hexadecane undergoes phase transition in the range of -40 ° C to 40 ° C, the microcapsules of HDDA shells can undoubtedly absorb and release less heat energy compared to pure n-hexadecane.

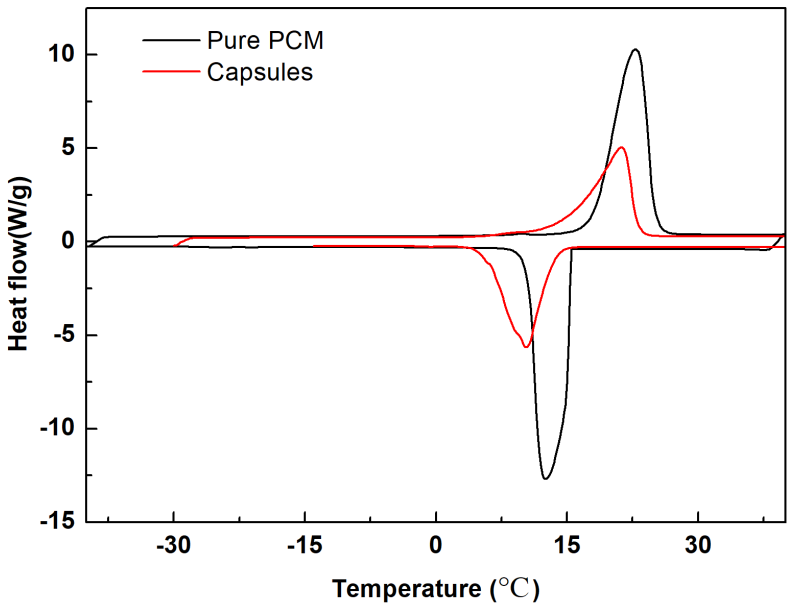

Figure 6-12 DSC curves of pure n-hexadecane and graphene/MEPCM microcapsules with a flow rate ratio of 5/4 between the inner and middle phases.

Table 6.1 shows that the melting enthalpy and freezing enthalpy of pure n-hexadecane are 272.90 and 268.93 kJ/kg, respectively. When Q_i/Q_m equals 2/7, 3/6, 4/5, and 5/4, the ΔH_f of microcapsules is 92.49, 113.78, 138.41, and 153.29 kJ/kg respectively, with corresponding ΔH_m are 102.42, 126.26, 147.93, and 164.25 kJ/kg, respectively. The encapsulation efficiency (W) and energy storage efficiency (E) of microcapsules could be obtained by the following formula [24, 25]:

$$\mathrm{W} = \frac{\left|\Delta H_{f-MEPCM}\right|}{\left|\Delta H_{f-PCM}\right|} \times 100\% \tag{6.1}$$

$$\mathrm{E} = \frac{\left|\Delta H_{m-MEPCM}\right| + \left|\Delta H_{f-MEPCM}\right|}{\left|\Delta H_{m-PCM}\right| + \left|\Delta H_{f-PCM}\right|} \times 100\% \tag{6.2}$$

Table 6-1 Thermal properties of the fabricated MEPCM microcapsules.

Q_i/Q_m	ΔH_f(kJ/kg)	ΔH_m(kJ/kg)	W(%)	E(%)
Pure PCM	268.93	272.90	-	-
2/7	92.49	102.42	34.39	35.97
3/6	113.78	126.26	42.31	44.30
4/5	138.41	147.93	51.47	52.85
5/4	153.29	164.25	57.00	58.61

It was found that the difference between encapsulation efficiency and energy storage efficiency of microcapsules is very small at each flow rate. The variation between them is less than 5%, suggesting that most of the latent heat could be absorbed and released by the PCM during phase transition. It also illustrated that almost all n-hexadecane molecules are successfully encapsulated by the shell material, and basically all n-hexadecane in the microcapsules can effectively store and release latent heat during the phase transition period [24, 25]. The above results showed that microcapsules prepared by microfluidic and UV radiation curing could be well used in latent heat storage systems.

The DSC analysis was utilized to determine the latent heat of the graphene/MEPCM microcapsules, as detailed in Table 6.2. The microcapsules, containing various mass ratios of multilayer graphene, underwent repeated phase-change processes during the experiment. Figures 6.13 and 6.14 visually

depict a basically unchanged in the proportion of PCM within the microcapsules as the mass ratio of multilayer graphene increased from 0 to 2 wt%. This suggests that addition of graphene to the microcapsules does not affect the phase-change enthalpy.

Table 6-2 Thermal properties of the fabricated Graphene/MEPCM microcapsules with different graphene content.

Mass ratio of graphene	ΔH_f(kJ/kg)	ΔH_m(kJ/kg)	W(%)	E(%)
0 wt%	153.29	164.25	57.00	58.61
0.5 wt%	153.12	164.22	56.94	58.57
1 wt%	153.25	164.65	56.99	58.67
1.5 wt%	153.87	164.74	57.22	58.80
2 wt%	153.65	164.42	57.13	58.70

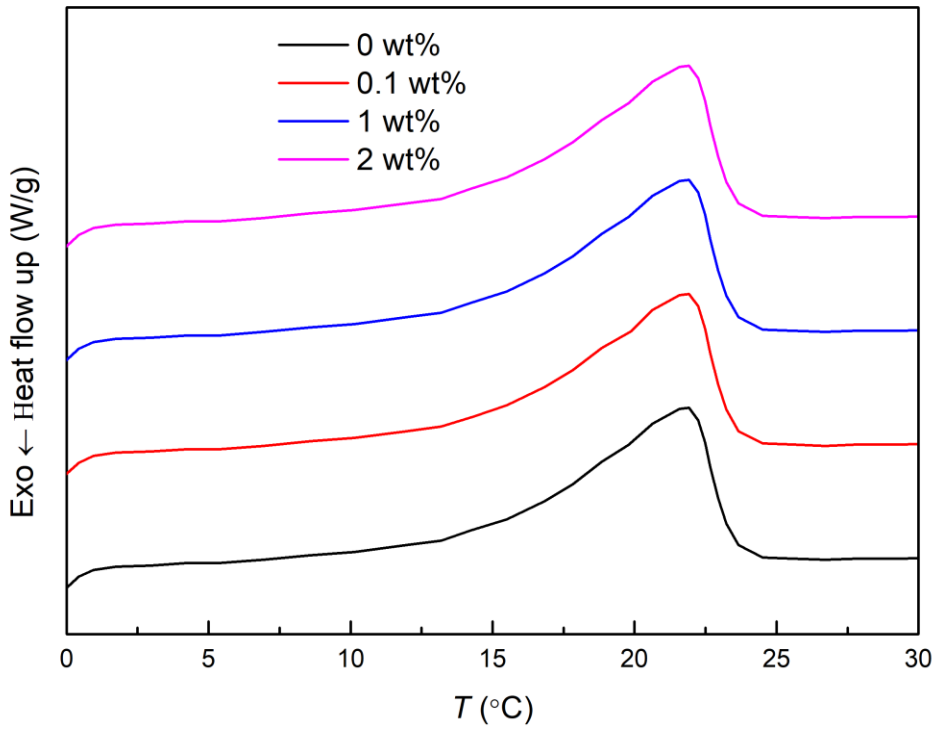

Figure 6-13 (a) DSC thermographs of PCM microcapsules: melting peaks

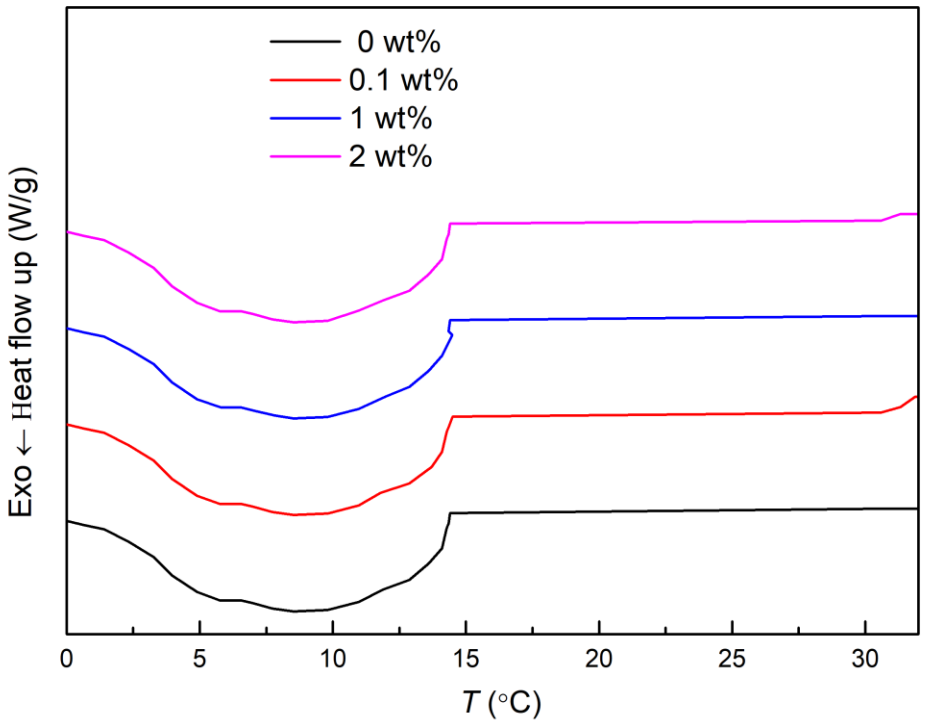

Figure 6-14 DSC thermographs of PCM microcapsules: solidification peaks

To illustrate the enhancement of heat conductivity achieved by incorporating multilayer graphene, the thermal conductivities of PCM microcapsules with varying mass ratios of multilayer graphene were evaluated using the transient plane source method with a conductometer. In this experimental setup, the PCM microcapsules, including their core and shell, were crushed to form a simple plane for testing. The thermal conductivities of the microcapsules in both solidified and molten states were measured. Figure 6.15 shows that as the mass ratio of multilayer graphene increased from 0.1 to 2 wt%, there was a noticeable improvement in heat conductivity, highlighting the contribution of multilayer graphene to enhancing heat transfer within the PCM microcapsules.

Overall, these results demonstrate that the PCM microcapsules exhibit satisfactory heat transfer performance during the phase-change process.

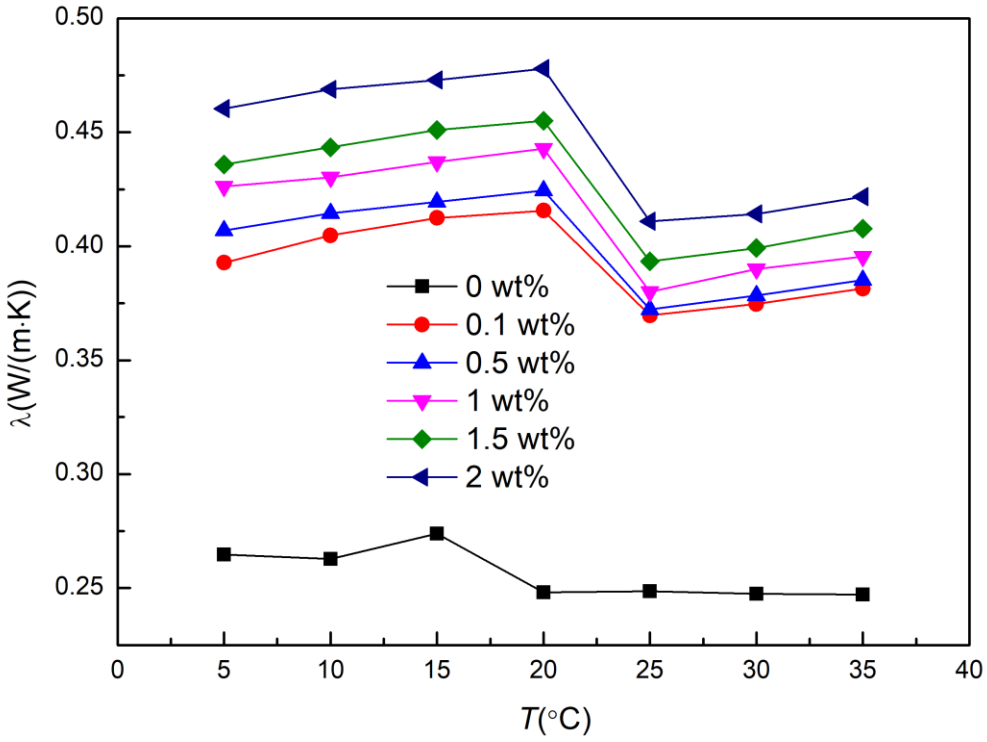

Figure 6-15 Thermal conductivity of the graphene/MEPCM microcapsules with different graphene content versus temperature. The tested microcapsules are prepared under the typical condition of a flow rate ratio of 5/4 between the inner and middle phases.

6.6. Thermal stability of graphene/MEPCM

The thermal stability of microcapsules plays a crucial role in determining their practical applications and is closely linked to the quality of the microcapsule shell. To evaluate this, the study conducted TG analysis and thermal cycling durability tests on the graphene/MEPCM

microcapsules. Figure 6.16 presents the TG curves of three substances: pure n-heptadecane, pure HDDA, and graphene modified MEPCM with HDDA and graphene as the shell. As the temperature increases, the weight of all three substances decreases. Pure n-heptadecane starts losing weight at approximately 68.4 °C and continues to do so until the temperature reaches 236.2 °C, at which point it has completely evaporated. Notably, the decomposition temperature of pure n-heptadecane is lower than its boiling temperature of 292 °C, indicating that the substance volatilizes before reaching boiling point. In contrast, the weight loss rate of microcapsules with a graphene/HDDA shell is significantly lower than that of pure n-heptadecane. The thermal decomposition of the microcapsules with HDDA shell is essentially completed around 480 °C. Additionally, the 5% weight-loss temperatures (also known as thermal resistant temperatures) of the microcapsules with an HDDA shell are approximately 124.3 °C. These observations suggest that the HDDA polymer shell effectively protects the n-heptadecane from leaking or rapidly volatilizing. In summary, the TG analysis and thermal cycling durability tests indicate that microcapsules with an HDDA shell exhibit improved thermal stability compared to pure n-heptadecane. The HDDA polymer shell acts as a protective barrier, preventing the substance from leaking or evaporating quickly.

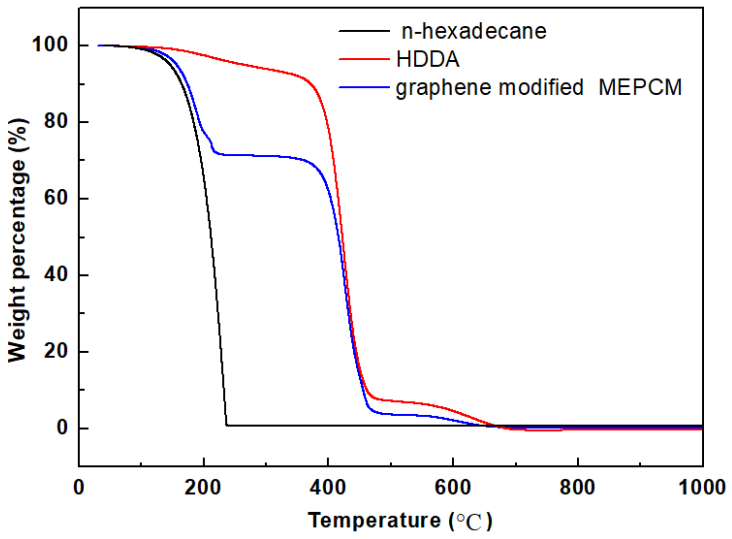

Figure 6-16 TG curves of pure n-heptadecane, HDDA and MECPM with graphene/HDDA shell.

6.7. Mechanical strength of graphene modified MEPCM

The mechanical strength of microcapsules was measured using a Haake RheoStress 6000 rotary rheometer, with a parallel plate titanium alloy rotor P60 TiL, and the experimental temperature was 25.0 ± 0.1 ℃. The mechanical strength is determined through compression testing: specifically, a single microcapsule are laid flat on parallel plates with an initial gap of 1mm, and compressed at a speed of 0.01 mm/s. The normal stress value during the compression process is also collected. As can be seen in Figure 6.17, when the inner and middle phase are 20 μl/min and 25 μl/min respectively, the wall thickness of the microcapsules is relatively thin, and the final spacing is about 75 μm, corresponding to a larger stress value of 50.02 N. On the contrary, for changes in inner/middle flow rate as 15/30 μl/min, the wall thickness of the microcapsules increases, and the corresponding final spacing also slightly increases (100 μm), while the stress value is slightly smaller at 49 N. Based on

the above analysis, it is concluded that the mechanical strength can be enhanced with the increase of shell thickness of the microcapsules.

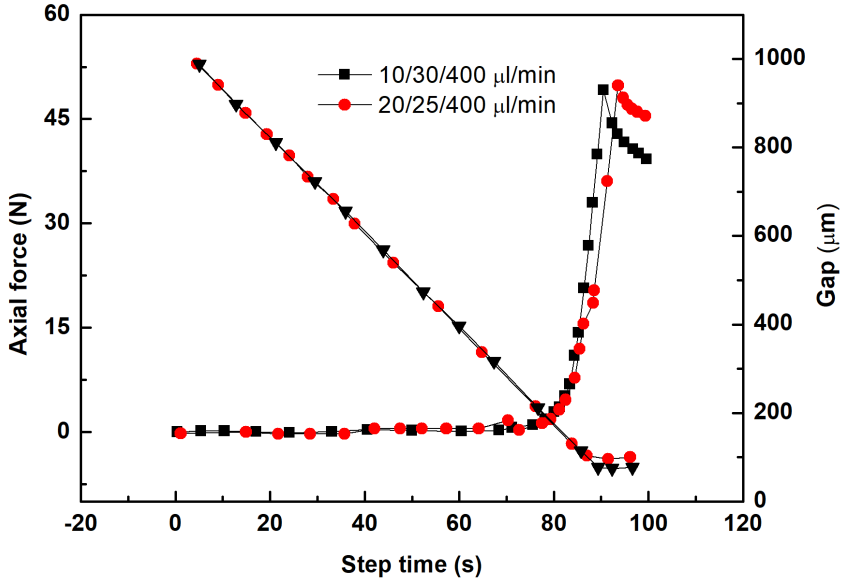

Figure 6-17 Axial force and gap with different flow rate.

6.8. Summary

By combining needle-based microfluidics with UV radiation curing, MEPCM and graphene/GO enhanced MEPCMs with controllable structure and size were rapidly prepared with n-hexadecane as the core. By changing the inner flow rate, the outer diameter, inner diameter and shell thickness of the microcapsules can be easily adjusted. In this chapter, spherical MEPCM and graphene/GO enhanced MEPCMs with smooth surface and small relative size change in the MEPCM particles (under 5%) were successfully prepared and these MEPCMs showed good thermal storage and release energy capacity. Besides, the HDDA shell was proved to have good mechanical property to withstand the volume change caused by the core material during phase transformation. After the

80th thermal cycle, no fractured MEPCM was observed, illustrating excellent thermal cycle stability. In conclusion, this chapter offers valuable guidance for the preparation of MEPCMs with good thermal properties. The addition of graphene to the microcapsules does not affect the phase-change enthalpy. As the mass ratio of graphene increased from 0.1 to 2 wt%, a remarkable enhancement in heat conductivity was observed, underscoring the significant role of multilayer graphene in improving heat transfer within the PCM microcapsules.

Chapter 7 - Microchannel heat sink improvement based on novel design and graphene enhanced MECPM

7.1. Material selection for heat sink

In this section, the influence of heat sink material on the heat transfer performance of the microchannel will be examined. Here, the un-finned microchannel was used to evaluate the MCHS performance with different heat sink materials. Figure 7.1 illustrates the effect of the four different heat sink materials on the Nu number at Re=600. It is shown that different heat sink materials have little effect on the Nu value, which means that the material of heat sink is not as much significant to the heat transfer performance. Silicon as the material for microchannel heat sink achieved the highest Nu number of 12.17 while silver had the least one of 11.98. Besides, experimental studies on the fabrication of microchannel heat sinks have shown that it is effective and feasible for achieving good thermal performance when choosing silicon as microchannel and micro-fins materials, which could be fabricated by laser micromachining [174] or deep reactive ion etching [175-177]. For this reason, silicon was selected as the material for the next investigation of this chapter.

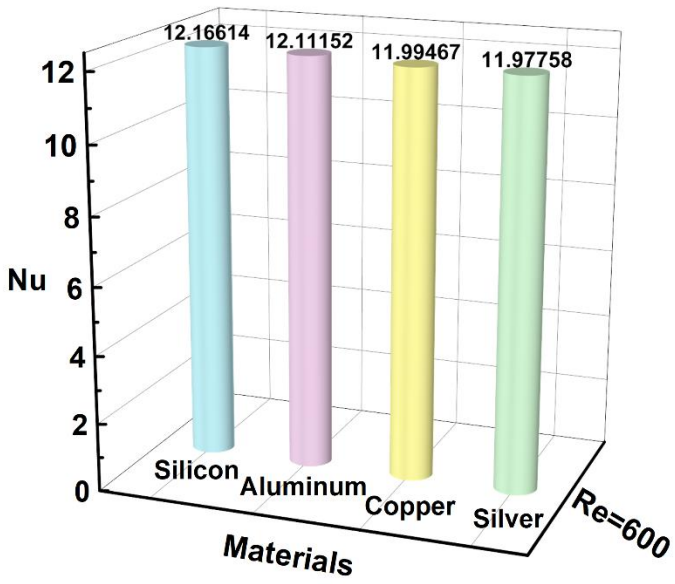

Figure 7-1 Comparison of Nusselt number when using silicon, aluminum, copper, or silver as heat sink at Re=600.

7.2. The effect of different arrangements of micro pin-fins

This section focused on how the three geometrical structures, Structure A, B and C influences the thermal and hydraulic performance of MCHS. The circular shaped micro pin-fin geometry with 0.9 mm spacing was applied to the three geometrical structures for this investigation. Figure 7.2 shows the velocity contour plots for the MCHS without pin-fins and structure C for Re = 600. It can be observed that the pin-fins created a disturbance in the boundary layer as well secondary flows. Additionally, the inclusion of pin-fins in the straight microchannels led to the generation of vortex shedding, effectively enhancing the heat transfer coefficient. It is worth noting that previous studies have also documented the occurrence of vortex shedding in MCHS with pin-fins [178].

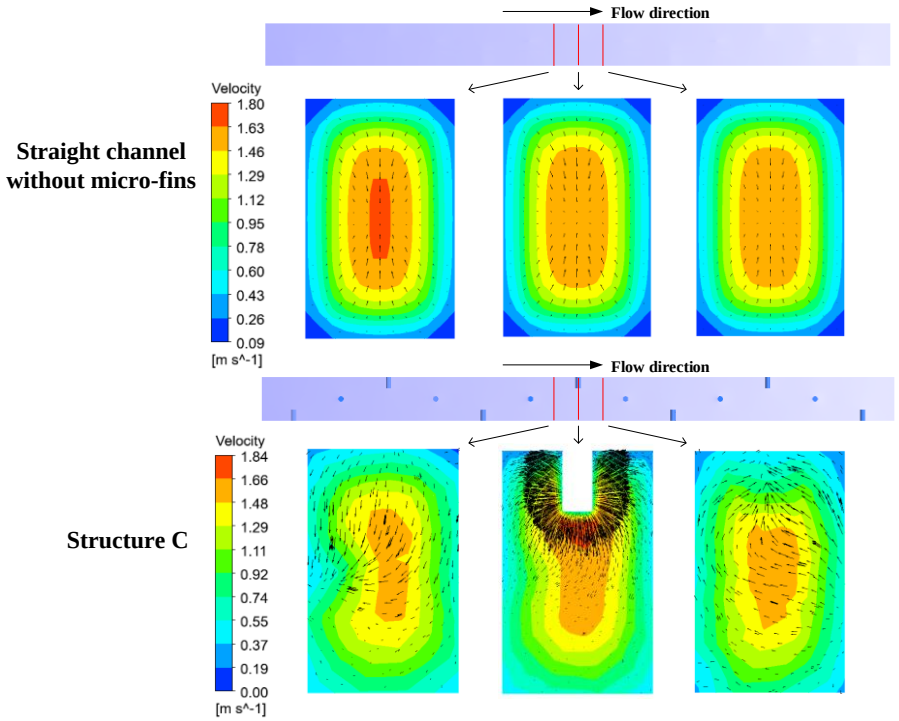

Figure 7-2 Velocity plot (contoure+vector) at different positions in the microchannel without micro-fins and the microchannel with structure C.

Pressure drop occurs when fluid flows through the microchannels as it encounters some resistance caused by friction and disruption [48]. Thus, studying pressure drop is necessary for forced convection heat transfer to estimate the pumping power needed to make the MCHS work properly. It can be observed Figure 7.3(a) that the pressure drop increases with the increases of Re for all arrangements. The pressure drop for unfinned MCHS always remains the lowest in the entire range of Re. Specifically, the pressure drop for Structure B and C is 47% higher than unfinned structure at Re=1000. The reason is that adding pin-fins reduces the total volume of working fluid, which encounters the disruption, resulting increasing velocity and larger pressure drop. Besides, local vortices would be generated behind pin-fins thereby increasing the inlet pressure. Figure 7.3(a) also illustrates that a conventional MCHS exhibits the highest overall thermal

resistance compared to the modified MCHS designs. The total thermal resistance of structure A, B and C decreased by an average of 17.04%, 32.85%, and 33.88% respectively, when compared to a typical MCHS at Re=1000. Figure 7.3(b) illustrates the variation of dimensionless outlet temperature T' and with Re for different arrangements of MCHS. It can be seen the difference of T' for Structure A, B and C are negligible for all Re. Figure 7.3(b) also displays the Nu for all of the four types of MCHS rise with an increases of Re, but the growth rate become a little smaller. Obviously, increasing Re leads to high coolant velocity and mass flow rate, resulting more heat transfer. Besides, it should be noted that the Nu for Structure A was observed to be 51.1% larger than unfinned structure. The best performance of Structure C was found at Re=1000, where the value of Nu was observed to be 59.9% larger than unfinned structure. The significant heat transfer results from the heat transfer surface area (Ac) and the micro-fins were capable of disrupting and reforming boundary layers, which in turn promoted the formation of vortices. This resulted in increased mixing of the flow within a channel.

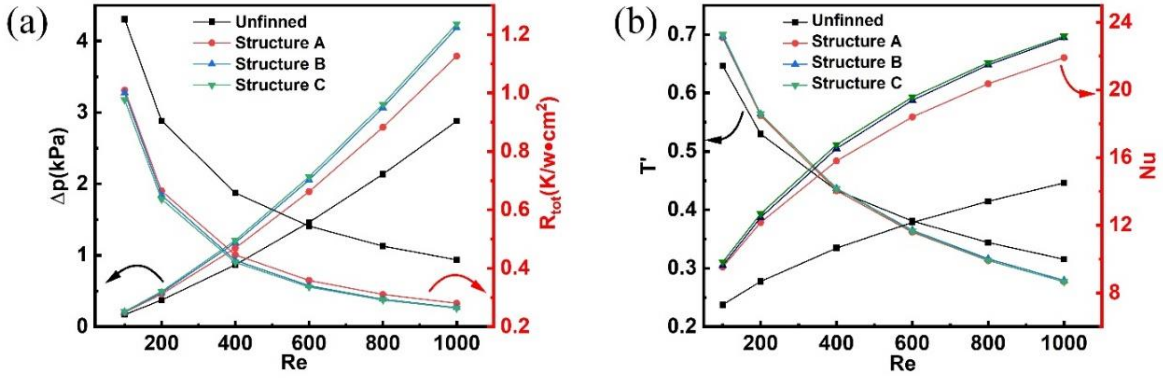

Figure 7-3 Effect of arrangements of micro pin-fins on (a) pressure drop and the total thermal resistance, (b) dimensionless temperature hoist at the exit and Nu for different arrangements of MCHS.

In order to compare the overall thermal and dynamic performance of microchannels with different geometric arrangements (Structure A, B and C), PEC were studied as a measure of heat transfer enhancement due to increased pressure drop. PEC greater than 1 means that heat transfer enhancement is greater than the pressure drop increased by applying micro pin fin structures. As shown in the Figure 7.4, with the increase of Re, the PEC of all microchannel structures first increases, reaches a certain value, and then decreases. This indicates that for different geometric structure distributions, there exists the same optimal flow rate Re=600, which maximizes the overall performance of the system. In the entire Re region under consideration, structure C has the highest PEC value. Specifically, the PEC of structure B and structure C is much higher than that of structure A within the range of $400 \leq \mathrm{Re} \leq 1000$, while it's slightly higher than structure B and the PEC can be up to 1.43 when Re=600. It should be noted that the PEC variation between structure B and C gradually decreases with Re, becoming zero when Re=1000, which means that compared to structure B, the advantage of structure C becomes less and less obvious with the increase of Re, but it is still the optimal structure within the considered Re range.

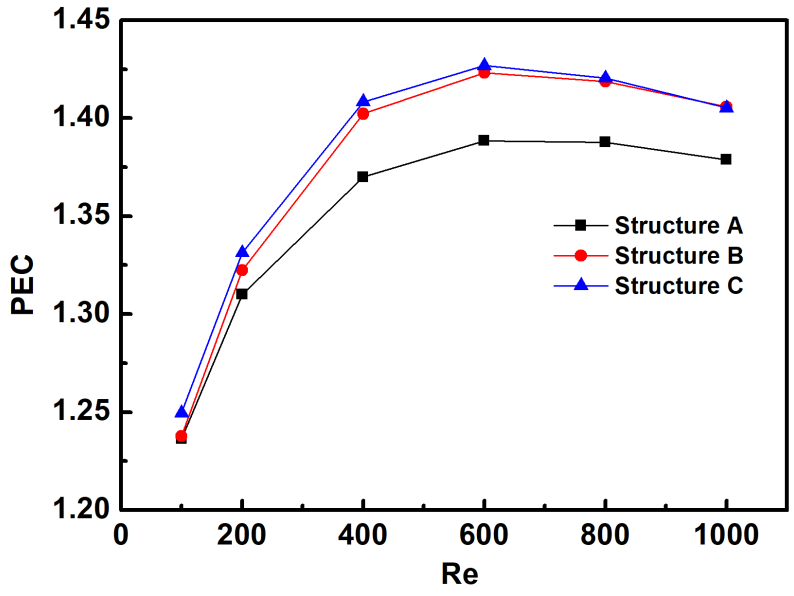

Figure 7-4 Effect of arrangements of micro pin-fins on PEC.

7.3. The effect of geometry of micro pin-fins

This section aims to determine the most effective shape of micro pin-fins to improve the heat transfer. It is evident from Figure 7.5(a) that the rise in Re results in an increase in pressure drop, but the rate of increase is dependent on the geometry of the micro pin-fins. While there is a trivial variation in pressure drops of micro pin-fins with different cross-sectional geometries at low Res, the differences become more pronounced at higher Res. The triangular cross-section pin fins portray the largest pressure drop, exceeding 5000 Pa at Re=1000, whereas the elliptical cross-sectional pin fin had the smallest pressure drop, approximately 4000 Pa at Re=1000. The reason for this can be explained by the fact that triangular pin-fin produces a larger adverse pressure gradient than the other shapes. Figure 7.5(a) also shows that the geometric shape has little effect on the thermal resistance. Figure 7.5(b) depicts that all geometries exhibited a negative relationship between T' and Re. The T' of micro pin fin with circular and elliptical sections displayed similar values and gradients, while square, triangular, and hexagonal shaped cross-sections also exhibited nearly identical values and gradients. It's also observed in Figure 7.5(b) that the Nu increases with increasing Re for the micro shape considered. The MCHS with circular shaped micro pin-fin has the highest Nu when Re was between 100 and 600, while Nu with triangular shaped pin-fin surpasses that of circular shaped fin when Re>600. It can be attributed to the ability of triangular and circular pin fins to generate wake at the trailing edge, promoting fluid mixing and consequently increasing the heat transfer performance.

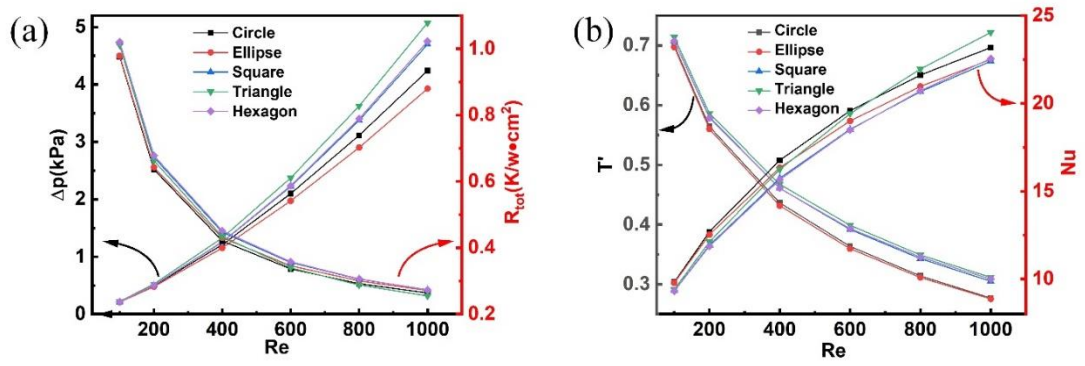

Figure 7-5 Effect of different geometry of MCHS on (a) pressure drop and the total thermal resistance, (b) dimensionless outlet temperature and Nu.

The comparison of PECs for different micro pin fin shapes is shown in Figure 7.6. Within the considered range of Re numbers, except for the triangle shape, which PEC continuously increases, the PECs for all other shapes initially increases within the range of $100 \leq \text{Re} \leq 600$, and then decreases after reaching its maximum at Re=600. This indicates the presence of a common optimum Re=600, where the overall performance of almost all considered shapes reaches its maximum value. Besides, in the range of $200 \leq \text{Re} \leq 1000$, the microchannel with circular shape pin fin has the highest PEC value. Specifically, within the entire range of Re, the PEC for circular and elliptical shapes is significantly higher than that for triangular and hexagonal shape micro pin fins, with the PEC for the circular micro-pin fin structure slightly higher than that for the elliptical one. Considering the five assessed factors, it can be deduced that the circle cross sectioned fin exhibited the best heat transfer dissipation, although it was associated with a higher pressure drop.

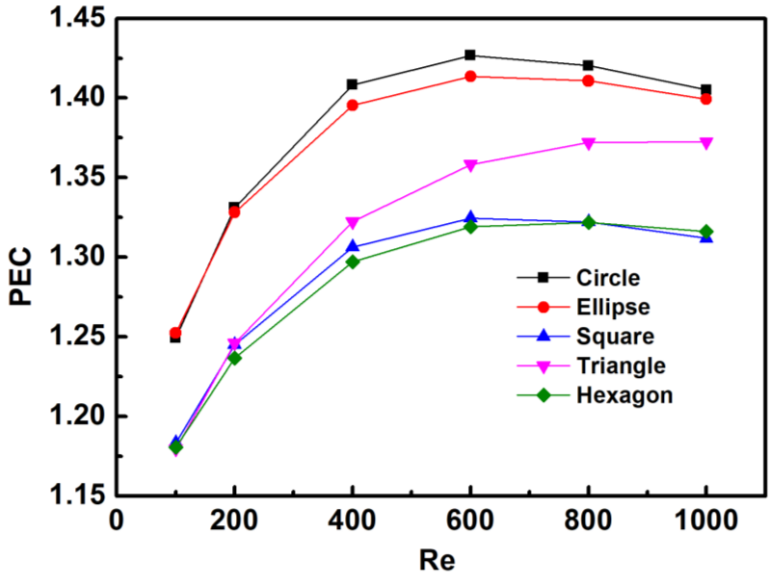

Figure 7-6 Effect of different geometry of MCHS on PEC.

7.4. The effect of spacing distance between adjacent micro pin-fins

This part examines the effect of spacing between adjacent micro pin-fins in the MCHS. In Figure 7.7, the velocity contour and vector plots depict various locations within the MCHS with different spacing distances between adjacent micro pin-fins at Re=600. The plots reveal the existence of secondary flows, particularly in the microchannel with smaller spacing distances. Furthermore, the inclusion of pin-fins in the microchannels leads to vortex shedding, which may further enhances the Nu.

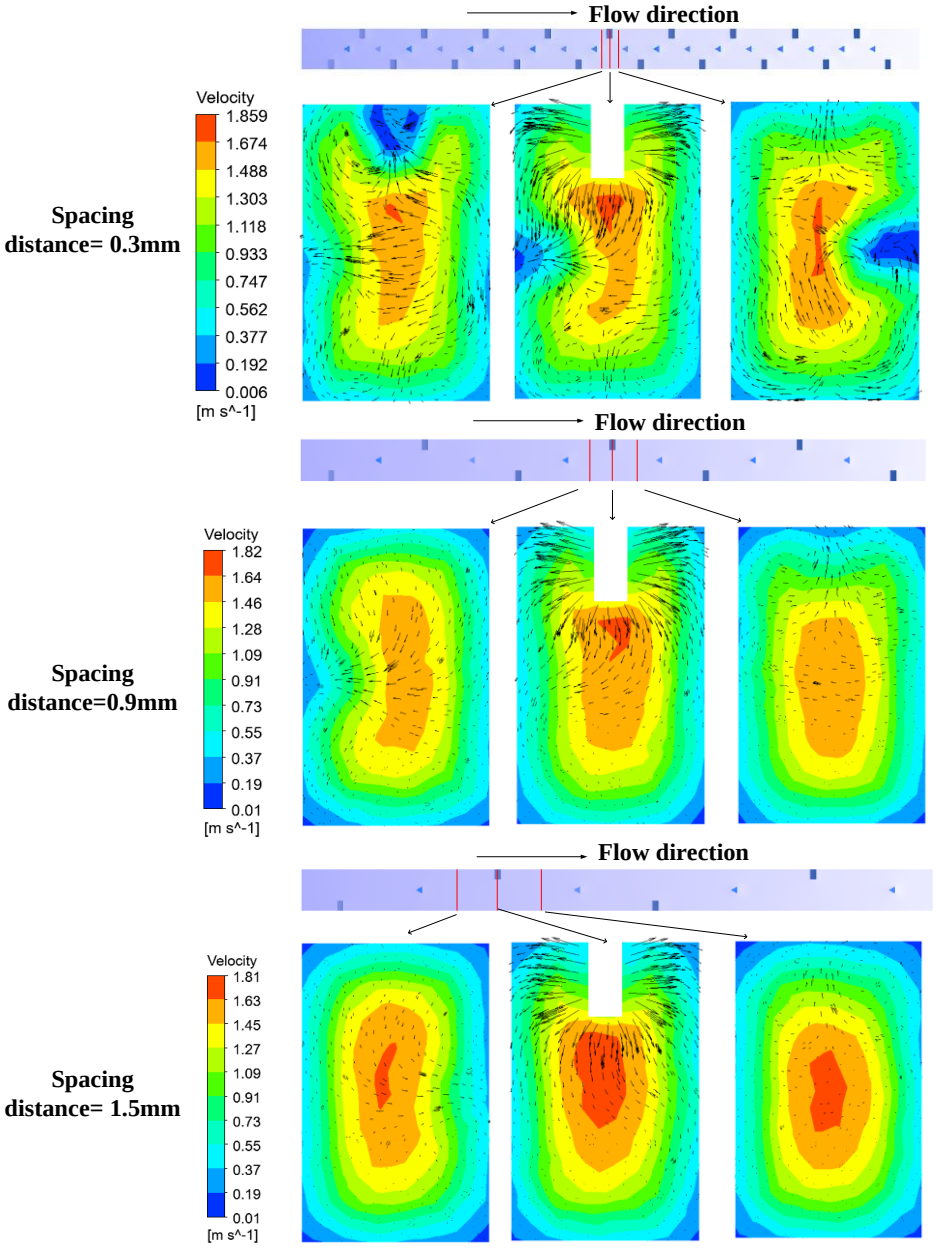

Figure 7-7 Velocity plot (vector+contour) at different positions in the fouth microchannel at different spacing distance of adjust micro-fins.

Figure 13 shows the contour plots for temperature of the MCHS with different spacing distance between adjacent micro pin-fins for Re =600. It can be found that the spacing distance had little influence on the maximum temperature in the microchannel (Figure 7.8(a, c, e, and g)), but it significantly influence the temperature distribution at the outlet of the microchannel, and the one with 0.3 mm spacing distance exhibited the most uniform temperature distribution (Figure 7.8(b, d, f, and h)).

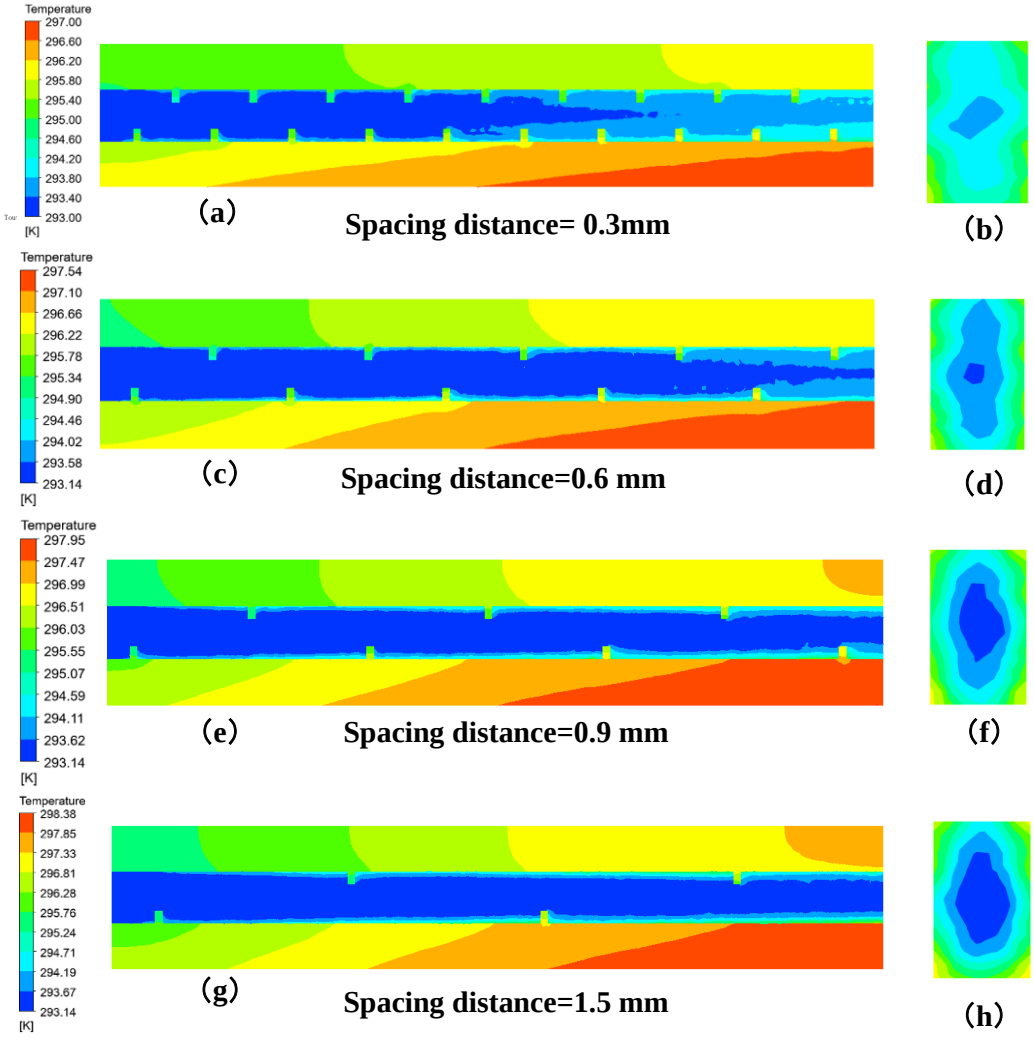

Figure 7-8 Temperature distribution of horizontal plane in the fourth microchannel of the heat sink and the temperature distribution of outlet at different spacing distance (a, b) 0.3 mm, (c, d) 0.6 mm, (e, f) 0.9 mm and (g, h) 1.5 mm when Re=600.

Figure 7.9(a) gives the pressure drop decreases as the spacing distance increases. The effect can be attributed to the reduction in the number of pin-fins in the MCHS, since the increasing spacing distance led to a smaller number of pin-fins, which further resulting in an increase in the volume of the working fluid. According to the continuity equation and Bernoulli's equation, larger volume of the coolant causes a decrease in the pressure difference between the inlet and outlet. From Figure 7.9(a), it is also evident that the thermal resistance decreased with the increase of spacing distances. This is because reducing the spacing distance between adjacent micro-pin fins simultaneously enhanced thermal convection and conduction in microchannels, thereby achieving the effect of reduced thermal resistance. Nevertheless, it is noticed that as the Re increased, the rate at which thermal resistance decreased became slower. This observation implies that there exists a threshold beyond which increasing the spacing distance to reduce thermal resistance becomes less economically beneficial. Figure 7.9(b) shows the dimensionless outlet temperature decreases with increasing Re, and at a certain Re, the effect of spacing on dimensionless temperature was not critical for spacing distance of 0.6 mm to 1.5 mm. However, the dimensionless outlet temperature with 0.3 mm spacing was significantly enhanced compared with that of 0.6 mm spacing. The result of the variation of Nu presented in Figure 7.9(b) shows that the Nu for the 0.3 mm spacing distance at various Re number was the highest. Here, it was observed to be 16.8% and 24.5% larger than 0.6 and 0.9 mm spacing distance at Re=1000 respectively. The 0.6 mm spacing distance was observed to perform as the second highest with heat transfer capacity of 54.8 at Re=1000. It can be explained that smaller spacing distance led to more pin-fins in each microchannel, resulting in the disruption of the thermal boundary layer and the frequent

regeneration of the boundary. Therefore, thermal boundary layer separation and its redevelopment decreased the thickness of average thermal boundary layer, thus enhancing the heat transfer performance.

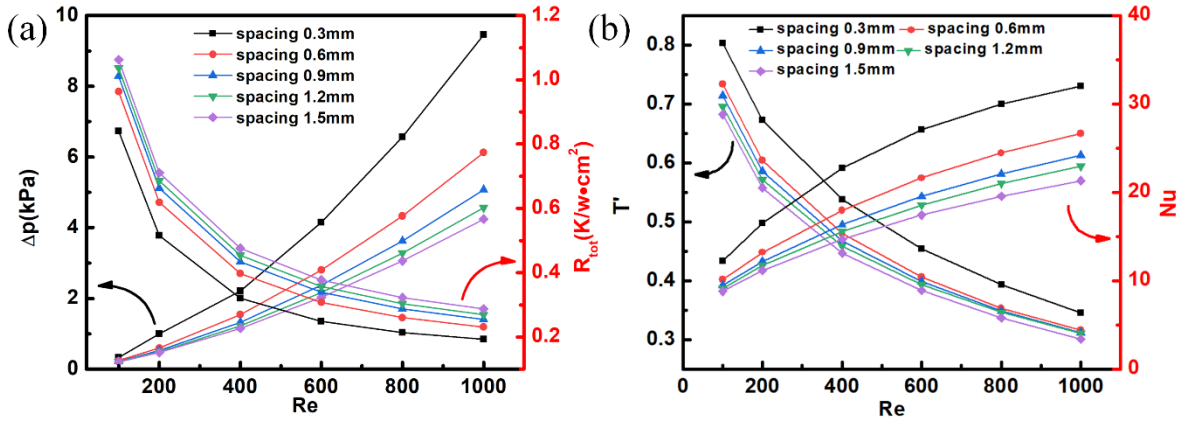

Figure 7-9 Effect of spacing distance between adjacent micro pin-fins on (a) pressure drop and the total thermal resistance, (b) dimensionless outlet temperature and Nu.

The comparison of PEC for different adjacent micro-pin fin spacings is shown in Figure 7.10. Within the considered range of Re number, the PEC with spacing of 0.3 mm and 0.6 mm initially increases and then decreases with increasing Re, with the maximum PEC occurring at *Re*=600 for the 0.3 mm spacing, and at Re=800 for the 0.6 mm spacing. On the other hand, when the spacing is equal or greater than 0.9 mm, the PEC gradually increases with increasing Re. This indicates that the optimum Re for achieving the best performance of microchannels varies with different spacings. Furthermore, throughout the entire range of Re, the PEC value gradually increases with increasing spacing, and the PEC value for the 0.3 mm spacing is significantly higher than in other cases. It can be concluded that although a larger pump power would be required to maintain the MCHS, the microchannel with 0.3 mm spacing distance shows the best overall thermal and hydraulic performance.

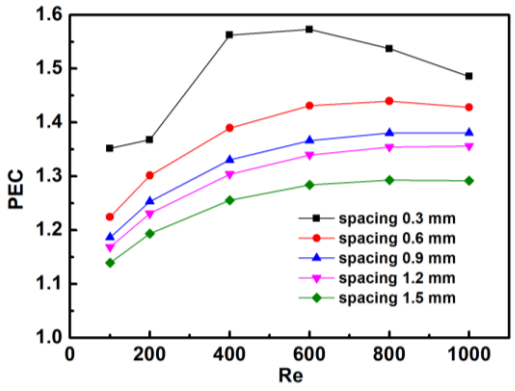

Figure 7-10 Effect of spacing distance between adjacent micro pin-fins on PEC.

7.5. The effect of GO/MEPCM slurry

In this section, we investigate the effect of GO/MEPCM slurry on microchannel heat dissipation. As shown in Table 3.9, when different contents of GO are added to MEPCM, its thermal and physical properties will also change, thereby affecting the cooling effect on microchannels. From Figure 7.11(a, b), it can be seen that the pressure drop and thermal resistance in microchannels using GO/MEPCM slurry as the coolant are generally greater than those using water as the coolant. This is because adding GO/MEPCM particles to water leads to an increase in dynamic viscosity and thermal conductivity. The increase in viscosity leads to an increase in flow resistance within the GO/MEPCM slurry fluid, resulting in higher pressure drop. It should be pointed out that the microchannel of MEPCM slurry with 0.1 wt% GO produces the maximum pressure drop, while the microchannel of slurry with 0.2 wt% GO produces the maximum thermal resistance. This indicates that the increase in pressure drop and thermal resistance of microchannels is not positively correlated with the amount of GO added. From Figure 7.11(c, d), it shows that GO/MEPCM slurry can significantly increase the Nu and dimensionless outlet temperature of microchannels, and with the increase of Re, the dimensionless outlet temperature does not change much with the increase of GO, basically between 0.70 and 0.80. This indicates that there is not much difference between the outlet temperature and the average wall temperature throughout the entire Re range. Adding GO/MEPCM can greatly reduce the

temperature difference between the wall and outlet of the microchannel, and the temperature difference remains basically unchanged as *Re* increases. In addition, at different GO contents, the Nu of microchannels increases with the increase of *Re*.

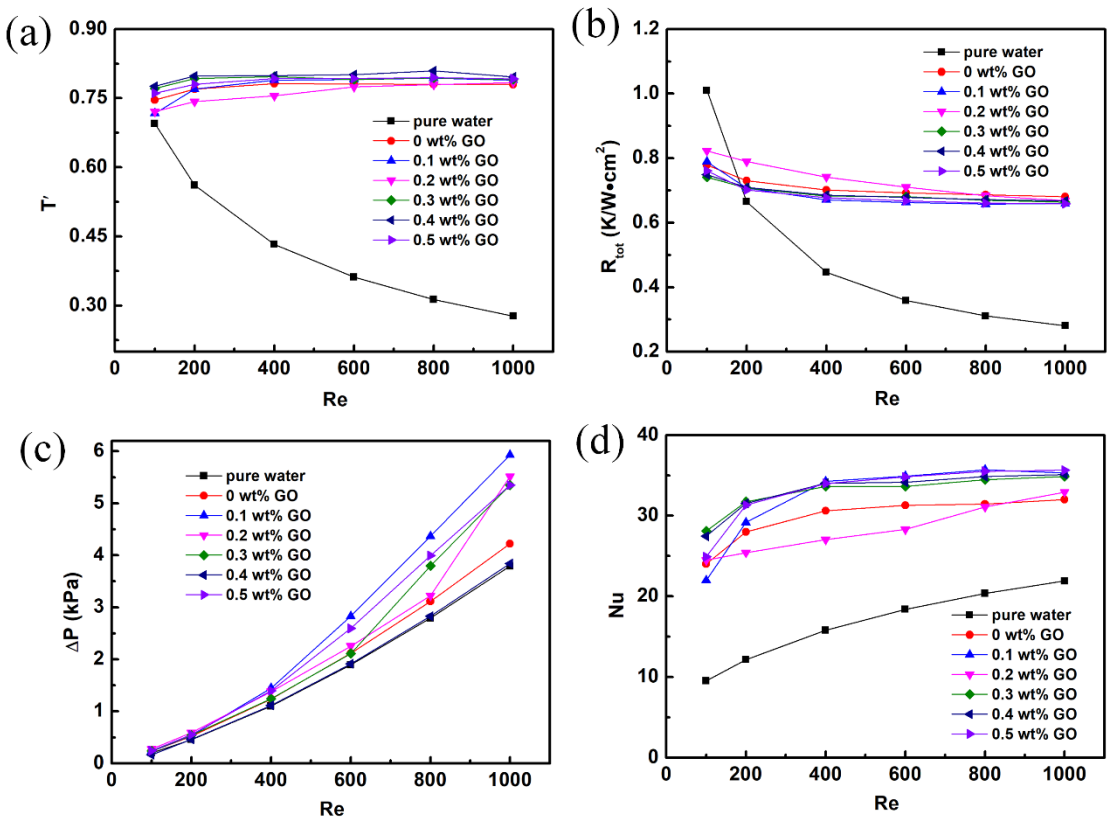

Figure 7-11 Effect of GO/MEPCM slurry on (a) pressure drop, (b) the total thermal resistance, (c) dimensionless outlet temperature and (d) Nu.

As discussed in the introduction section, the Al_2O_3 nanofluids has been used to improve the thermal performance of the microchannel. Therefore, in this section, by using the thermophysical properties of Al_2O_3 nanoparticles [43] in Table 7.1, the effect of Al_2O_3 nanoparticles will also be studied to compare with that of using GO/MEPCM slurry as the coolant. As shown in Figure 7.12(a), within the range of Re numbers

considered, the PEC decreases with the increase of GO content. The PEC of GO/MEPCM slurry is much higher than that of water coolant, and its PEC value is 84% higher than that of Al_2O_3 nanofluid coolant when Re=400, as shown in Figure 7.12(b). It is worth noting that throughout the entire *Re* range, the PEC of the microchannel remains at its maximum value when the GO content is 0.4wt%. This indicates that exists an optimal GO content value to obtain the best overall performance of the microchannel system.

Table 7-1 Thermophysical properties of nanofluids with 5 wt% Al_2O_3 volume fraction.

Al_2O_3 Contents	Density (kg/m^3)	Specific heat capacity (J/kg·K)	Thermal conductivity (W/m·K)	Dynamic viscosity (kg/m·s)
5 wt% Al_2O_3	1143.3	3601.8	0.689	0.00113

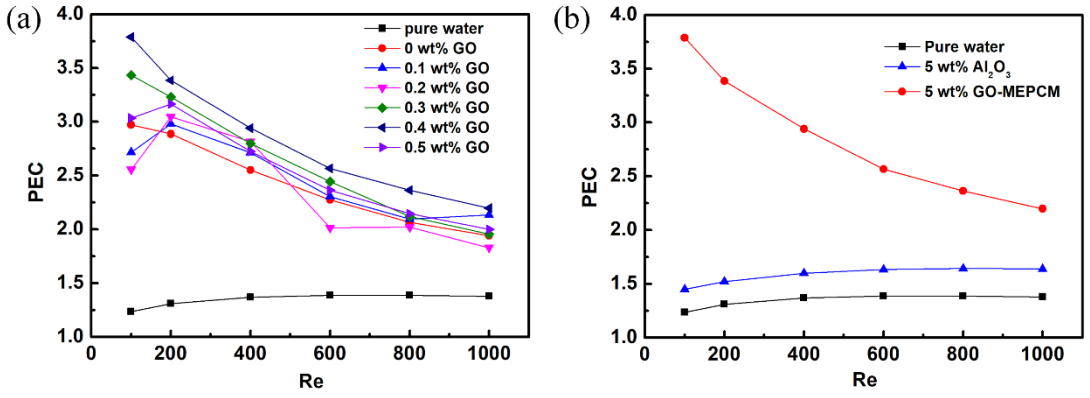

Figure 7-12 (a) Effect of GO on PEC with 5 wt% GO-MEPCM, (b) comparison between Al_2O_3 nanofluids and GO-MEPCM slurry with 0.4 wt GO% on PEC.

7.6. Summary

The heat dissipated by microelectronic devices can deteriorate their performance. One way to address this issue is by utilizing microchannel heat sink, which can significantly enhance heat transfer performance through the use of improved working fluids and channel structures. In this chapter, a novel design of different arrangements and shapes of micro pin-fins is proposed and comparative analysis has been conducted to examine the heat transfer enhancement evaluated by pressure drop, dimensionless outlet temperature, thermal resistance, Nusselt number (Nu) and the overall performance evaluation criterion (PEC). Based on this, the impacts of graphene oxide/ micro-encapsulated phase change material (GO/MEPCM) slurry were investigated in the microchannel heat sink with optimum heat transfer capacity. The results demonstrate that the Nu for the novel design is 59.9% larger than that of unfinned structure when Reynolds number (Re)=1000, while the PEC can be up to 1.43. It also shows that the microchannel with 0.3 mm spacing distance between adjacent circle shaped cross-sectional pin-fins exhibit better PEC performance than other cases even though it has the largest pressure drop. When GO/MEPCM slurry is used as the coolant in the microchannel, the PEC of the microchannel remains at its maximum value throughout the entire Re range when 0.4 wt% of GO is used, which is 84% higher than that when Al_2O_3 nanofluid is used as a coolant.

Chapter 8 - Conclusions and recommended future work

8.1. Conclusions

Phase change materials (PCMs) are substances that melt and solidify at almost constant temperatures, and can store or release a large amount of energy during phase change. Microcapsule technologies have been widely used to encapsulate PCMs, which broadens its application range and improves the efficiency of thermal management. Microencapsulated phase change material (MEPCMs) are getting more and more attention in the development of energy field. In this project, a needle-based microfluidic device has been proposed to prepare the MEPCMs with or without graphene/GO as the shell. Besides, a novel microchannel heat sink design with pin-fin structure was proposed with varying fin geometries and fin spacing. Various configurations and GO/MEPCM slurry were numerically analyzed to determine the optimal fin geometry and spacing. A comparative analysis of the predicted results yielded the following conclusions:

- Numerical examination showed that increasing continuous phase velocity or reducing interfacial tension decreases LMPA droplet size and increases formation frequency in a microcahnnel. Higher interfacial tension decreases solidification time, while temperature changes affect solidification time but not droplet size or frequency. Besides, by combining oscillatory flow-induced breakup and phase change in a straight microchannel, it was found that reducing wall temperature speeds up LMPA droplet solidification, creating ultra-small particles in 3 ms.
- The synthesis of MEPCM and graphene/GO decorated MEPCM have been synthesized in a

needle based microfluidic device. The results showed that the microcapsules have uniform particle size, smooth surface and spherical shape. The coefficient of size variation was within 5%. The thermal storage performance of MEPCMs and graphene/MEPCMs were studied by differential scanning calorimetry and the results showed that the microcapsules have good phase transition performance and high thermal storage performance. Besides, the shell material of microcapsules offered good protection for the PCM material. The addition of graphene to the microcapsules does not affect the phase-change enthalpy. As the mass ratio of graphene increased from 0.1 to 2 wt%, a remarkable enhancement in heat conductivity was observed, underscoring the significant role of multilayer graphene in improving heat transfer within the PCM microcapsules. These favorable characteristics make MEPCMs with graphene/GO enhanced HDDA enclosure being potential materials for storing thermal energy.

- The thermal performance and pressure drop characteristics of various microchannel configurations and coolants were compared. Novel design (Structure C) demonstrated the best PEC performance, achieving up to 1.43 at Re=600. Micro pin fin geometric shape had minimal impact on thermal resistance, but triangular fins led to the highest pressure drop. Circular pins had the highest PEC, outperforming hexagonal fins by over 8% at certain Re ranges. The spacing distance of micro pin fins affected temperature distribution at the outlet and influenced PEC optimization, with 0.3 mm spacing achieving the highest PEC of 1.57 at Re=600. The pressure drop and thermal resistance in microchannels using GO/MEPCM slurry as coolant are greater than those using water as coolant. At different GO contents, the Nu of microchannels increases with the increase of Re. Throughout the entire range of Re, the PEC of microchannels remains at its maximum value when the GO content is 0.4wt% and

reaches 3.79 when Re=100. Besides, the PEC of GO/MEPCM slurry is much higher than that of water coolant, and its PEC value is 84% higher than that of Al2O3 nanofluid coolant when Re=400.

8.2. Recommended future work

As is evident throughout this review, microfluidics offers precise control over the encapsulation process, resulting in uniform and well-defined microcapsules with desired properties. Various microfluidic techniques have been developed, allowing for the encapsulation of different PCMs within protective shells. The morphology of microcapsules can be tailored, and thermal properties can be enhanced through the incorporation of additives. Nevertheless, there are still several challenges that need to be addressed to optimize the design of MEPCM or graphene/MEPCM microcapsules, which include investigating new materials for the core of the MEPCM or graphene/MEPCM microcapsules, developing new microfluidic chip, scaling up production for commercialization and exploring new applications for these microcapsules.

8.2.1. Investigating new materials for the core of the graphene/MEPCM microcapsules:

The majority of MEPCM microcapsules produced using microfluidic control techniques are typically prepared at room temperature. This requirement poses a limitation on the choice of phase change materials for the core of these MEPCM microcapsules, as they must be in liquid form at room temperature [49, 51, 52, 54, 81, 84]. Consequently, the current selection of core materials is relatively limited. However, there is an exciting potential for future advancements by manipulating the working temperature during the encapsulation process. This opens up opportunities for incorporating different types of phase change materials with diverse properties and applications.

For instance, by adjusting the working temperature, it becomes possible to consider low melting point alloys as potential core materials, which possess advantageous characteristics, such as high thermal conductivity and excellent heat storage capacity, making them suitable for applications such as thermal energy storage and heat transfer systems. Besides, fatty acids are another class of core materials that can be explored. Fatty acids exhibit phase change behavior at relatively low temperatures, making them suitable for various applications, including thermal regulation, energy storage, and controlled release systems.

8.2.2. Developing new microfluidic chips for graphene/MEPCM microcapsules preparation:

At present, the microfluidics chips used for MEPCM microcapsules preparation are complex and expensive due to precision manufacturing techniques, specialized materials, multi-layered structures and integration of components, which contribute to increased complexity and costs [51, 52, 54, 55, 84]. As a result, it is crucial to explore new chip designs that are simpler and more cost-effective. One promising alternative is the use of modular microfluidics for the production of MEPCM microcapsules [179, 180]. One of the major benefits of using modular microfluidics systems is its simplicity in chip assembly [180]. Unlike traditional microfluidic chip designs, which can be complex and require intricate fabrication processes, the modular microfluidic system can be easily assembled and disassembled using commercially available components. This reduces the overall cost and complexity of chip production. Moreover, the modular microfluidic system offers reusability, which can be easily disassembled and cleaned, allowing for multiple uses without the need for frequent replacement. This not only reduces the cost associated with chip materials but also minimizes waste generation.

8.2.3. Scaling up the production process from lab-scale to commercial-scale:

Currently, the preparation of MEPCM microcapsules using microfluidic control is primarily limited to laboratory-scale production, making it difficult to generate large quantities of MEPCM microcapsules [52, 84, 100, 181]. One method that shows promise for scaling up the production is by utilizing microfluidics chips with a parallel geometry. The parallel geometry of microfluidics chips allows for the simultaneous production of multiple microcapsules, increasing the production rate and efficiency. By designing the chip with parallel channels or compartments, it becomes possible to process multiple samples in parallel, thereby increasing the throughput. However, it is important to note that the parallel system of traditional microfluidics chips can be complex and expensive to manufacture. As a result, ongoing research and development should be focused on simplifying the manufacturing process and reducing costs while maintaining the benefits of the parallel geometry. By optimizing the design and fabrication techniques, it may be possible to make the production of MEPCM microcapsules on a larger scale more accessible and cost-effective.

8.2.4. Developing new applications:

As discussed above, MEPCM microcapsules are not limited to building, textiles, solar energy utilization and military aviation; they can also serve as multifunctional materials for both catalysis and energy storage by adding nanomaterials [54]. Therefore, the exploration of multifunctional MEPCM microcapsules can be a promising direction. MEPCM microcapsules can combine the thermal energy storage capacity of PCMs with other functional characteristics of added nanomaterials. For instance, by adding other nanomaterials with good electrical conductivity, such as metal nanoparticles or conductive polymers, MEPCM microcapsules can be endowed with

conductive functions. Such multifunctional microcapsules can be used for energy storage in electronic devices, such as supercapacitors or batteries. By adding nanomaterials with sensing properties, such as magnetic nanoparticles or photosensitive nanoparticles, phase change microcapsules can respond to external stimuli and be used to prepare controllable release systems or intelligent sensors. By introducing nanomaterials with fluorescent properties, such as quantum dots or fluorescent dyes, phase change microcapsules can be used for labeling and tracking applications, such as biomedical imaging and biosensing.

Acknowledgments

This project was financially supported by Ningbo Science and Technology Bureau under project code 2019B10042. This project was partially supported by the Nottingham Ningbo China Beacons of Excellence Research and Innovation Institute (budget code: I01211200007). I acknowledge the Ph.D. scholarship from the University of Nottingham Ningbo China.

References:

[1] A. Jamekhorshid, S. M. Sadrameli, M. Farid, A review of microencapsulation methods of phase change materials (PCMs) as a thermal energy storage (TES) medium, Renewable and Sustainable Energy Reviews, 31 (2014) 531-542.
[2] Y. Zhao, X. Zhang, W. Hua, Review of preparation technologies of organic composite phase change materials in energy storage, Journal of Molecular Liquids, 336 (2021) 115923.
[3] M. He, Y. Wang, D. Li, M. Zhang, T. Wang, F. Zhi, X. Ji, D. Ding, Recent applications of phase-change materials in tumor therapy and theranostics, Biomaterials Advances, 147 (2023) 213309.
[4] Y. Sheikh, M. O. Hamdan, S. Sakhi, A review on micro-encapsulated phase change materials (EPCM) used for thermal management and energy storage systems: Fundamentals, materials, synthesis and applications, Journal of Energy Storage, 72 (2023) 108472.
[5] H. Akeiber, P. Nejat, M. Z. A. Majid, M. A. Wahid, F. Jomehzadeh, I. Zeynali Famileh, J. K. Calautit, B. R. Hughes, S. A. Zaki, A review on phase change material (PCM) for sustainable passive cooling in building envelopes, Renewable and Sustainable Energy Reviews, 60 (2016) 1470-1497.
[6] M. Geszke-Moritz, M. Moritz, Solid lipid nanoparticles as attractive drug vehicles: Composition, properties and therapeutic strategies, Materials Science and Engineering: C, 68 (2016) 982-994.

[7] M. S. Ghoghaei, A. Mahmoudian, O. Mohammadi, M. B. Shafii, H. Jafari Mosleh, M. Zandieh, M. H. Ahmadi, A review on the applications of micro-/nano-encapsulated phase change material slurry in heat transfer and thermal storage systems, Journal of Thermal Analysis and Calorimetry, 145(2) (2020) 245-268.
[8] B. Xu, P. Li, C. Chan, Application of phase change materials for thermal energy storage in concentrated solar thermal power plants: A review to recent developments, Applied Energy, 160 (2015) 286-307.
[9] Y. Lin, G. Alva, G. Fang, Review on thermal performances and applications of thermal energy storage systems with inorganic phase change materials, Energy, 165 (2018) 685-708.
[10] S. A. Mohamed, F. A. Al-Sulaiman, N. I. Ibrahim, M. H. Zahir, A. Al-Ahmed, R. Saidur, B. S. Yılbaş, A. Z. Sahin, A review on current status and challenges of inorganic phase change materials for thermal energy storage systems, Renewable and Sustainable Energy Reviews, 70 (2017) 1072-1089.
[11] S. D. Sharma, K. Sagara, Latent Heat Storage Materials and Systems: A Review, International Journal of Green Energy, 2(1) (2005) 1-56.
[12] C. Castellon, N. Miquel, J. Roca, M. Medrano, L. F. Cabeza, Microencapsulated phase changing materials (PCM) for building applications, Proceedings of the 10th International Conference on Thermal Energy Storage, (2006).
[13] H. D. Han, A. K. Kan, J. Ji, G. L. Mei, Application of microencapsulated phase change material in building energy conservation, First International Conference on Building Energy and Environment, Proceedings, 1-3 (2008) 1640-1647.
[14] A. T. Naikwadi, A. B. Samui, P. A. Mahanwar, Fabrication and experimental investigation of microencapsulated eutectic phase change material-integrated polyurethane sandwich tin panel composite for thermal energy storage in buildings, International Journal of Energy Research, 45 (2021) 20783-20794.
[15] Z. Qiu, X. Ma, P. Li, X. Zhao, A. Wright, Micro-encapsulated phase change material (MPCM) slurries: Characterization and building applications, Renewable and Sustainable Energy Reviews, 77 (2017) 246-262.
[16] X. Geng, W. Li, Y. Wang, J. Lu, J. Wang, N. Wang, J. Li, X. Zhang, Reversible thermochromic microencapsulated phase change materials for thermal energy storage application in thermal protective clothing, Applied Energy, 217 (2018) 281-294.
[17] X. Geng, W. Li, Q. Yin, Y. Wang, N. Han, N. Wang, J. Bian, J. Wang, X. Zhang, Design and fabrication of reversible thermochromic microencapsulated phase change materials for thermal energy storage and its antibacterial activity, Energy, 159 (2018) 857-869.
[18] F. Jiang, X. Wang, D. Wu, Magnetic microencapsulated phase change materials with an organo-silica shell: Design, synthesis and application for electromagnetic shielding and thermal regulating polyimide films, Energy, 98 (2016) 225-239.
[19] S. Chen, X. Wang, W. Li, S. Wang, Y. Qi, X. Li, Y. Zhao, T. Zhu, T. Ma, X. Xie, Experimental study on cooling performance of microencapsulated phase change suspension in a PEMFC, International Journal of Hydrogen Energy, 42(50) (2017) 30004-30012.
[20] G. V. N. Trivedi, R. Parameshwaran, Microencapsulated phase change material suspensions for cool thermal energy storage, Materials Chemistry and Physics, 242 (2020) 122519.
[21] M. Eisapour, A. H. Eisapour, M. J. Hosseini, P. Talebizadehsardari, Exergy and energy analysis of wavy tubes photovoltaic-thermal systems using microencapsulated PCM nano-slurry coolant fluid, Applied Energy, 266 (2020) 114849.
[22] G. Fang, H. Li, X. Liu, Preparation and properties of lauric acid/silicon dioxide composites as form-stable phase change materials for thermal energy storage, Materials Chemistry and Physics, 122(2) (2010) 533-536.

[23] Y. Özonur, M. Mazman, H. Ö. Paksoy, H. Evliya, Microencapsulation of coco fatty acid mixture for thermal energy storage with phase change material, International Journal of Energy Research, 30(10) (2006) 741-749.
[24] X. X. Zhang, X. C. Wang, X. M. Tao, K. L. Yick, Energy storage polymer/MicroPCMs blended chips and thermo-regulated fibers, Journal of Materials Science, 40(14) (2005) 3729-3734.
[25] X.-Y. Gao, N. Han, X.-X. Zhang, W.-Y. Yu, Melt-processable acrylonitrile–methyl acrylate copolymers and melt-spun fibers containing MicroPCMs, Journal of Materials Science, 44(21) (2009) 5877-5884.
[26] K. Iqbal, D. Sun, Development of thermo-regulating polypropylene fibre containing microencapsulated phase change materials, Renewable Energy, 71 (2014) 473-479.
[27] C. Chen, L. Wang, Y. Huang, Electrospun phase change fibers based on polyethylene glycol/cellulose acetate blends, Applied Energy, 88(9) (2011) 3133-3139.
[28] W. Li, Y.-J. Ma, X.-F. Tang, N. Jiang, R. Zhang, N. Han, X.-X. Zhang, Composition and Characterization of Thermoregulated Fiber Containing Acrylic-Based Copolymer Microencapsulated Phase-Change Materials (MicroPCMs), Industrial & Engineering Chemistry Research, 53(13) (2014) 5413-5420.
[29] L. De Windt, D. Dabo, S. Lidelöw, R. Badreddine, A. Lagerkvist, MSWI bottom ash used as basement at two pilot-scale roads: Comparison of leachate chemistry and reactive transport modeling, Waste Management (Oxford), 31(2) (2011) 267-280.
[30] L. Sánchez, P. Sánchez, A. De Lucas, M. Carmona, J. F. Rodríguez, Microencapsulation of PCMs with a polystyrene shell, Colloid and Polymer Science, 285(12) (2007) 1377-1385.
[31] B. Fei, H. Lu, K. Qi, H. Shi, T. Liu, X. Li, J. H. Xin, Multi-functional microcapsules produced by aerosol reaction, Journal of Aerosol Science, 39(12) (2008) 1089-1098.
[32] R. Yang, H. Xu, Y. Zhang, Preparation, physical property and thermal physical property of phase change microcapsule slurry and phase change emulsion, Solar Energy Materials and Solar Cells, 80(4) (2003) 405-416.
[33] Y. Jin, W. Lee, Z. Musina, Y. Ding, A one-step method for producing microencapsulated phase change materials, Particuology, 8(6) (2010) 588-590.
[34] H.-T. Wu, M.-W. Yang, Precipitation kinetics of PMMA sub-micrometric particles with a supercritical assisted-atomization process, The Journal of Supercritical Fluids, 59 (2011) 98-107.
[35] A. Sarı, C. Alkan, A. Karaipekli, Preparation, characterization and thermal properties of PMMA/n-heptadecane microcapsules as novel solid–liquid microPCM for thermal energy storage, Applied Energy, 87(5) (2010) 1529-1534.
[36] Y. Wang, T. D. Xia, H. X. Feng, H. Zhang, Stearic acid/polymethylmethacrylate composite as form-stable phase change materials for latent heat thermal energy storage, Renewable Energy, 36(6) (2011) 1814-1820.
[37] C. Liang, X. Lingling, S. Hongbo, Z. Zhibin, Microencapsulation of butyl stearate as a phase change material by interfacial polycondensation in a polyurea system, Energy Conversion and Management, 50(3) (2009) 723-729.
[38] S. Yan, D. Yuan, Continuous microfluidic 3D focusing enabling microflow cytometry for single-cell analysis, Talanta, 221 (2021) 121401.
[39] S. Yan, Q. Yuan, J. Wu, Z. Jia, A free-standing, phase-change liquid metal mold for 3D flexible microfluidics, Frontiers in Bioengineering and Biotechnology, 10 (2022).
[40] X. Xu, X. Huang, J. Sun, J. Chen, G. Wu, Y. Yao, N. Zhou, S. Wang, L. Sun, 3D-Stacked Multistage Inertial Microfluidic Chip for High-Throughput Enrichment of Circulating Tumor Cells, Cyborg and Bionic Systems, 2022 (2022) 1-10.
[41] P. Zhu, L. Wang, Passive and active droplet generation with microfluidics: a review, Lab on a Chip, 17(1) (2017) 34-75.

[42] T. Y. Lee, T. M. Choi, T. S. Shim, R. a. M. Frijns, S. H. Kim, Microfluidic production of multiple emulsions and functional microcapsules, Lab on a Chip, 16(18) (2016) 3415-3440.
[43] T. Kong, J. Wu, K. W. K. Yeung, M. K. T. To, H. C. Shum, L. Wang, Microfluidic fabrication of polymeric core-shell microspheres for controlled release applications, Biomicrofluidics, 7(4) (2013) 044128.
[44] S. Yan, Y. Li, Q. Zhao, D. Yuan, G. Yun, J. Zhang, W. Wen, S. Y. Tang, W. Li, Liquid metal-based amalgamation-assisted lithography for fabrication of complex channels with diverse structures and configurations, Lab Chip, 18(5) (2018) 785-792.
[45] T. Ge, S. Yan, L. Zhang, H. He, L. Wang, S. Li, Y. Yuan, G. Chen, Y. Huang, Nanowire assisted repeatable DEP–SERS detection in microfluidics, Nanotechnology, 30(47) (2019) 475202.
[46] D. Liu, C. Liu, Y. Yuan, X. Zhang, Y. Huang, S. Yan, Microfluidic Transport of Hybrid Optoplasmonic Particles for Repeatable SERS Detection, Analytical Chemistry, 93(30) (2021) 10672-10678.
[47] P. Pattanayak, S. K. Singh, M. Gulati, S. Vishwas, B. Kapoor, D. K. Chellappan, K. Anand, G. Gupta, N. K. Jha, P. K. Gupta, P. Prasher, K. Dua, H. Dureja, D. Kumar, V. Kumar, Microfluidic chips: recent advances, critical strategies in design, applications and future perspectives, Microfluidics and Nanofluidics, 25(12) (2021) 99.
[48] Z. Ma, B. Li, J. Peng, D. Gao, Recent Development of Drug Delivery Systems through Microfluidics: From Synthesis to Evaluation, Pharmaceutics, 14(2) (2022) 434.
[49] S. Lone, H. M. Lee, G. M. Kim, W.-G. Koh, I. W. Cheong, Facile and highly efficient microencapsulation of a phase change material using tubular microfluidics, Colloids and Surfaces A: Physicochemical and Engineering Aspects, 422 (2013) 61-67.
[50] S. Parvate, G. T. Vladisavljević, N. Leister, A. Spyrou, G. Bolognesi, D. Baiocco, Z. Zhang, S. Chattopadhyay, Lego-Inspired Glass Capillary Microfluidic Device: A Technique for Bespoke Microencapsulation of Phase Change Materials, ACS Applied Materials & Interfaces, 15(13) (2023) 17195-17210.
[51] G. Q. Wen, R. Xie, W. G. Liang, X. H. He, W. Wang, X. J. Ju, L. Y. Chu, Microfluidic fabrication and thermal characteristics of core-shell phase change microfibers with high paraffin content, Applied Thermal Engineering, 87 (2015) 471-480.
[52] J. Li, L. Jia, Y. Chen, L. Li, S. Mo, J. Wang, C. Wang, Microfluidic fabrication and thermal properties of microencapsulated n-heptadecane with hexanediol diacrylate shell for thermal energy storage, Applied Thermal Engineering, 162 (2019) 114278.
[53] T. Watanabe, Y. Sakai, N. Sugimori, T. Ikeda, M. Monzen, T. Ono, Microfluidic Production of Monodisperse Biopolymer Microcapsules for Latent Heat Storage, ACS Materials Au, 2(3) (2022) 250-259.
[54] R. Al Nuumani, G. Bolognesi, G. T. Vladisavljević, Microfluidic Production of Poly(1,6-hexanediol diacrylate)-Based Polymer Microspheres and Bifunctional Microcapsules with Embedded TiO(2) Nanoparticles, Langmuir, 34(39) (2018) 11822-11831.
[55] T. Shi, P. Hu, J. Wang, Preparation of Polyurea Microcapsules Containing Phase Change Materials Using Microfluidics, ChemistrySelect, 5(7) (2020) 2342-2347.
[56] J. Wu, T. Kong, K. W. K. Yeung, H. C. Shum, K. M. C. Cheung, L. Wang, M. K. T. To, Fabrication and characterization of monodisperse PLGA–alginate core–shell microspheres with monodisperse size and homogeneous shells for controlled drug release, Acta Biomaterialia, 9(7) (2013) 7410-7419.
[57] T. Kong, Z. Liu, Y. Song, L. Wang, H. C. Shum, Engineering polymeric composite particles by emulsion-templating: thermodynamics versus kinetics, Soft Matter, 9(41) (2013) 9780-9784.
[58] Z. Kang, T. Kong, L. Lei, P. Zhu, X. Tian, L. Wang, Engineering particle morphology with microfluidic droplets, Journal of Micromechanics and Microengineering, 26(7) (2016) 075011.

[59] J. Nunes, S. Tsai, J. Wan, H. A. Stone, Dripping and jetting in microfluidic multiphase flows applied to particle and fibre synthesis, Journal of Physics D: Applied Physics, 46(11) (2013) 114002.
[60] J. Love Christopher, J. R. Anderson, G. M. Whitesides, Fabrication of Three-Dimensional Microfluidic Systems by Soft Lithography, MRS Bulletin, 26(7) (2001) 523-528.
[61] G. F. Christopher, S. L. Anna, Microfluidic methods for generating continuous droplet streams, Journal of Physics D: Applied Physics, 40(19) (2007) R319.
[62] A. Utada, E. Lorenceau, D. Link, P. Kaplan, H. A. Stone, D. A. Weitz, Monodisperse Double Emulsions Generated from a Microcapillary Device, Science (New York, N.Y.), 308 (2005) 537-541.
[63] L.-Y. Chu, A. S. Utada, R. K. Shah, J.-W. Kim, D. A. Weitz, Controllable Monodisperse Multiple Emulsions, Angewandte Chemie International Edition, 46(47) (2007) 8970-8974.
[64] N. Pannacci, H. Bruus, D. Bartolo, I. Etchart, T. Lockhart, Y. Hennequin, H. Willaime, P. Tabeling, Equilibrium and Nonequilibrium States in Microfluidic Double Emulsions, Physical Review Letters, 101(16) (2008) 164502.
[65] S.-H. Kim, J. W. Kim, J.-C. Cho, D. A. Weitz, Double-emulsion drops with ultra-thin shells for capsule templates, Lab on a Chip, 11(18) (2011) 3162-3166.
[66] C. Cramer, P. Fischer, E. J. Windhab, Drop formation in a co-flowing ambient fluid, Chemical Engineering Science, 59(15) (2004) 3045-3058.
[67] A. S. Utada, A. Fernandez-Nieves, H. A. Stone, D. A. Weitz, Dripping to Jetting Transitions in Coflowing Liquid Streams, Physical Review Letters, 99(9) (2007) 094502.
[68] X. Liu, L. Wu, Y. Zhao, Y. Chen, Study of compound drop formation in axisymmetric microfluidic devices with different geometries, Colloids and Surfaces A: Physicochemical and Engineering Aspects, 533 (2017) 87-98.
[69] D. Saeki, S. Sugiura, T. Kanamori, S. Sato, S. Ichikawa, Microfluidic preparation of water-in-oil-in-water emulsions with an ultra-thin oil phase layer, Lab on a Chip, 10(3) (2010) 357-362.
[70] D. Sun, Y. Wang, D. Jiang, N. Xiang, K. Chen, Z. Ni, Dynamic self-assembly of particles in an expanding channel flow, Applied Physics Letters, 103(7) (2013) 071905.
[71] H. Peng, Z. Xu, S. Chen, Z. Zhang, B. Li, L. Ge, An easily assembled double T-shape microfluidic devices for the preparation of submillimeter-sized polyacronitrile (PAN) microbubbles and polystyrene (PS) double emulsions, Colloids and Surfaces A: Physicochemical and Engineering Aspects, 468 (2015) 271-279.
[72] C. Zhou, P. Yue, J. J. Feng, Formation of simple and compound drops in microfluidic devices, Physical of Fluids, 18(9) (2006) 092105.
[73] T. V. Vu, S. Homma, G. Tryggvason, J. C. Wells, H. Takakura, Computations of breakup modes in laminar compound liquid jets in a coflowing fluid, International Journal of Multiphase Flow, 49 (2013) 58-69.
[74] P. Guillot, A. Colin, A. S. Utada, A. Ajdari, Stability of a Jet in Confined Pressure-Driven Biphasic Flows at Low Reynolds Numbers, Physical Review Letters, 99(10) (2007) 104502.
[75] K. J. Humphry, A. Ajdari, A. Fernández-Nieves, H. A. Stone, D. A. Weitz, Suppression of instabilities in multiphase flow by geometric confinement, Phys Rev E Stat Nonlin Soft Matter Phys, 79(5 Pt 2) (2009) 056310.
[76] A. R. Abate, M. Kutsovsky, S. Seiffert, M. Windbergs, L. F. V. Pinto, A. Rotem, A. S. Utada, D. A. Weitz, Synthesis of Monodisperse Microparticles from Non-Newtonian Polymer Solutions with Microfluidic Devices, Advanced Material, 23(15) (2011) 1757-1760.
[77] Y. Yu, L. Shang, J. Guo, J. Wang, Y. Zhao, Design of capillary microfluidics for spinning cell-laden microfibers, Nature Protocols, 13(11) (2018) 2557-2579.
[78] K. Ghasemi, S. Tasnim, S. Mahmud, PCM, nano/microencapsulation and slurries: A review of fundamentals, categories, fabrication, numerical models and applications, Sustainable Energy Technologies and Assessments, 52 (2022) 102084.

[79] W. Gao, F. Liu, C. Yu, Y. Chen, X. Liu, Microfluidic method–based encapsulated phase change materials: Fundamentals, progress, and prospects, Renewable and Sustainable Energy Reviews, 171 (2023) 112998.
[80] W.-G. Liang, C. Yang, G.-Q. Wen, W. Wang, X.-J. Ju, R. Xie, L.-Y. Chu, A facile and controllable method to encapsulate phase change materials with non-toxic and biocompatible chemicals, Applied Thermal Engineering, 70(1) (2014) 817-826.
[81] Z. Fu, L. Su, J. Li, R. Yang, Z. Zhang, M. Liu, J. Li, B. Li, Elastic silicone encapsulation of n-hexadecyl bromide by microfluidic approach as novel microencapsulated phase change materials, Thermochim Acta, 590 (2014) 24-29.
[82] K. Akamatsu, M. Ogawa, R. Katayama, K. Yonemura, S. Nakao, A facile microencapsulation of phase change materials within silicone-based shells by using glass capillary devices, Colloids and Surfaces A: Physicochemical and Engineering Aspects, 567 (2019) 297-303.
[83] X. Han, T. Kong, P. Zhu, L. Wang, Microfluidic Encapsulation of Phase-Change Materials for High Thermal Performance, Langmuir, 36(28) (2020) 8165-8173.
[84] G. Hao, C. Yu, Y. Chen, X. Liu, Y. Chen, Controlled microfluidic encapsulation of phase change material for thermo-regulation, International Journal of Heat and Mass Transfer, 190 (2022) 122738.
[85] D. Chong, X. Liu, H. Ma, G. Huang, Y. L. Han, X. Cui, J. Yan, F. Xu, Advances in fabricating double-emulsion droplets and their biomedical applications, Microfluidics and Nanofluidics, 19(5) (2015) 1071-1090.
[86] C. Decker, Kinetic study and new applications of UV radiation curing, Macromolecular Rapid Communications, 23(18) (2002) 1067-1093.
[87] D. S. Kim, W. H. Seo, Ultraviolet‐curing behavior and mechanical properties of a polyester acrylate resin, Journal of Applied Polymer Science, 92(6) (2004) 3921-3928.
[88] J. Lange, Viscoelastic properties and transitions during thermal and UV cure of a methacrylate resin, Polymer Engineering & Science, 39(9) (1999) 1651-1660.
[89] A. Endruweit, M. Johnson, A. Long, Curing of composite components by ultraviolet radiation: A review, Polymer Composites, 27(2) (2006) 119-128.
[90] Y. Pang, H. Gabriel, K. A. Frantz, F. Saeed, A prospective study of different test targets for the near point of convergence, Ophthalmic and Physiological Optics, 30(3) (2010) 298-303.
[91] W. Su, M. Hu, L. Wang, G. Kokogiannakis, J. Chen, L. Gao, A. Li, C. Xu, Microencapsulated phase change materials with graphene-based materials: Fabrication, characterisation and prospects, Renewable and Sustainable Energy Reviews, 168 (2022) 112806.
[92] S. A. Ryu, Y. H. Hwang, H. Oh, K. Jeon, J. H. Lee, J. Yoon, J. B. Lee, H. Lee, Biocompatible Wax-Based Microcapsules with Hermetic Sealing for Thermally Triggered Release of Actives, ACS Appl Mater Interfaces, 13(30) (2021) 36380-36387.
[93] J. Wang, S. Hahn, E. Amstad, N. Vogel, Tailored Double Emulsions Made Simple, Advanced Material, 34(5) (2022) 2107338.
[94] S. Parvate, G. Vladisavljević, N. Leister, A. Spyrou, G. Bolognesi, D. Baiocco, Z. Zhang, S. Chattopadhyay, Lego-Inspired Glass Capillary Microfluidic Device: A Technique for Bespoke Microencapsulation of Phase Change Materials, ACS Applied Materials & Interfaces, 15 (2023) 17195-17210.
[95] J. Liu, J. R. Streufert, K. Mu, T. Si, T. Han, Y. Han, X. Lin, J. Li, P. V. Braun, Polymer Composites Containing Phase-Change Microcapsules Displaying Deep Undercooling Exhibit Thermal History-Dependent Mechanical Properties, Advanced Materials Technologies, 5(10) (2020) 2000286.
[96] M. Li, W. Wang, Z. Zhang, F. He, S. Yan, P.-J. Yan, R. Xie, X.-J. Ju, Z. Liu, L.-Y. Chu, Monodisperse Na2SO4·10H2O@SiO2 Microparticles against Supercooling and Phase Separation during Phase Change for Efficient Energy Storage, Industrial & Engineering Chemistry Research, 56(12) (2017) 3297-3308.

[97] C. Wang, R. Liu, L. Li, X. Chen, Fabrication of microencapsulated phase change materials using microfluidics, in: MEMAT 2022; 2nd International Conference on Mechanical Engineering, Intelligent Manufacturing and Automation Technology, 2022; pp. 1-4.
[98] X. Zhang, M. Hong, H. Wan, L. Luo, Z. Yu, R. Guo, Identification of Key Genes Involved in Embryo Development and Differential Oil Accumulation in Two Contrasting Maize Genotypes, Genes, 10 (2019) 993.
[99] R. Ji, Q. Zhang, F. Zhou, F. Xu, X. Wang, C. Huang, Y. Zhu, H. Zhang, L. Sun, Y. Xia, X. Lin, H. Peng, Y. Zou, H. Chu, Electrospinning fabricated novel poly (ethylene glycol)/graphene oxide composite phase-change nano-fibers with good shape stability for thermal regulation, Journal of Energy Storage, 40 (2021) 102687.
[100] X. Zhang, R. Xie, W. X. Hu, Y. Faraj, Q. Zhao, X. X. Fan, W. Wang, X. J. Ju, Z. Liu, L. Y. Chu, Microfluidic fabrication of core-sheath composite phase change microfibers with enhanced thermal conductive property, Journal of Material Science, 53(23) (2018) 15769-15783.
[101] G.-Q. Wen, R. Xie, W.-G. Liang, X.-H. He, W. Wang, X.-J. Ju, L.-Y. Chu, Microfluidic fabrication and thermal characteristics of core–shell phase change microfibers with high paraffin content, Applied Thermal Engineering, 87 (2015) 471-480.
[102] X. R. Wen G, Ju X, Wang W, Liu Z, Chu L, Preparation and properties of MWNT/polyvinyl butyral composite phase change fibers, Chemical Industry and Engineering Progress, 34 (2015) 3688–3692.
[103] Y. Yan, W. Li, R. Zhu, C. Lin, R. Hufenus, Flexible Phase Change Material Fiber: A Simple Route to Thermal Energy Control Textiles, Materials, 14 (2021) 401.
[104] R. Yang, Y. Zhang, X. Wang, Y. Zhang, Q. Zhang, Preparation of n-tetradecane-containing microcapsules with different shell materials by phase separation method, Solar Energy Materials and Solar Cells, 93(10) (2009) 1817-1822.
[105] O. Pascu, R. Garcia-Valls, M. Giamberini, Interfacial polymerization of an epoxy resin and carboxylic acids for the synthesis of microcapsules, Polymer International, 57(8) (2008) 995-1006.
[106] Z. Chen, G. Fang, Preparation and heat transfer characteristics of microencapsulated phase change material slurry: A review, Renewable and Sustainable Energy Reviews, 15(9) (2011) 4624-4632.
[107] C. Selvam, D. M. Lal, S. Harish, Thermal conductivity enhancement of ethylene glycol and water with graphene nanoplatelets, Thermochim Acta, 642 (2016) 32-38.
[108] H. Nazir, M. Batool, F. J. Bolivar Osorio, M. Isaza-Ruiz, X. Xu, K. Vignarooban, P. Phelan, Inamuddin, A. M. Kannan, Recent developments in phase change materials for energy storage applications: A review, International Journal of Heat and Mass Transfer, 129 (2019) 491-523.
[109] S. C. Lin, H. H. Al-Kayiem, Evaluation of copper nanoparticles – Paraffin wax compositions for solar thermal energy storage, Solar Energy, 132 (2016) 267-278.
[110] A. D. Brent, V. R. Voller, K. J. Reid, Enthalpy-porosity technique for modeling convection-diffusion phase change: Application to the melting of a pure metal, Numerical Heat Transfer, 13(3) (1988) 297-318.
[111] B. Ding, Z.-H. Zhang, L. Gong, M.-H. Xu, Z.-Q. Huang, A novel thermal management scheme for 3D-IC chips with multi-cores and high power density, Applied Thermal Engineering, 168 (2020) 114832.
[112] G. E. Moore, Cramming more components onto integrated circuits, Proceedings of the IEEE, 86(1) (1998) 82-85.
[113] P. Y. Paik, V. K. Pamula, K. Chakrabarty, A Digital-Microfluidic Approach to Chip Cooling, IEEE Design & Test of Computers, 25(4) (2008) 372-381.
[114] D. B. Tuckerman, R. F. W. Pease, High-performance heat sinking for VLSI, IEEE Electron device letters, 2(5) (1981) 126-129.

[115] C. Xu, S. Xu, R. D. Eticha, Experimental investigation of thermal performance for pulsating flow in a microchannel heat sink filled with PCM (paraffin/CNT composite), Energy Conversion and Management, 236 (2021) 114071.
[116] K. Lim, J. Lee, Experimental study on single-phase convective heat transfer of interlocking double-layer counterflow mini-channel heat sink, Energy Conversion and Management, 243 (2021) 114415.
[117] S. Wang, G. Xia, D. Ma, R. Li, L. Xu, Influence of restrictor on the thermal-hydraulic performance in manifold microchannel heat sink, International Communications in Heat and Mass Transfer, 149 (2023) 107093.
[118] K. Tang, Y. Huang, G. Lin, Y. Guo, J. Huang, H. Lin, H. Zhang, Q. Yang, J. Miao, Thermal-hydraulic performance of ammonia in manifold microchannel heat sink, Applied Thermal Engineering, 232 (2023) 121000.
[119] G. Marseglia, M. G. De Giorgi, P. Pontes, R. Solipa, R. R. Souza, A. L. N. Moreira, A. S. Moita, Enhancement of microchannel heat sink heat transfer: Comparison between different heat transfer enhancement strategies, Experimental Thermal and Fluid Science, 150 (2024) 111052.
[120] P. Pontes, I. Gonçalves, M. Andredaki, A. Georgoulas, A. L. N. Moreira, A. S. Moita, Fluid flow and heat transfer in microchannel devices for cooling applications: Experimental and numerical approaches, Applied Thermal Engineering, 218 (2023) 119358.
[121] P. Bhandari, K. S. Rawat, Y. K. Prajapati, D. Padalia, L. Ranakoti, T. Singh, A review on design alteration in microchannel heat sink for augmented thermohydraulic performance, Ain Shams Engineering Journal, 15(2) (2024) 102417.
[122] W. Q. Tao, Y. L. He, Q. W. Wang, Z. G. Qu, F. Q. Song, A unified analysis on enhancing single phase convective heat transfer with field synergy principle, International Journal of Heat and Mass Transfer, 45(24) (2002) 4871-4879.
[123] V. Leela Vinodhan, K. S. Rajan, Fine-tuning width and aspect ratio of an improved microchannel heat sink for energy-efficient thermal management, Energy Conversion and Management, 105 (2015) 986-994.
[124] X.-D. Wang, A. Bin, J.-L. Xu, Optimal geometric structure for nanofluid-cooled microchannel heat sink under various constraint conditions, Energy Conversion and Management, 65 (2013) 528-538.
[125] S. Shen, J. L. Xu, J. J. Zhou, Y. Chen, Flow and heat transfer in microchannels with rough wall surface, Energy Conversion and Management, 47(11) (2006) 1311-1325.
[126] K. Tang, G. Lin, Y. Guo, J. Huang, H. Zhang, J. Miao, Simulation and optimization of thermal performance in diverging/converging manifold microchannel heat sink, International Journal of Heat and Mass Transfer, 200 (2023) 123495.
[127] G. Xia, D. Ma, Y. Zhai, Y. Li, R. Liu, M. Du, Experimental and numerical study of fluid flow and heat transfer characteristics in microchannel heat sink with complex structure, Energy Conversion and Management, 105 (2015) 848-857.
[128] G. Marseglia, M. G. De Giorgi, D. S. Carvalho, P. Pontes, R. R. Souza, A. L. N. Moreira, A. S. Moita, Experimental investigation on the effects of the geometry of microchannels based heat sinks on the flow boiling of HFE-7100, Applied Thermal Engineering, 236 (2024) 121497.
[129] H. Wang, Z. Chen, J. Gao, Influence of geometric parameters on flow and heat transfer performance of micro-channel heat sinks, Applied Thermal Engineering, 107 (2016) 870-879.
[130] P. Gunnasegaran, H. Mohammed, N. Shuaib, R. Saidur, The effect of geometrical parameters on heat transfer characteristics of microchannels heat sink with different shapes, International communications in heat and mass transfer, 37(8) (2010) 1078-1086.
[131] A. A. Alfaryjat, H. A. Mohammed, N. M. Adam, M. K. A. Ariffin, M. I. Najafabadi, Influence of geometrical parameters of hexagonal, circular, and rhombus microchannel heat sinks on the thermohydraulic characteristics, International Communications in Heat and Mass Transfer, 52 (2014) 121-131.

[132] N. Raja Kuppusamy, R. Saidur, N. N. N. Ghazali, H. A. Mohammed, Numerical study of thermal enhancement in micro channel heat sink with secondary flow, International Journal of Heat and Mass Transfer, 78 (2014) 216-223.
[133] X. Shi, S. Li, Y. Mu, B. Yin, Geometry parameters optimization for a microchannel heat sink with secondary flow channel, International Communications in Heat and Mass Transfer, 104 (2019) 89-100.
[134] W. M. a. A. Japar, N. a. C. Sidik, S. Mat, A comprehensive study on heat transfer enhancement in microchannel heat sink with secondary channel, International Communications in Heat and Mass Transfer, 99 (2018) 62-81.
[135] Y. Sui, C. J. Teo, P. S. Lee, Y. T. Chew, C. Shu, Fluid flow and heat transfer in wavy microchannels, International Journal of Heat and Mass Transfer, 53(13-14) (2010) 2760-2772.
[136] H. A. Mohammed, P. Gunnasegaran, N. H. Shuaib, Influence of channel shape on the thermal and hydraulic performance of microchannel heat sink, International Communications in Heat and Mass Transfer, 38(4) (2011) 474-480.
[137] A. Sakanova, C. C. Keian, J. Zhao, Performance improvements of microchannel heat sink using wavy channel and nanofluids, International Journal of Heat and Mass Transfer, 89 (2015) 59-74.
[138] L. Lin, J. Zhao, G. Lu, X.-D. Wang, W.-M. Yan, Heat transfer enhancement in microchannel heat sink by wavy channel with changing wavelength/amplitude, International Journal of Thermal Sciences, 118 (2017) 423-434.
[139] A. Alkhazaleh, F. Alnaimat, M. Y. E. Selim, B. Mathew, Liquid cooling of microelectronic chips using MEMS heat sink: Thermohydraulic characteristics of wavy microchannels with pin-fins, International Journal of Thermofluids, 18 (2023) 100313.
[140] M. Daadoua, B. Mathew, F. Alnaimat, Experimental investigation of pressure drop and heat transfer in minichannel with smooth and pin fin surfaces, International Journal of Thermofluids, 21 (2024) 100542.
[141] P. Bhandari, K. S. Rawat, Y. K. Prajapati, D. Padalia, L. Ranakoti, T. Singh, Design modifications in micro pin fin configuration of microchannel heat sink for single phase liquid flow: A review, Journal of Energy Storage, 66 (2023) 107548.
[142] L. Chai, G. Xia, M. Zhou, J. Li, J. Qi, Optimum thermal design of interrupted microchannel heat sink with rectangular ribs in the transverse microchambers, Applied Thermal Engineering, 51(1) (2013) 880-889.
[143] D. Yang, Y. Wang, G. Ding, Z. Jin, J. Zhao, G. Wang, Numerical and experimental analysis of cooling performance of single-phase array microchannel heat sinks with different pin-fin configurations, Applied Thermal Engineering, 112 (2017) 1547-1556.
[144] R. Chein, J. Chen, Numerical study of the inlet/outlet arrangement effect on microchannel heat sink performance, International Journal of Thermal Sciences, 48(8) (2009) 1627-1638.
[145] M. R. Hajmohammadi, P. Alipour, H. Parsa, Microfluidic effects on the heat transfer enhancement and optimal design of microchannels heat sinks, International Journal of Heat and Mass Transfer, 126 (2018) 808-815.
[146] M. Xu, H. Lu, L. Gong, J. C. Chai, X. Duan, Parametric numerical study of the flow and heat transfer in microchannel with dimples, International Communications in Heat and Mass Transfer, 76 (2016) 348-357.
[147] C. Zhang, Y. Chen, M. Shi, Effects of roughness elements on laminar flow and heat transfer in microchannels, Chemical Engineering and Processing: Process Intensification, 49(11) (2010) 1188-1192.
[148] O. O. Adewumi, T. Bello-Ochende, J. P. Meyer, Constructal design of combined microchannel and micro pin fins for electronic cooling, International Journal of Heat and Mass Transfer, 66 (2013) 315-323.
[149] S. P. Jang, S. U. S. Choi, Cooling performance of a microchannel heat sink with nanofluids, Applied Thermal Engineering, 26(17) (2006) 2457-2463.

[150] J. Wu, J. Zhao, J. Lei, B. Liu, Effectiveness of nanofluid on improving the performance of microchannel heat sink, Applied Thermal Engineering, 101 (2016) 402-412.
[151] A. Shalchi-Tabrizi, H. R. Seyf, Analysis of entropy generation and convective heat transfer of Al2O3 nanofluid flow in a tangential micro heat sink, International Journal of Heat and Mass Transfer, 55(15) (2012) 4366-4375.
[152] Z. Azizi, A. Alamdari, M. R. Malayeri, Convective heat transfer of Cu–water nanofluid in a cylindrical microchannel heat sink, Energy Conversion and Management, 101 (2015) 515-524.
[153] M. Bahiraei, S. Heshmatian, Thermal performance and second law characteristics of two new microchannel heat sinks operated with hybrid nanofluid containing graphene–silver nanoparticles, Energy Conversion and Management, 168 (2018) 357-370.
[154] S. M. Peyghambarzadeh, S. H. Hashemabadi, A. R. Chabi, M. Salimi, Performance of water based CuO and Al2O3 nanofluids in a Cu–Be alloy heat sink with rectangular microchannels, Energy Conversion and Management, 86 (2014) 28-38.
[155] M. M. Sarafraz, V. Nikkhah, M. Nakhjavani, A. Arya, Thermal performance of a heat sink microchannel working with biologically produced silver-water nanofluid: Experimental assessment, Experimental Thermal and Fluid Science, 91 (2018) 509-519.
[156] H. M. Ali, W. Arshad, Effect of channel angle of pin-fin heat sink on heat transfer performance using water based graphene nanoplatelets nanofluids, International Journal of Heat and Mass Transfer, 106 (2017) 465-472.
[157] A. Ijam, R. Saidur, P. Ganesan, Cooling of minichannel heat sink using nanofluids, International Communications in Heat and Mass Transfer, 39(8) (2012) 1188-1194.
[158] A. Ijam, R. Saidur, Nanofluid as a coolant for electronic devices (cooling of electronic devices), Applied Thermal Engineering, 32 (2012) 76-82.
[159] H. R. Seyf, Z. Zhou, H. Ma, Y. Zhang, Three dimensional numerical study of heat-transfer enhancement by nano-encapsulated phase change material slurry in microtube heat sinks with tangential impingement, International journal of heat and mass transfer, 56(1-2) (2013) 561-573.
[160] M. Chen, Y. Wang, Z. Liu, Experimental study on micro-encapsulated phase change material slurry flowing in straight and wavy microchannels, Applied Thermal Engineering, 190 (2021) 116841.
[161] H. Idris Abdu, K. Eid, A. M. Abdullah, M. H. Sliem, A. Elzatahry, X. Lu, Dry ice-mediated rational synthesis of edge-carboxylated crumpled graphene nanosheets for selective and prompt hydrolysis of cellulose and eucalyptus lignocellulose under ambient reaction conditions, Green Chemistry, 22(16) (2020) 5437-5446.
[162] A. K. Ipadeola, M. Chitt, A. Abdelgawad, K. Eid, A. M. Abdullah, Graphene-based catalysts for carbon monoxide oxidation: Experimental and theoretical insights, International Journal of Hydrogen Energy, 48(46) (2023) 17434-17467.
[163] F. Nemati, M. Rezaie, H. Tabesh, K. Eid, G. Xu, M. R. Ganjali, M. Hosseini, C. Karaman, N. Erk, P.-L. Show, N. Zare, H. Karimi-Maleh, Cerium functionalized graphene nano-structures and their applications; A review, Environmental Research, 208 (2022) 112685.
[164] M. Hu, D. Wang, G. Kokogiannakis, J. Darkwa, Y. Li, L. Wang, Q. Xu, W. Su, Enhancement of thermal and mechanical properties of microencapsulated phase change materials with graphene oxide, Chemical Engineering Journal, 479 (2024) 147855.
[165] T. Hutter, W.-A. Bauer, S. Elliott, W. Huck, Formation of Spherical and Non-Spherical Eutectic Gallium-Indium Liquid-Metal Microdroplets in Microfluidic Channels at Room Temperature, Advanced Functional Materials, 22 (2012) 2624-2631.
[166] W. Olbricht, D. Kung, The deformation and breakup of liquid drops in low Reynolds number flow through a capillary, Physics of Fluids, 4 (1992) 1347-1354.
[167] H. John, I. Lienhard, V. Lienhard, A heat transfer textbook, Phlogiston Press, Cambridge, (2008)

[168] G. K. Batchelor, The effect of Brownian motion on the bulk stress in a suspension of spherical particles, Journal of Fluid Mechanics, 83(1) (1977) 97-117.
[169] H. Inaba, M. J. Kim, A. Horibe, Melting heat transfer characteristics of microencapsulated phase change material slurries with plural microcapsules having different diameters, Journal of Heat Transfer, 126(4) (2004) 558-565.
[170] Y. Yang, J. Du, M. Li, W. Li, Q. Wang, B. Wen, C. Zhang, Y. Jin, W. Wang, Embedded microfluidic cooling with compact double H type manifold microchannels for large-area high-power chips, International Journal of Heat and Mass Transfer, 197 (2022) 123340.
[171] R. L. Webb, Performance evaluation criteria for use of enhanced heat transfer surfaces in heat exchanger design, International Journal of Heat and Mass Transfer, 24(4) (1981) 715-726.
[172] J. D. Anderson, J. Wendt, Computational fluid dynamics, Springer, 1995.
[173] A. S. Utada, E. Lorenceau, D. R. Link, P. D. Kaplan, H. A. Stone, D. A. Weitz, Monodisperse Double Emulsions Generated from a Microcapillary Device, Science, 308(5721) (2005) 537-541.
[174] H. Zhou, J. Lee, M. Kang, H. Kim, H. Lee, J. B. In, All laser-based fabrication of microchannel heat sink, Materials & Design, 221 (2022) 110968.
[175] P. Dixit, N. Lin, J. Miao, W. K. Wong, T. K. Choon, Silicon nanopillars based 3D stacked microchannel heat sinks concept for enhanced heat dissipation applications in MEMS packaging, Sensors and Actuators A: Physical, 141(2) (2008) 685-694.
[176] D. Kong, K. W. Jung, S. Jung, D. Jung, J. Schaadt, M. Iyengar, C. Malone, C. R. Kharangate, M. Asheghi, K. E. Goodson, H. Lee, Single-phase thermal and hydraulic performance of embedded silicon micro-pin fin heat sinks using R245fa, International Journal of Heat and Mass Transfer, 141 (2019) 145-155.
[177] A. Megahed, I. Hassan, Two-phase pressure drop and flow visualization of FC-72 in a silicon microchannel heat sink, International Journal of Heat and Fluid Flow, 30(6) (2009) 1171-1182.
[178] J. Jaseliūnaitė, M. Šeporaitis, Performance optimisation of microchannel pin-fins using 2D CFD, Applied Thermal Engineering, 206 (2022) 118040.
[179] J. Wu, H. Fang, J. Zhang, S. Yan, Modular microfluidics for life sciences, Journal of Nanobiotechnology, 21(1) (2023) 85.
[180] T. Li, L. Zhao, W. Liu, J. Xu, J. Wang, Simple and reusable off-the-shelf microfluidic devices for the versatile generation of droplets, Lab on a Chip, 16(24) (2016) 4718-4724.
[181] J. Liu, J. R. Streufert, K. Mu, T. Si, T. Han, Y. Han, X. Lin, J. Li, P. V. Braun, Polymer Composites Containing Phase‐Change Microcapsules Displaying Deep Undercooling Exhibit Thermal History‐Dependent Mechanical Properties, Advanced Materials Technologies, 5(10) (2020) 2000286.

Abbreviation

LMPA	low melting point alloy
GO	graphene oxide
MEPCM	micro-encapsulated phase change material

MCHS	Microchannel heat sik
HDDA	hexanediol diacrylate
OM	optical microscopy
PCM	phase change material
SEM	Scanning electron microscopy
TGA	thermogravimetric analyzer

Nomenclature

A	mush zone constant [kg/m s^{-1}]
A_c	convection heat transfer area [m^2]
C_P	specific heat[J/kg]
C_1	constant [-]
C_2	constant [-]
Ca	capillary number [-]
D_h	hydraulic diameter [mm]
F	surface tension force acting on the interface [N/m^3]

f	frequency [Hz]
$\boldsymbol{f_c}$	collision term [N/m^3]
F	inhomogeneous term [N/m^3]
$\vec{F}$	interfacial tension force [N]
H	total enthalpy (J/kg)
h	width of the microchannel [mm]
ΔH	enthalpy of phase change (J/kg)
k	Thermal conductivity (W/m K^{-1})
k_1	wavenumber [-]
k_{min}	minimum rupture wave number [-]
L	specific melting enthalpy (J/kg)
$\hat{n}$	surface unit norm [-]
n	unit normal vector at the interface
Nu	Nusselt number
P	pressure (N/m^2)
P_0	unperturbed pressure [N/m^2]
Q	volumetric flow rate ratio [µL/h]

R	radius [m]
R_1	principal radii of curvature [m]
$R_{cond,mean}$	thermal resistance for thermal conduction [K/W·cm^2]
$R_{conv,mean}$	thermal resistance for convective heat transfer [K/W·cm^2]
$R_{heat,mean}$	thermal resistance for the finite heat capacity [K/W·cm^2]
S	source term [N/m]
S	source term (N/m^3)
T	temperature (K)
t	time [s]
T_L	liquidus temperature [K]
T_{ref}	reference temperature [K]
T_S	solidus temperature [K]
V	velocity (m/s)
w	mass fraction of nanofluid (-)
W	width [mm]
We	Weber number [-]

Greek letters

α	proportion of fluid phase [-]
β	constant [-]
ω	constant [-]
σ	surface tension [N/m]
κ	local curvature [-]
μ	viscosity [[kg/m s^{-1}]
ρ	density [mg/m^3]
γ	liquid fraction [-]
ε	Constant [-]
φ	volume fraction

Subscripts

atm	atmosphere pressure
avg	average
C	continuous phase
c	channel

D	dispersed phase
in	inlet
L	solidus
nf	nanofluid
out	outlet
p	particles
S	Slurry
s	sink material
W	wall
w	water
r	radial component
tot	total
θ	circumferential component
σ	interface